ENHANCEMENT OF OPTICAL PROPERTIES IN ARTIFICIAL METAL-DIELECTRIC STRUCTURES

by
Tengfei Li

A dissertation submitted to The Johns Hopkins University in conformity
with the requirements for the degree of Doctor of Philosophy

Baltimore, Maryland
June, 2020

Abstract

The thesis consists of 7 self-contained chapters. Following the introductory Chapter 1, in Chapter 2, I analyze the enhancement of radiation in HMMs by going beyond usual "effective medium" model and discovering many interesting phenomena that augment and, in some cases, contradict the established results. I discover that Purcell enhancement of radiation is always present in metal dielectric structures and that it results from the direct coupling of the energy into the free electron motion in the metal that leads to quenching of the radiative lifetime. In Chapter 3, I study the so-called hyperlensing purportedly capable of imaging sub-wavelength objects. I analyze the imaging properties of HMMs by using newly developed Eigen-mode approach as well as by transfer matrix method. In Chapter 4, I study arrays of subwavelength resonant features made form metals and dielectrics. In this array mid-infrared fields get greatly enhanced which is extremely important for applications in sensing. I establish that to achieve the strongest enhancement, one still needs to use metals, due to high free carrier density in them. That makes the metals preferred in fluorescence or Raman sensing. The subject of Chapter 5 is also related to the mid-infrared region where I explore the light manipulation with metasurface consisting of metal-isolator metal (MIM) resonators. Based on theoretical analysis and simulation performed by me, a metasurface was designed and fabricated using nanoimprint method and later analyzed using Fourier Transform Infrared Spectrometry. Chapter 6 is dedicated to a new material that can be greatly broaden the range of features attainable in metal dielectric structure – a two-dimensional MoS_2. An origami-inspired self-folding

approach is used to reversibly transform MoS_2 into functional 3D optoelectronic devices. We demonstrated that the 3D self-folded MoS_2 structures show enhanced light interaction and are capable of angle-resolved photodetection. Chapter 7 deals with periodically poled lithium niobate for frequency conversion for a novel application – development of non-magnetic optical isolator – a key component for application in optical communications and especially in integrated optics. The nonmagnetic isolator based on frequency converter was proposed, designed, fabricated and tested showing excellent performance characteristics in terms of isolation ratio exceeding 20dB.

Thesis Readers

Dr. Jacob B. Khurgin (Primary Advisor)
    Professor
    Department of Electrical and Computer Engineering
    Johns Hopkins University

Dr. Amy C. Foster
    Associate Professor
    Department of Electrical and Computer Engineering
    Johns Hopkins University

Dr. David H. Gracias
    Professor
    Department of Chemical and Biomolecular Engineering
    Johns Hopkins University

Dr. Susanna M. Thon
    Associate Professor
    Department of Electrical and Computer Engineering
    Johns Hopkins University

Acknowledgements

First of all, I would like to express my sincere gratitude to my advisor Prof. Jacob B. Khurgin for the continuous support of my PhD study and related research, for his patience, motivation, and immense knowledge. His guidance helped me through all the time of research and writing of this thesis. I could not have imagined having a better advisor and mentor for my PhD study.

Besides my advisor, I would like to pay particular thanks to my thesis committee: Dr. Amy Foster, Dr. Thon Susanna and Dr. David H. Gracias for their patience in reading my research proposal and dissertation, insightful comments and encouragement. I am grateful to them for the fruitful discussions and valuable suggestions.

I thank my friends and colleagues at Johns Hopkins University: Nathan Henry, Ruidong Xue, P. Noire and Stella Artois for their help and support during my PhD study.

I would like to thank our collaborators: Weinan Xu, Vivel Nagal, Qi Huang from Department of Chemical and Biomolecular Engineering at Johns Hopkins Univeristy; Kamal Khalil and Dr. Sasan Fathpoure at University of Central Florida for their fruitful achievement, I expanded my knowledge and honed my skills working with them.

I would like to thank NSF (National Science Foundation) and ARO (Army Research Office) for the financial support essential to successfully complete this thesis.

Last but not the least, I would like to thank my family: my parents, my wife, my son,

my parents in law for their unconditional love and support, optimism encouragements, which made my doctoral journal much easier than otherwise.

Contents

List of Figures

Chapter 1

Introduction to Artificial Optical Structures: Metamaterials & Metasurfaces

1.1   Introduction to Metamaterials & Metasurfaces

Performance of all photonic devices is based on controlling the interaction between electromagnetic wave and materials. Hence, by manipulating the light-matter interaction in a desired manner through engineered structures and geometries using available materials, one can achieve control over the electromagnetic functionality.

Therefore, the ultimate performance of electronic and photonic devices is limited by the range of available materials used to build them. To realize a novel electromagnetic property macroscopically amounts to creating artifically structured composites consisting of well-arranged functional inclusions of subwvaelength dimensions. Even though their dimensions are several orders of magnitude above the atomic or molecular level of a conventional material, the scale of these inclusions is still small compared to the wavelength of interest, hence, their electromagnetic response is homogeneous. Such kind of artificial material by which one can achieve new optical properties and phenomena, is usually called "metamaterials".

Usually the definition and the basic characteristic of metamaterials is given as

[1]: "A metamaterial is an artificially structured material which attains its properties form the unit structure rather than the constituent materials. A metamaterial has an inhomogeneity scale that is much smaller that the wavelength of interest, and its electromagnetic response is expressed in terms of homogenized material parameters."

All the electromagnetic phenomena are governed by Maxwell's equations, which are a set of equations describing the interrelationship between fields, sources, and materials properties. The electromagnetic properties of a material are determined by two material parameters: the permittivity ϵ and permeability μ, describing the coupling of a material to the electric and magnetic components of an electromagnetic wave, respectively. Since the response of a material to external fields is largely
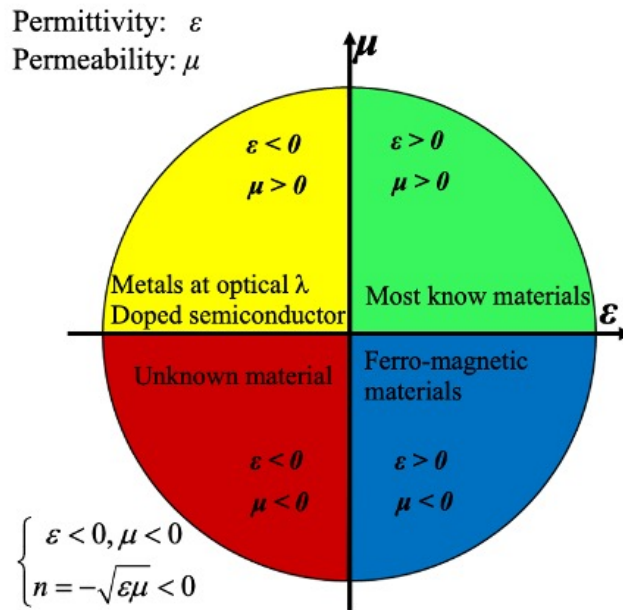
Figure 1-1. Parameter spaces of permittivity ϵ and permeability μ. The two axes correspond to the real parts of permittivity and permeability, respectively [1]

determined only by these two material parameters, we can use an electromagnetic parameter space to classify materials based on the two values, as shown by Fig. 1-1. The real part of permittivity ϵ_r is plotted to the horizontal axis of the parameter space, while the vertical axis corresponds to the real part of permeability μ_r, therefore, materials with all possible combinations of ϵ_r and μ_r can be placed in the parameter

space. In the first quadrant is the conventional materials known as transparent, with positive values of ϵ_r and μ_r. The negative values of ϵ or μ indicate that the direction of the electric or magnetic field induced inside the material, i.e displacement D and magnetization B respectively is opposite to the direction of the field. Noble metals at optical frequencies are good examples for materials with negative ϵ and negative μ can be found in ferromagnetic media near a resonance. No propagating waves can be supported in materials represented by the second and fourth quadrants, where one of the two parameters is negative and the index of refraction becomes purely imaginary. In the third quadrant, no material whose permittivity and permeability are both negative have been found in nature. According to Maxwell's plural equation, when the real part of permittivity and permeability are both negative, then the index is negative. With a negative index, novel and interesting optical phenomena can be anticipated, such as backward wave propagation, reversed Cherenkov radiation [2] and the inverse Doppler effect [3].

Essentially, the research of metamaterial is related to the innovative of exploitation of the electromagnetic parameter space. The major focus of the on going research effort in metamaterial community is to create artificial materials that enter region of the parameters space that are not forbidden by Maxwell's equations but are not observed in any conventional media and to take advantage of this expanded parameter space for better control of electromagnetic waves.

1.2 Surface Plasmon Polaritons (SPPs)

Surface plasmon polaritons (SPPs) are electromagnetic excitations propagating at the interface between a dielectric and a conductor (metal, semiconductor), and SPPs are confined at the interface and evanescent both in the propagation direction and the direction perpendicular to the interface. SPPs are induced by the coupling of the electromagnetic fields to the oscillation of the free electrons in conductor [4]. To

better see the properties of SPPs, let's take the wave equation as a starting point. Equation 1.1 is the general form of wave equation,

$$\nabla^2 E - \frac{\varepsilon}{c}\frac{\partial^2 E}{\partial t^2} = 0 \tag{1.1}$$

where E is the electric field, c is the speed of light, ϵ is the permittivity of material that the light propagating in. This equation has to be solved separately in different regions of ϵ, moreover, boundary conditions have to been rigorously matched. For simplicity, here we assume in a homogeneous material, there is a harmonic time dependent electromagnetic wave, the the electric field is $E(r, t) = E(r)e^{-i\omega t}$, insert into Eq. 1.1, yields

$$\nabla^2 E + k_0^2 \varepsilon E = 0 \tag{1.2}$$

where $k_0 = \omega/c$ is the wave vector of the propagating wave. Equation 1.2 is also known as the Helmholtz equation.

Figure 1-2 shows the geometry we are using here, for simplicity we assume here a one-direction problem, the permittivity ϵ changes only along z direction, $\epsilon = \epsilon(z)$ and the SPPs propagate along the x direction, and there is no spatial variation in the y direction. At the interface $z = 0$, the confined propagating wave can be described as $E(x, y, z) = E(z)e^{i\beta x}$, the complex parameter $\beta = k_x$ is called the propagating constant of the traveling wave and it's the x component of the wave vector in the direction of propagation. Substitute the confined waves into Eq. 1.2 we get

$$\frac{\partial^2 E(z)}{\partial z^2} + \left(k_0^2 \varepsilon - \beta^2\right) E = 0 \tag{1.3}$$

of course, there is a similar equation for the magnetic field H.

To better determine the spatial field profile and dispersion of propagation waves, we find the explicit expressions for the different field components of E and H, and then for the harmonic time dependence ($\frac{\partial}{\partial t} = -i\omega$), we get the following set of coupled

4
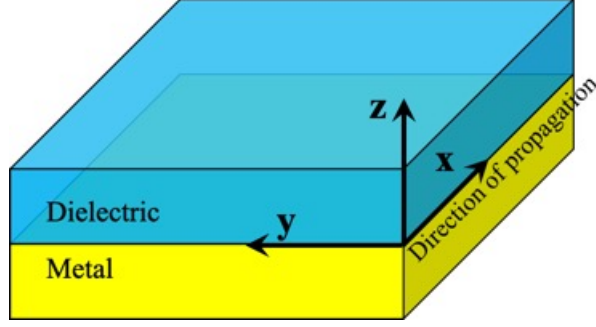
Figure 1-2. Definition of a planar plasmonic waveguide. The waves propagate along the x direction.

equations:

$$\begin{array}{ll} \frac{\partial E_z}{\partial y} - \frac{\partial E_y}{\partial z} = i\omega\mu_0 H_x & \frac{\partial H_z}{\partial y} - \frac{\partial H_y}{\partial z} = -i\omega\mu_0 E_x \\ \frac{\partial E_x}{\partial z} - \frac{\partial E_z}{\partial x} = i\omega\mu_0 H_y & \frac{\partial H_x}{\partial z} - \frac{\partial H_z}{\partial x} = -i\omega\mu_0 E_y \\ \frac{\partial E_y}{\partial x} - \frac{\partial E_x}{\partial y} = i\omega\mu_0 H_z & \frac{\partial H_y}{\partial x} - \frac{\partial H_x}{\partial y} = -i\omega\mu_0 E_z \end{array} \tag{1.4}$$

Due to the propagation along x direction $\left(\frac{\partial}{\partial x} = i\beta\right)$ and the homogeneity in the y direction $\left(\frac{\partial}{\partial y} = 0\right)$, the above equations can be simplified as:

$$\begin{array}{ll} \frac{\partial E_y}{\partial z} = -i\omega\mu_0 H_x & \frac{\partial H_y}{\partial z} = i\omega\mu_0 E_x \\ \frac{\partial E_x}{\partial z} - i\beta E_z = i\omega\mu_0 H_y & \frac{\partial H_x}{\partial z} - i\beta H_z = -i\omega\mu_0 E_y \\ i\beta E_y = i\omega\mu_0 H_z & i\beta H_y = -i\omega\mu_0 E_z \end{array} \tag{1.5}$$

Then these equations can be split into two sets, each one has its self-consistent
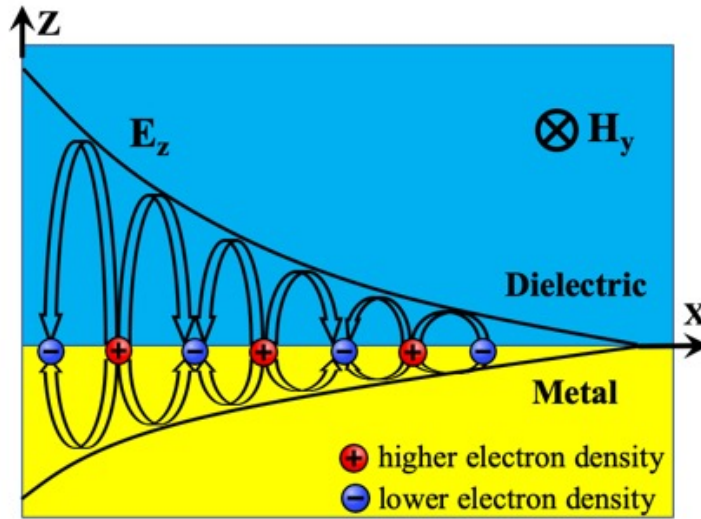
Figure 1-3. Geometry for SPPs propagation at a single interface between a metal and a dielectric.

solutions with different polarization properties of propagating waves. The first set

5

is the transverse magnetic (TM) mode, it contains E_x, E_z and H_y components; the other set is the transverse electric (TE) mode, it contains H_x, H_z and E_y components. Finally, the coupling equations of TM mode reduce to

$$\begin{cases} E_x = -i\frac{1}{\omega\varepsilon_0\varepsilon}\frac{\partial H_y}{\partial z} \\ E_z = -\frac{\beta}{\omega\varepsilon_0\varepsilon}H_y \end{cases} \tag{1.6}$$

and the wave equation for TM mode is

$$\frac{\partial^2 H_y}{\partial z^2} + \left(k_0^2\varepsilon - \beta^2\right)H_y = 0 \tag{1.7}$$

and the coupling equations of TE mode reduce to

$$\begin{cases} H_x = i\frac{1}{\omega\mu_0}\frac{\partial E_y}{\partial z} \\ H_z = \frac{\beta}{\omega\mu_0}E_y \end{cases} , \tag{1.8}$$

and the wave equation for TE mode is

$$\frac{\partial^2 E_y}{\partial z^2} + \left(k_0^2\varepsilon - \beta^2\right)E_y = 0. \tag{1.9}$$

Let's first look at TM solutions. Using Eq. 1.6 set in upper $(z > 0)$ half space we get

$$\begin{cases} H_y(z) = A_2 e^{i\beta x}e^{-k_2 z} \\ E_x(z) = iA_2\frac{1}{\omega\varepsilon_0\varepsilon_2}k_2 e^{i\beta x}e^{-k_2 z} \\ E_z(z) = -A_2\frac{\beta}{\omega\varepsilon_0\varepsilon_2}k_2 e^{i\beta x}e^{-k_2 z} \end{cases} \tag{1.10}$$

in the lower half space $(z < 0)$ we get

$$\begin{cases} H_y(z) = A_1 e^{i\beta x}e^{k_1 z} \\ E_x(z) = -iA_1\frac{1}{\omega\varepsilon_0\varepsilon_1}e^{i\beta x}e^{k_1 z} \\ E_z(z) = -A_1\frac{\beta}{\omega\varepsilon_0\varepsilon_1}e^{i\beta x}e^{k_1 z} \end{cases} \tag{1.11}$$

$k_i = k_{z,i}(i = 1, 2)$ is the component of the wave vector perpendicular to the interface in the two media, hence its reciprocal value $1/\mid k_z \mid$ is the evanescent decay length of the fields perpendicular to the interface, which quantifies the confinement of the wave. By using the boundary condition at the interface, we can get $A_1 = A_2$ and

$$\frac{k_2}{k_1} = -\frac{\varepsilon_2}{\varepsilon_1} \tag{1.12}$$

here we notice that the surface waves can only exit at the interface between two media whose real part of permittivities have opposite signs. Through the TM mode wave equation Eq. 1.7, we get

$$\begin{cases} k_1^2 = \beta^2 - k_0^2 \varepsilon_1 \\ k_2^2 = \beta^2 - k_0^2 \varepsilon_2 \end{cases} \tag{1.13}$$

Finally, the dispersion relation of the surface, which is the Surface Plasmon Polaritons (SPPs), can be obtained by combining Eqs. 1.12 and 1.13

$$\beta = k_0 \sqrt{\frac{\varepsilon_1 \varepsilon_2}{\varepsilon_1 + \varepsilon_2}} \tag{1.14}$$

By following the similar analysis progress for TE mode, we couldn't find a valid solution for it. Hence the surface plasmon polaritons only exist for TM polarization.
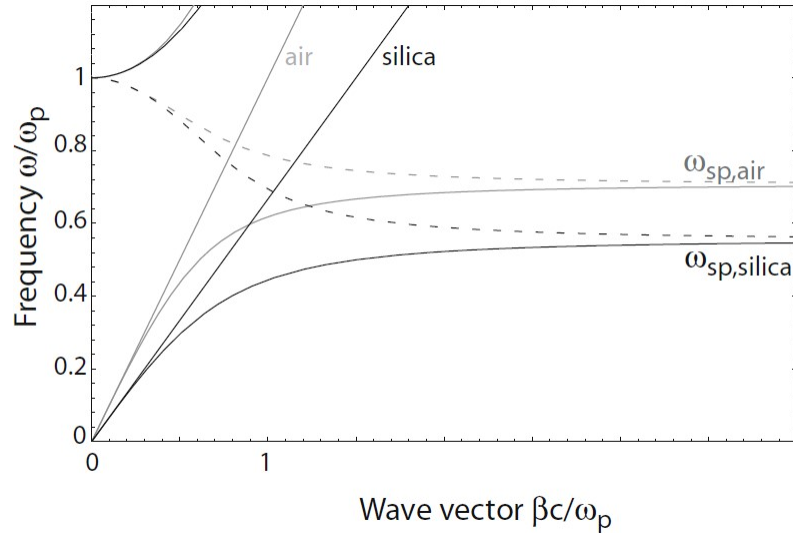
Figure 1-4. Dispersion relation of SPPs at the interface between a Drude metal with negligible collision frequency and air and silica.

An example of SPPs dispersion relations are shown in Fig. 1-4, the SPPs is confined at the interfaces between the real Drude model metal and air, fused silica. And the frequency ω is normalized to the plasma frequency ω_p. We can see that the dispersion curves lay to the right of the respective light lines of air and silica. Hence, compared to the normal propagating wave, SPPs have larger wave vector (propagation constant) and shorter wavelength. For practical situation the materials with negative permittivity

are usually metal and semiconductors, and their permittivities are complex. Hence the propagation constant β of SPPs is also complex, and propagating SPPs are damped with an energy attenuation length, as shown in Fig. 1-3, which is known as propagation length, is L = $(2\text{Im}[\beta])^{-1}$, typically between 10 and 100μm in the visible regime.

As a conclusion, the SPPs is the result of the coupling of electromagnetic wave to the free electrons in metal or doped semiconductors. It exits only at the interface formed by the materials whose permittivities have opposite signs. And due to the existence of the loss of the material whose permittivity is negative, the propagation length of SPPs is limited, moreover, in the perpendicular direction it is also evanescent.

- **Long-range and Short-range SPPs**
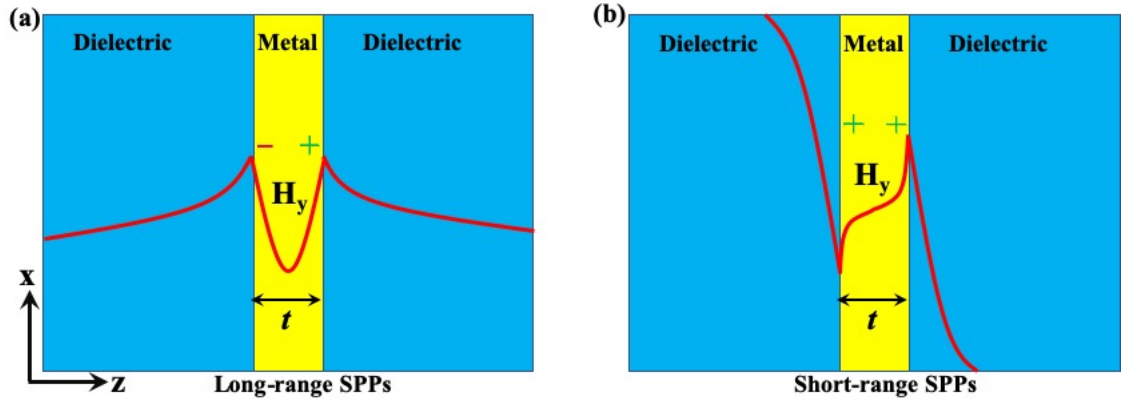
Figure 1-5. Long-range and short-range SPPs

As we have shown above, the SPPs supported by a metal-dielectric interface dissipate exponentially both along and perpendicular to the interface due to the complex refractive index of metal and the loss introduced by the medium bounding the metal. SPPs exhibit interesting properties and useful potential applications. To better utilize SPPs and achieve practical applications, it is necessary to reduce the SPPs attenuation. A common method of reducing SPPs attenuation is to use a thin metal film bounded on two sides by the same dielectric. By doing this the exited SPPs on two sides of metal film will couple to each other, hence coupling

SPPs modes or "super modes" can be obtained. Generally, two super modes can be supported, symmetric and antisymmetric modes, as shown in Fig. 1-5. In Fig. 1-5, only the transverse magnetic field is plotted, and the longitudinal electric field has opposite symmetry, hence as shown in the figure, for the antisymmetric mode, the charge density on two sides of metal film has a symmetric distribution, whereas for the symmetric mode, the charge density distribution is antisymmetric. For the symmetric mode, the attenuation and effective index decrease as t is reduced, and the mode fields increasingly expelled from the metal film and penetrating more deeply into the dielectric, hence the propagation length increases, and the symmetric mode is called "Long-range SPPs mode". For the antisymmetric mode, it exhibits increasing confinement and penetration into the metal with decreasing t, consequently, increasing attenuation and shorter propagation length, so the antisymmetric mode is call "Short-range SPPs mode".

1.3 New Optical Properties of Metamaterials & Metasurfaces

Since the early 2000s, metamaterials have emerged as a rapidly growing inter- disciplinary area, involving physics, electrical engineering, materials science, optics and nanoscience. As we mentioned in the previous section, the properties of metamaterials are tailored by manipulating their internal physical structure, this makes them remarkably different from natural materials, whose properties are mainly decided by their chemical constituents and bonds. Metamaterials consist of periodically or randomly distributed artificial structures that have a size and spacing much smaller than the wavelength of electromagnetic wave. Hence, entirely new properties can emerge, some of which are listed below.

- **Negative Index and Superlens**

As is well known, the refractive index is a complex number n = $n' + in''$, where the imaginary part characterizes light extinction (losses). The real part gives by which the phase velocity of light is decreased in a material as compared to vacuum. Negative index materials (NIM) , whose index is negative, their phase velocity is opposite the energy flow, and this is unusual form the standpoint of traditional optics. Moreover, at the interface between a positive and negative index materials, the refracted light is bent in the counterintuitive way with respect to the normal. The vectors E, H and k form a left-hand coordinate system , hence NIM are also called left-handed materials. As early as 1904, the negative phase velocity and its consequences were studied by Sir Arthur Schuster [5] and H. Lamb [6]. Later the optical properties of NIM were studied by L. I. Mandelstam [7], D. V. Sivukhin [8] and V. G. Veselago [9]. V. G. Veselago provided the modern prescription of 'negative permittivity and negative permeability' for negative refraction. The recent boom of NIM comes from John Pendry [10, 11] who made a number of contribution to the field including his groundbraking prediction of the NIM-based superlens with resolution beyond the diffraction limit [10]. The first NIM was achieved experimentally in 2000 in the microwave range, and the first experimental demonstrations of negative refractive index in optical range were accomplished by using pairs of metal rods and pairs of dielectric voids in metal [13]. After that, many NIM based on metamaterials have be achieved in different range using different structures and methods.

The realization of superlens or perfect lens are based on the achievement of NIM. A possible way to reach a negative refractive index in a passive medium is to design a material whose permittivity $\epsilon = \epsilon' + i\epsilon''$, and the permeability $\mu = \mu' + i\mu''$ obey the equation $\epsilon'|\mu| + \mu'|\epsilon| < 0$, this leads to a negative real part of the refractive index n = $n' + in'' = \sqrt{\epsilon\mu}$. The inequality is always satisfied if both $\epsilon' < 0$ and $\mu' < 0$. But it is not a necessary condition, there may be magnetically active media ($\mu \neq 1$)
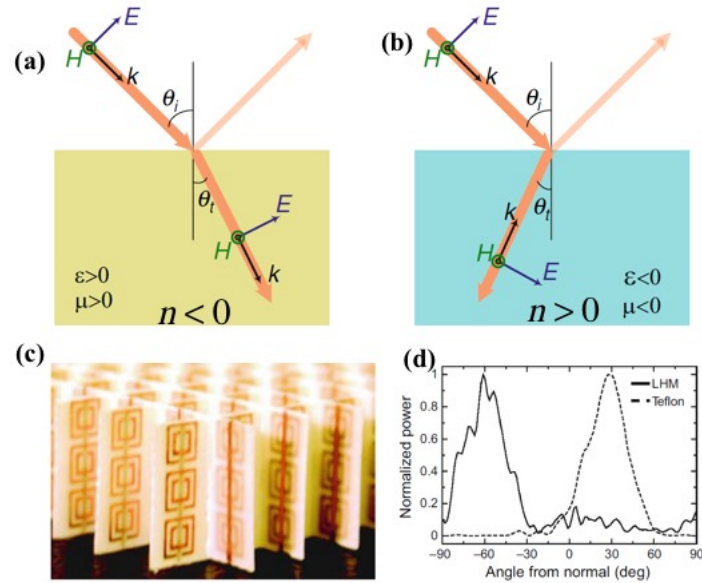
Figure 1-6. Schematic of normal refraction in (a) normal medium and (b) negative refraction in metamaterials with negative effective index. (c) The first demonstrated metamaterial with negative effective index. (d) Comparison of refraction between normal material and metamaterial with negative effective index.[12]

with a positive real part μ' for which the inequality is fulfilled and which therefore show a negative real part of the refractive index n'. Pendry pointed out that a slab with refractive index n $= -1$ surrounded by air allows the imaging of objects with subwavelength precision. Provided that all of the dimensions of a system are much smaller than the wavelength, the electric and magnetic fields can be referred as quasi-static and independent, then the requirement for superlensing is reduced to only $\epsilon = -\epsilon_h$, and ϵ_h is the permittivity of the hose medium interfacing the lens. Based on this condition, scientists found that a slab of silver is a good candidate for such superlens at its surface-plasmon resonance frequency (where $\epsilon = -\epsilon_h$). Such a superlens was achieved experimentally in 2005, as shown in Fig. 1-7. However, this kind of superlens can be operated only at a single frequency satisfying the lens condition $\epsilon(\omega) = -\epsilon_h$, which is a significant drawback for superlens based on bulk metals. Further research has shown that by using metal-dielectric composites instead of bulk metals, people can develop superlens operating at any desired visible

or near-infrared wavelength, with the frequency controlled by the metal fill ratio.
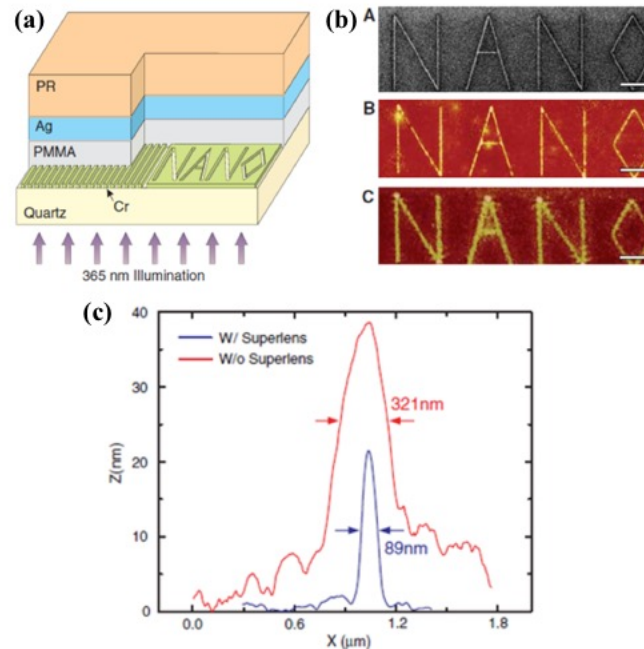
Figure 1-7. (a)Schematic of the superlens. The embedded objects are inscribed onto 50nm-thick Cr; at left is an array of 60-nm-wide slots of 120nm pitch, separated from the 35nm-thick silver film by a 40-nm PMMA spacer layer, the image of the object is recorded by the photoresist on the other side of the silver superlens. (b) A is the FIB image of the object, the linewidth of the "NONA" object was 40nm, the scale in A to C is 2um; B is the AFM of the developed image in photoresist with a silver superlens; C is the AFM of the developed image on photoresist when the 35-nm-thick layer of silver was replaced by PMMA. (c) The averaged cross-section of letter "A" shows an exposed line width of 89nm (blue line), whereas in the control experiment, and the measured diffraction-limited full width at half-maximum line width of 321 (red line).[14]

- **Metamaterial Cloaking**

  An electromagnetic cloak is a structure making an object "invisible" for electromagnetic radiation in a certain frequency range. An object can be regarded as an invisible if it does not reflect waves back to the source, does not scatter waves into other directions and does not generate shadow. That means this kind of objects do not absorb any power and do not make an impact on the fields existing outside the object. Matematerials have simulated another research field- transmission optics. To achieve the cloaking, the total scattering cross section (SCS)
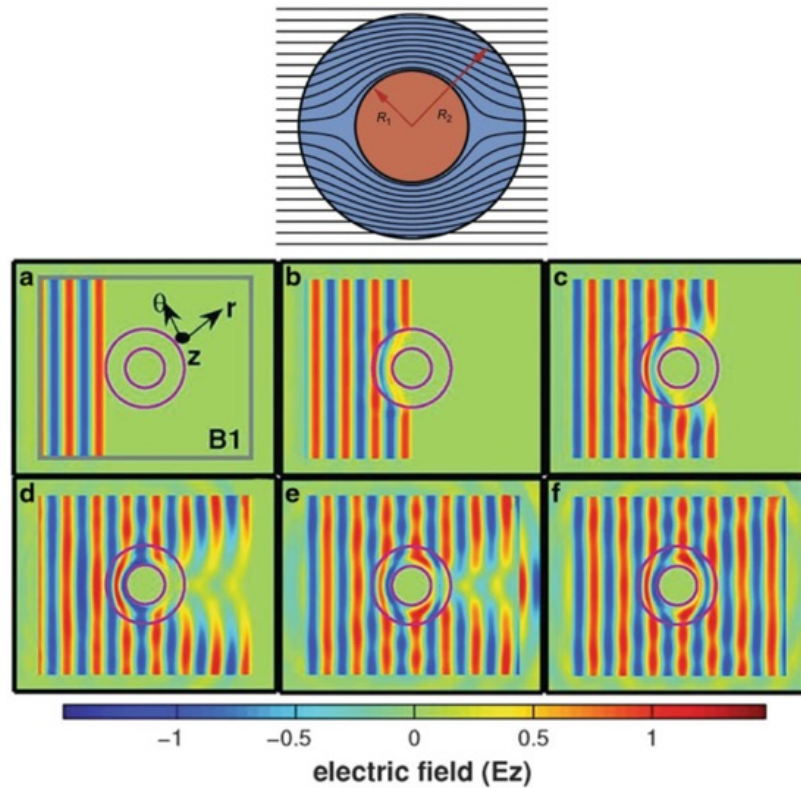
Figure 1-8. Illustration of the coordinate transformation technique: the rays of electromagnetic field are guided inside the cloak device around the volume enclosed by the cloak. The distribution of the electric field at different times: (a) t=2:28T ; (b) t=3.60T ; (c) t=4.92T ; (d) t=7.20T ; (e) t=9.00T ; (f) Stable state. T is the period of the incident wave. [15]

has to be reduced to zero. Several theories and methods have been developed to achieve metamaterial cloaking, such as scattering cancellation method, coordinate transformation technique, transmission-line technique. The first cloaking device was first experimentally demonstrated in 2006 at the frequencies in the microwave radiation band based on the coordinate transformation technique [16], as shown in Fig. 1-8. This device's height was less than 13 mm and its diameter is 125mm, it successfully diverted microwaves around itself and made the SCS zero. The object (a small cylinder) was placed in the center of the device, and the cloak deflected microwave and make the microwave flow around the cylinder with only minor distortion, making it appear almost as if nothing were there. The reflection from the object was reduced by surrounding the object with a shell which is able to affect the passage of light near it. Unlike homogeneous natural material, the metamaterial cloak has to be designed with different properties vary from point to point, and each point should be designed for specific electromagnetic interactions and different directions. Despite the successful demonstration of metamaterial cloak, there are three notable limitations: first of all, the cloak works only in the microwave spectrum and the invisibility has not been realized for visible range. Second, only small objects can made to "disappear" as the surrounding air, for the first metamaterial cloak, a copper cylinder was used, to achieve, the cylinder has to be less than five inches in diameter and less than one half inch in tall. Third, the first achieved cloak can only occur over a narrow frequency band due to the dispersive nature of present-day metamaterials. Because the coordinate transformation requires extraordinary material parameters that are only approachable through the use of resonant elements, the cloaking can be achieved only in very narrow frequency band.

After the first cloak, scientists have developed many others using different methods and metamaterial structures with better performance and at different frequency

ranges. But it still has a long way to go to achieve real cloak that has practical applications.

- **Anomalous reflection and refraction**
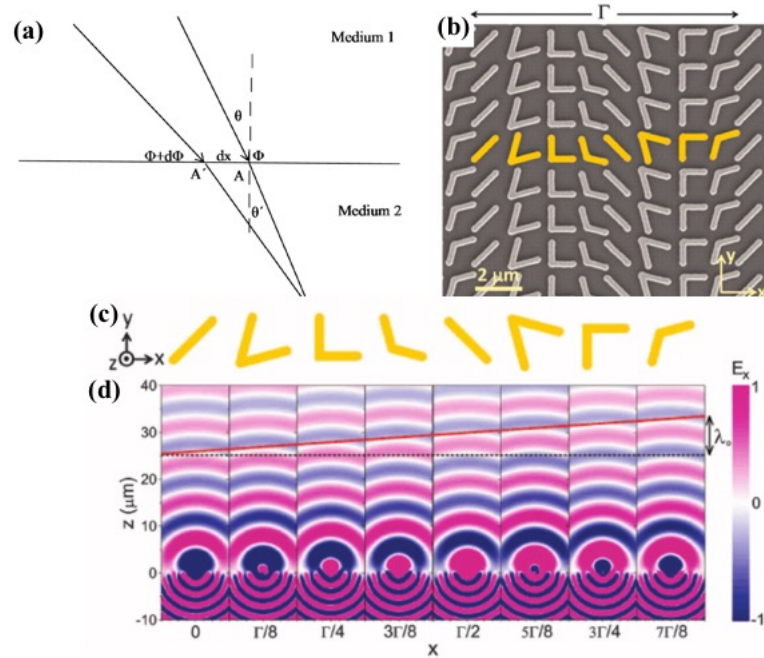
Figure 1-9. (a)An illustration of generalized law of refraction. (b) SEM image of a mid-infrared metasurface consisting of an array of V-shaped gold optical antennas patterned on a silicon wafer, with the unit cell highlighted and $\Gamma = 11\mu$m. It creates a constant gradient of phase jump along the metasurface for the control of the propagation direction of light transmitted through or reflected from the metasurface. (c) Schematic of unit cell of the plasmonic interface for demonstrating the generalized laws of reflection and refraction(d) FDTD simulation of the scattered field for the individual antennas composing the metasurface array. The tilted red line is the envelope of the projections of the spherical waves scattered by the antennas.[17]

As we all know, traditional optical devices, such as lenses and holograms, shape the wavefronts over a distance larger than the operating wavelength [18]. Lenses reshape the light by gradually varying the phase of the incident wave by using their shape and refractive index, holograms generate images in the far-field through interference [19]. Similar to its 3D counterpart—metamaterials, metasurfaces also have the ability to tailor both the electric and magnetic field component of the electromagnetic waves. By carefully design the metasurface, phase jump can

be generated for the electromagnetic wave that passing the metasurface, then the phase is discontinuous, hence the phase can be gradually tempered over a distance. This is helpful to decrease the reliance on wave propagation and allows the shaping of wavefronts and focusing of energy over sub-wavelength distance. Hence, metasurfaces can potentially replace the bulky and heavy devices used traditionally for such purposes. The phase discontinuity or jump comes from the resonant behavior of the miniaturized metasurface building blocks. A surface electromagnetic wave will be induced when an electromagnetic wave incident on individual element of a metasurface, and the surface electromagnetic wave causes the charge to oscillate, which is also known as surface plasmon. The interaction of the impinging electromagnetic wave and the surface plasmon leads to the phase discontinuity across the metasurface and because of this phase jump and discontinuity, the Snell's law is replaced by a "generalized law" for the metasurface [17]. The generalized law is derived based on Fermat's principle of the least time as stationary phase [17]. Fermat's principle states that when light travels between two points, it takes the path which takes the least amount of time. As shown in Fig. 1-9, when a plane wave incident on a metasurface with an incident angle θ, two possible paths that the wave take are shown, because the metasurface causes an abrupt change in the phase, this change at point A is shown by ϕ, while on A′ is it represented by $\phi + \mathrm{d}\phi$. The distance between A and A′ is assumed to be dx, it is also assumed that ϕ is a continuous function of x. It is assumed that the two paths are infinitesimally close such that the phase difference between them to reach point A is zero. This leads to the generalized refraction law given by the following Equation [17]

$$nsin(\theta) - n'sin(\theta') = \frac{\lambda_0}{2\pi n}\frac{dx}{d\phi},$$ (1.15)

Where λ_0 is the wavelength in vacuum, n and n′ are the refractive indices of medium 1 and 2. Similarly the generalized law of reflection for metasurfaces is given by

16

Equation:

$$sin(\theta) - sin(\theta_{refl}) = \frac{\lambda_0}{2\pi n}|\frac{dx}{d\phi}|, \qquad (1.16)$$

where θ_{refl} is the angle of reflection. The non-linear relation between the incident and reflection is worth noting since the angle of incidence and reflection are no longer equal for a metasurface. Equations (1) and (2) can be easily reduced to the original Snell's lay of refraction and reflection if there is no phase jump ($d\phi/dx = 0$). The generalized laws of reflection and refraction have been demonstrated by reflect arrays and v-shaped antennas, respectively [17, 20, 21].

- **Metasurface lenses**

  By designing and fabricating the metasurfaces, ultrathin lenses with high resolution can also be achieved. To focus the electromagnetic wave at a distance d, a metasurface needs to have a phase profile given by the following equation [22],

$$\phi_L(x, y) = \frac{2\pi}{\lambda}\left(\sqrt{x^2 + y^2 + d^2} - d\right), \qquad (1.17)$$

  This profile can alter the shape of the wavefront from planar to spherical, a condition necessary for focusing. When the electromagnetic wave normally incident on the surface, one can get high numerical aperture efficiency, but when the incident angle is not 90 degree, then according to the aberration theory, an aberration called 'coma' occurs, which can cause significant degradation in the numerical aperture efficiency. The coma aberration can be reduced by placing the surface on a curved piece of dielectric. The above v-shape antennas metasurface has shown its ability to focus energy at telecom frequencies [23], another metasurface lens based on reflect-arrays is presented in [24]. This lens was designed based on a metal-insulator-metal structure and work near infrared region. Gold bricks were deposited on silicon dioxide and the individual elements were optimized in order to engineer the desired reflection response. Theoretical efficiency of 78% can be achieved. Another metasurface lens based on rectangular dielectric resonators has

been shown to focus energy at a single focus for three different frequencies. This was made possible by making the sum of the phase transversed by the wave and the phase jump imparted by the metasurface constant at three distinct frequencies, and the resulting metasurface ended up being completely aperiodic [25]. Figure 1-10 shows a thin metalens made of aperiodic dielectric resonators, this metallens have achieve diffraction-limited focusing and sub-wavelength imaging in visible light range. As shown in Fig. 1-10, its resolution is higher than the state-of-art commercial objective for the designed wavelength, the efficiency can be higher than 80%.

1.4 The Future of Metamaterials & Metasurfaces

Metamaterials and metasurfaces are hot and blooming research fields, more and more novel phenomena and applications have been achieved. New research topics have been opened up, such as flat optics and transmission optics. The typical structures described above represent but a small subset of all the opportunities offered by metamaterials and metasurfaces. In the following Chapters I address a few of these opportunities and present a balanced and rigorous assessment of what can be achieved and what are the limitations of metamaterials.
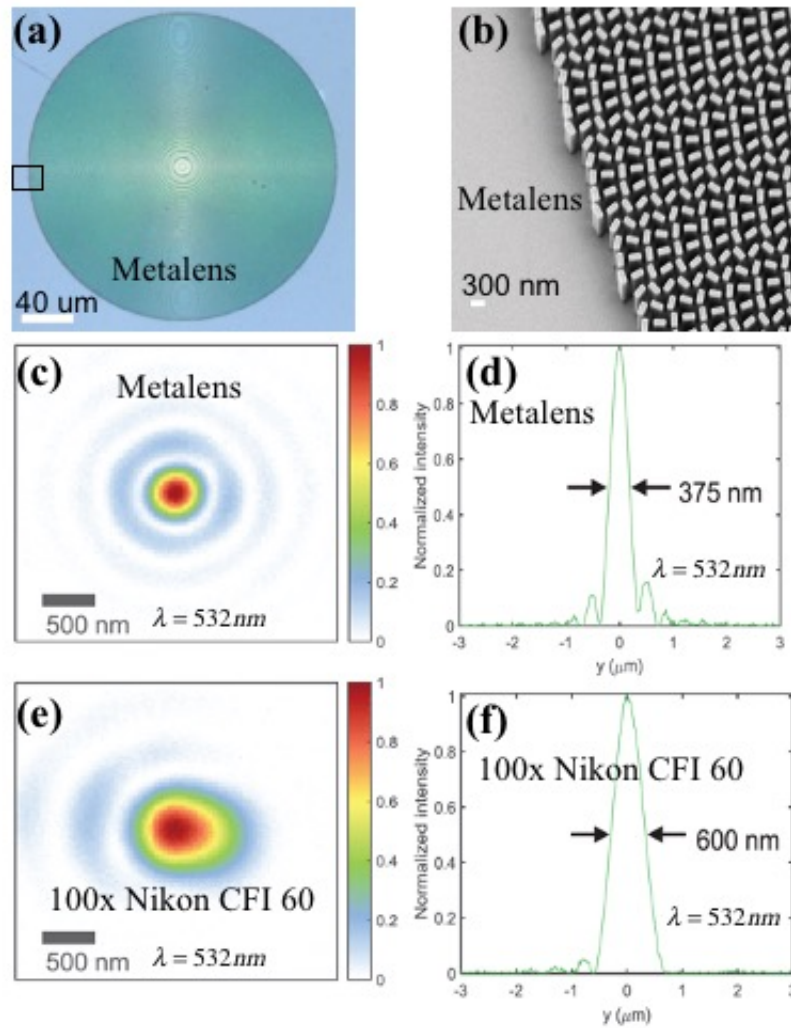
Figure 1-10. (a) and (b) are schematic of the metalens and its building block, the TiO2 nanofin; (c) Measured focal spot intensity profile of the metalens designed at $\lambda = 532$nm;(d) Corresponding vertical cuts of the metalenses' focal spots at $\lambda = 532$nm; (e) Measured focal spot intensity profiles of the objective ($100\times$ Nikon CFI 60, NA = 0.8) at wavelength of $\lambda = 532$nm; (f) Corresponding vertical cuts of the focal spots of the objective, at wavelength $\lambda = 532$nm [26].

Chapter 2

Hyperbolic metamaterials: beyond the effective medium theory

2.1 Introduction to Hyperbolic metamaterials

Nowadays, numerous artificial metamaterials with unusual optical properties have been developed and they are becoming more and more important for controlling the propagation of light. In recent years, the focus of research of metamaterials has gradually changed from passive to active and tunable metamaterials, as well as simplifying structures while keep many of their novel optical properties and functionalities. Among different kinds of metamaterials, one class who are highly anisotropic media and have hyperbolic dispersion, have attracted researches' special attention. Such metamaterials are called hyperbolic metamaterials (HMMs), and they represent the ultra-anisotropic limit of traditional uniaxial crystals and one of the principal components of either permittivity ϵ or permeability μ tensors is opposite in sign to the other two principal components [27–29].

$$\hat{\varepsilon} = \begin{pmatrix} \varepsilon_\perp & 0 & 0 \\ 0 & \varepsilon_\perp & 0 \\ 0 & 0 & \varepsilon_\parallel \end{pmatrix} \hat{\mu} = \begin{pmatrix} \mu_\perp & 0 & 0 \\ 0 & \mu_\perp & 0 \\ 0 & 0 & \mu_\parallel \end{pmatrix} \tag{2.1}$$

The subscripts $\parallel$ and $\perp$ indicate the components parallel and perpendicular to the anisotropy axis, respectively. Most of the properties of HMM can be obtained from the iso-frequency surface of extraordinary waves, the for the HMM, whose permittivity
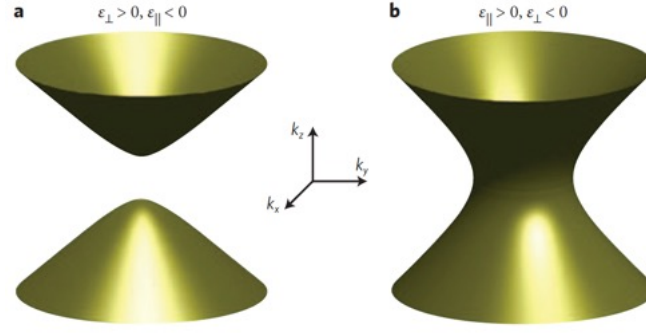
Figure 2-1. Isofrequency surfaces of extraordinary waves in hyperbolic metamaterials.
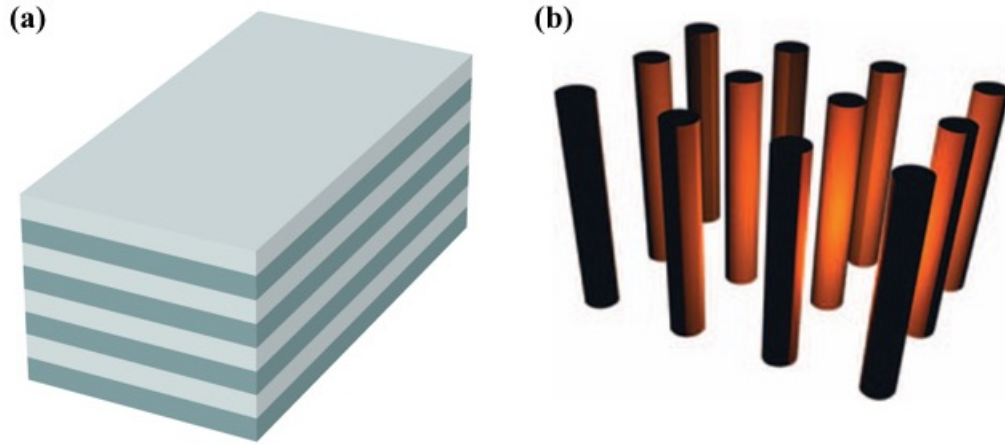
Figure 2-2. (a) Layered metal–dielectric hyperbolic metamaterial; (b) Nanorod-array hyperbolic metamaterial.

tensor elements have opposite signs, its iso-frequency is given by

$$\frac{k_x^2 + k_y^2}{\varepsilon_{\parallel}} + \frac{k_z^2}{\varepsilon_{\perp}} = \left(\frac{\omega}{c}\right)^2, \tag{2.2}$$

where k_x k_y and k_z are the x, y and z components of the wavevector, and ω is the frequency, c is the light speed.

The first HMM was experimentally demonstrated as early as 1969 [30] in a magnetic plasma. Some natural, such as bismuth and graphite, also exhibit hyperbolic properties in certain spectral ranges [31]. Recently, HMM have become a hot research area [32]. Research topics include spontaneous emission enhancement and engineering, realizing large Purcell factor [33], applications in heat transport [34] and acoustics [35] and analogue cosmology [36–38]. Some very practical metamaterial structures have

been fabricated by using HMM, for example, layered metal-dielectric structures and nanowire arrays with hyperbolic dispersion have been experimentally realized across the optical spectrum and various interesting effects have been demonstrated, such as sub-wavelength high-resolution imaging [39–41], focusing [42] and lifetime engineering [43, 44].

For metals, their real part of the dielectric function is negative below the plasma frequency because the polarization response of free moving electrons in the opposite direction to the electric field. For the hyperbolic regime, the components of dielectric tensor are negative in only one or two spatial directions. This can be achieved by restricting free electron motion to these directions. Hence, the most common realization of hyperbolic metamaterials is layered metal-dielectric structures. Figure 2-2, shows an example of a layered metal-dielectric HMM. The components of the effective dielectric tensor parallel ($\epsilon_\parallel$) and perpendicular ($\epsilon_\perp$) to the anisotropy axis are given by [45],

$$\varepsilon_\perp = \frac{\varepsilon_m d_m + \varepsilon_d d_d}{d_m + d_d}, \quad \frac{1}{\varepsilon_\parallel} = \frac{d_m/\varepsilon_m + d_d/\varepsilon_d}{d_m + d_d} \tag{2.3}$$

where $d_m(d_d)$ is the thickness and $\epsilon_m(\epsilon_d)$ is the dielectric constant of the metallic (dielectric) component. We can reach the hyperbolic regime by tuning the parameters, such that $\epsilon_\parallel \epsilon_\perp < 0$. Equation 2.3, which comes from the effective medium approximation under the long-wavelength limit, gives the elements of permittivity tensor. However, despite that the vacuum wavelength is much larger than the period, the excitation of surface plasmon polaritons at the metal-dielectric interface causes the field to vary significantly on the scale of one period. So the approximation given by Eq. 2.3 may not be valid in certain spectral ranges. The Plasmonics modes may have more complex shaped iso-frequency contours that are neither elliptic nor hyperbolic. This leads to both negatively and positively refracted beams being produced by light scattered at the metamaterial interface [46]. The first experimentally demonstration of a layered hyperbolic metamaterial was a hyperlens [39]. Negative

refraction and hyperbolic dispersion were demonstrated in the mid-infrared region using a structure consisting of doped InGaAs and intrinsic AlInAs layers. After that, numerous HMM have been demonstrated that consist of different metal/dielectric pairs, including Ag/AlO$_3$, Ag/polymethyl methacrylate, Ag/LiF, Ag/TiO$_2$, Ag/Ge, Au/Al$_2$O$_3$, Ag/MgF$_2$ and Ag/Ti$_3$O$_5$. Meanwhile, different theories and methods have been developed to analyze the dispersion, refraction and wave propagation in layered HMM [46, 47].

Hyperbolic wire metamaterials are formed by embedding arrays of parallel metallic wires in a dielectric matrix, as shown in Fig. 2-2 [48]. In the model of thin wires in vacuum, the components of the effective dielectric tensor of the wire medium have the form [49],

$$\varepsilon_\perp = 1 \ \varepsilon_\parallel \left(k_z\right) = 1 - \frac{\Omega_p^2}{\omega^2 - \delta^2 - c^2 k_z^2} \tag{2.4}$$

where $\Omega_p \approx c/a \left[\ln\left(a/2\pi R\right)/\left(2\pi\right) + 1/12\right]^{-1/2}$ is the effective plasma frequency, $\delta = \Omega_p a[\pi R^2 \left(1 - \varepsilon_{\text{wire}}\right)]^{-1/2}$, R is the wire radius, a is the period and ϵ_{wire} is the dielectric constant of the wire. For perfectly conducting wires ($\epsilon_{wire} \to \infty$) and in-plane propagation, Eq. 2.4 reduces to the Drude formula, $\varepsilon_\parallel = 1 - \Omega_p^2/\omega^2$, which suggests that the wire metamaterial could attain the hyperbolic regime below the plasma frequency.

The most widely used method to fabricate a nanostructured wire metamaterial is electrochemical deposition of a metal on a porous alumina membrane created by anodization [50]. This is a very efficient approach, allowing samples as large as 1cm $\times$ 1cm $\times$ 50μm to be created [51]. The first demonstrated hyperbolic property of such metamaterials was negative refraction at $\lambda = 780$nm, after that, the wire metamaterials have been extensively studied in experimental studies of biosensing and Purcell factor enhancement [52, 53]. The nanorod structure has a key advantage of being pretty sensitive to the refractive index of the matrix, having a sensitivity exceeding 3×10^4nm per refractive index unit. Hence, nanorod-based metamaterials

outperform surface-plasmon-enhanced sensors based on smooth metallic films.

2.2   The Kronig-Penney (KP) Model

When it comes to theoretical analysis of HMMs to date, the well-tried effective medium theory (EMT) has been relied upon the most [54–56], as well as more complex transfer matrix [33, 47, 57] and Green's function methods [58, 59], which predict Purcell factors (PFs) reaching values exceeding 105 [58], and conversely, as mentioned above, experimentally reported values that do not exceed 80 [60–63]. Numerical FDTD simulation [63, 64] has also been applied to HMMs, showing, once again, the predicted PE far exceeding the observed values. Besides being computationally cumbersome, neither one of these aforementioned "beyond the EMT" methods directly produce IFS in k-space, while the FDTD method fails to offer any physical insight into the picture. Based on the analysis of the rich body of theoretical HMMs work, there are still several questions waiting to be answered. (1) According to the EMT, hyperbolic IFSs exist only for certain relations of layer permittivities and thicknesses. While this prediction must be correct in the limit of infinitely thin layers, it has already been shown in [47] that the elliptical and hyperbolic dispersion regions can overlap. (2) While the giant enhancement of emission rates into the HMMs has been predicted, the enhancement of the rate of radiation coming out of HMMs, i.e., external rather than internal efficiency, has not been thoroughly investigated. (3) Spatial dependence of the PE, critical from a practical point of view, has not been given proper attention. (4) Finally, as any plasmonic (metal/dielectric) structure exhibits the same features as HMMs, namely, strong field confinement and the ability to support large wavevectors and the PE, it is crucial to define the connection between HMMs and the more conventional slab and gap SPPs. To address these questions, we shall use an analytical model that combines simplicity with precision, letting us investigate all the relevant properties of HMMs in great detail and compare them with SPPs. Recently, there has appeared [65] a

study indicating that the density of states in HMMs is similar to that in slab SPPs, and in our work we expand this treatment to gap SPPs. While the results of our work can be used in the evaluation of HMMs in any potential application, we focus mainly on the enhancement of spontaneous emission. Furthermore, while our focus is on the man-made HMMs that comprise metal/dielectric layers, in the end we show that many of our conclusions also hold for natural HMs [66].

2.2.1　The Kronig-Penney (KP) Model in HMM

The KP model was developed in the 1930s [67] to provide a simple explanation of the formation of the band structure in a periodic lattice. Obviously, any attempt to approximate the real crystal potential by a periodic sequence of one-dimensional wells and barriers is bound to lack precision. Thus the KP model has been largely relegated to condensed matter textbooks, until it enjoyed a brief renaissance in 1980s, when it was successfully applied to semiconductor superlattices [68, 69], where the KP potential bears a much closer resemblance to the actual superlattice potential. While the KP model is always an approximation in condensed matter physics, in periodic photonic structures, the KP model is an exact one. Changes in the dielectric permittivity are perfectly well described by the square wave function. The KP model has been successfully used in one-dimensional photonic crystals [70] and it appears to be a good choice for the study of HMMs. The KP model is not computationally heavy and readily provides physical characteristics, such as IFS, dispersion curves, and field shapes. Given these attractive features of the KP model, it appears to be perfectly suited to our task of providing insight into the physics of HMMs.

In this section, we applied the KP model to description the propagation and properties of SPPs inside HMMs. Here the changes of the layered structure's permittivity can be perfectly described by the square wave function, hence for the HMMs, the KP model is no longer an approximation, we can expect that it can provides physical

characteristics of HMMs. The following figure Fig. 2-3 shows an example of a Type I HMM, consisting of Al_2O_3 layers with thickness a and Ag layers with thickness b. The permittivity of Al_2O_3 is constant in the visible range $\epsilon_d = 3.61$, while the permittivity of Ag in the visible range can be fitted into the Drude mode [71]

$$\varepsilon_m(\omega) = 1 - \frac{\omega_p^2}{\omega^2 + i\omega\gamma(\omega)}, \qquad (2.5)$$

where $\omega_p = 1.36 \times 10^{16} s^{-1}$ is the bulk plasma frequency and the scattering rate γ_m is frequency dependent and is $\gamma_m = 8.475 \times 10^{13} s^{-1}$ when the wavelength is $\lambda = 500$nm [71]. For the calculation convenience, we first normalize distance and wave vectors to the wave vector in dielectric (Al_2O_3) $k_d = \epsilon_d^{1/2}\omega/c$, as $x' = xk_d$, so the spatial derivation becomes $\nabla' = k_d^{-1}\nabla$. The magnetic field is normalized to the impedance in dielectric $\eta_d = \sqrt{\mu_0/(\epsilon_0\epsilon_d)}$, as $H_y' = H_y\eta_d$, then the normalized magnetic field has the same unit with electric field (V/m). Here we also define the relative impedance as $\eta'(z) = E(z)/H'(z)$, as will be shown later, the relative impedance defines most of the characteristics of the modes in HMMs, such as the degree of confinement, propagation velocity, PE and propagation distance. By substituting the normalized terms into the first two Maxwell's equation and assuming that all the field are harmonic with frequency ω, we obtain
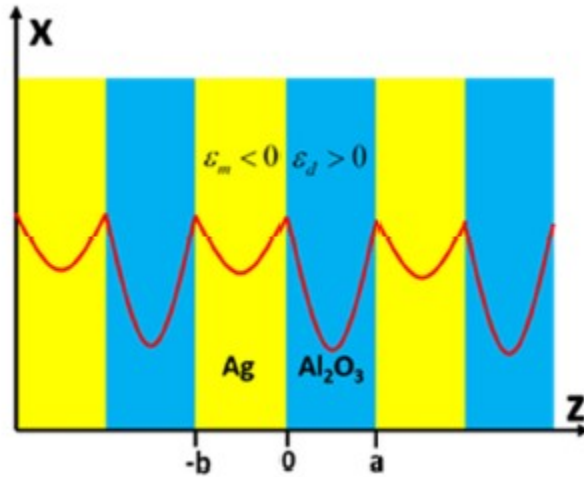
Figure 2-3. The configuration of HMMs comprising layered Ag and Al_2O_3

26

$$\left\{ \begin{array}{c} \nabla' \times H' = -i\varepsilon'(z) E \\ \nabla' \times E = iH' \end{array} \right\} \tag{2.6}$$

where $\epsilon'(z) = \epsilon/\epsilon_d$ is the normalized permittivity. Then as shown in Fig. 2-3, following the KP model, the normalized magnetic field of the TM mode in one period can be expressed as

$$H'_y = \left\{ \begin{array}{l} \left(Ae^{K'z'} + Be^{-K'z'}\right)e^{ik'_x x}, 0 < z < a' \\ \left(Ce^{Q'z'} + De^{-Q'z'}\right)e^{ik'_x x}, -b' < z < 0 \end{array} \right. \tag{2.7}$$

where k'_x is the lateral wave wave vector normalized to k_d, K' and Q' are the normalized decay constants in the dielectric and metal respectively. A to D are the amplitudes will be calculated by using the boundary condition $H_y(z' + a' + b') = H_y(z')e^{[ik'_z(a'+b')]}$. By substituting Eq. 2.7 into the wave equation one can get the relation between the lateral wave vector and the decay constants

$$\left\{ \begin{array}{c} k'^2_x - K'^2 = 1 \\ k'^2_x - Q'^2 = -|\varepsilon'_m| \end{array} \right. \tag{2.8}$$

where $\epsilon'_m = \epsilon_m/\epsilon_d$ is the normalized dielectric constant of the metal. Summing the two above equations

$$Q'^2 - K'^2 = 1 + |\varepsilon'_m| \tag{2.9}$$

We can figure out the relations between the different components of TM mode inside the dielectric layers

$$\left\{ \begin{array}{c} \frac{\partial H'_y}{\partial z} = iE_x \\ k'_x H'_y = -E_z \end{array} \right. \tag{2.10}$$

and inside metal layers

$$\left\{ \begin{array}{c} \frac{\partial H'_y}{\partial z'} = -i|\varepsilon'_m| E_x \\ k'_x H'_y = |\varepsilon'_m| E_z \end{array} \right. \tag{2.11}$$

Form Eqs. 2.9 and 2.10 we can see that larger wave vector results in larger ratio of magnetic to electric field, and smaller local impedance $\eta'(z)$, this has important consequence when I consider the energy balance and propagation velocity. Also, through Eqs. 2.9 and 2.10 one can find the electric field component in dielectric and metal layers

$$E_x = \left\{ \begin{array}{l} -iK'\left(Ae^{K'z'} - Be^{-K'z'}\right)e^{ik'_x x}, 0 < z' < a' \\ \frac{iQ'}{|\varepsilon'_m|}\left(Ce^{Q'z'} - De^{-Q'z'}\right)e^{ik'_x x}, -b' < z' < 0 \end{array} \right. \tag{2.12}$$

27

$$E_z = \begin{cases} -k'_x \left(Ae^{K'z'} + Be^{-K'z'} \right) e^{ik'_x x'}, 0 < z' < a' \\ \frac{k'_x}{|\varepsilon'_m|} \left(Ce^{Q'z'} + De^{-ik'_x x} \right), -b' < z' < 0 \end{cases}$$ (2.13)

Next, via the boundary condition at z = 0 interface for normalized magnetic and tangential electric field we can get

$$\begin{cases} A + B = C + D \\ K'(A - B) = \frac{Q}{|\varepsilon'_m|}(D - C) \end{cases}$$ (2.14)

Similarly, at the z = a interface we can get

$$\begin{cases} Ae^{K'a'} + Be^{-K'a'} = \left(Ce^{-Q'b'} + De^{Q'b'} \right) e^{ik'_z(a'+b')} \\ K' \left(Ae^{K'a'} - Be^{-K'a'} \right) = \frac{Q}{|\varepsilon'_m|} \left(De^{Q'b'} - Ce^{-Q'b'} \right) e^{ik'_z(a'+b')} \end{cases}$$ (2.15)

then combining these above four equations in the matrix form

$$\begin{pmatrix} 1 & 1 & -1 & -1 \\ K' & -K' & \frac{Q'}{|\varepsilon'_m|} & -\frac{Q'}{|\varepsilon'_m|} \\ e^{K'a'} & e^{-K'a'} & -e^{-Q'b'}e^{ik'_z(a'+b')} & -e^{Q'b'}e^{ik'_z(a'+b')} \\ K'e^{K'a'} & -K'e^{K'a'} & \frac{Q'}{|\varepsilon'_m|}e^{-Q'b'}e^{ik'_z(a'+b')} & -\frac{Q'}{|\varepsilon'_m|}e^{-Q'b'}e^{ik'_z(a'+b')} \end{pmatrix} \begin{pmatrix} A \\ B \\ C \\ D \end{pmatrix} = 0$$ (2.16)

This homogeneous equation has a nontrivial solution only if the determinant of the matrix is equal to zero which readily leads us to the characteristic equation of the propagating modes in HMMs

$$\cos(k'_z(a'+b')) = -\frac{1}{2} \left(\frac{Q'}{K'|\varepsilon'_m|} + \frac{K'|\varepsilon'_m|}{Q'} \right) \sinh(K'a')\sinh(Q'b') + \cosh(K'a')\cosh(Q'b')$$ (2.17)

Actually, the characteristic equation Eq. 2.25 can also be achieved through the transfer-matrix method. Each solution of the characteristic equation yields the value of transverse wave vector k'_z for each lateral wave vector k'_x, then the iso-frequency surface (IFS) can achieved as shown in Figs. 2-4(b)and (c) for wavelength $\lambda = 500$nm for different values of thickness ratio TR=a/b, corresponding to four different classes of the effective medium.

As shown in Fig. 2-4(a), large TR results in both lateral and transverse effective dielectric constants are positive, and the effective medium is a conventional (elliptical)

28
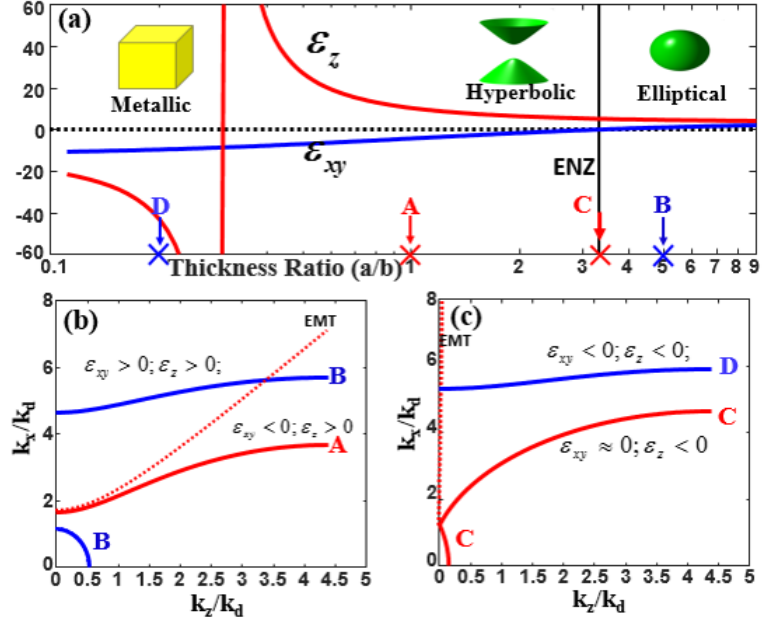
Figure 2-4. (a) Dielectric constants for different TR from EMT; (b, c) IFS for different TR according to Kronig-Penney model, in case B, the elliptical IFS obtained from EMT and KP model are nearly overlapping each other.

dielectric. With the decrease of TR, the lateral dielectric constant ϵ_{xy} changes sign first, which indicates that the medium becomes hyperbolic, and then the transverse dielectric constant ϵ_z also becomes negative, indicating that the material effectively reaches the metallic stage. Figures 2-4(b) and (c) show the IFS in the four regions, we are going to get more details by analyzing different IFS.

For case A, the TR is one, and the permittivity components predicted by EMT are $\epsilon_{xy} = -4.20, \epsilon_z = 10.32$, which places the structure in the hyperbolic region with dotted red line A IFS. The solid red line A is the IFS calculated using KP model, it also shows hyperbolic dispersion, but we can see the two results match each other only when the wave vector is very small, below 10% of the Brillouin zone (BZ), for the KP model dispersion, the slop gradually decreases to zero at the edge of the BZ, which result from the consequence of the reflection.

For case B, the TR is chosen as 5, the EMT predicted permittivities are $\epsilon_{xy} = 1, \epsilon_z = 4.61$, which means that there should be elliptical IFS, as shown by the blue

dotted line in Fig. 2-4(b). However, the KP solution (blue solid line) demonstrates that the hyperbolic and elliptical IFS co-exist, and the elliptical part of the KP model matches the EMT very well.

Next, for the case C, the TR is chosen as 3.33, which makes one of the EMT predicted permittivity component close to zero, $\epsilon_{xy} = -7.9 \times 10^{-4}, \epsilon_z = 5.20$, this makes the structure agrees with the definition of the epsilon-near-zaro (ENZ) metamaterials [72, 73]. According to EMT, the transverse wave vector k_z can become arbitrarily small, indicating the constant phase extending along z axis. This observation is confirmed by the EMT IFS rendered by the nearly vertical dotted red solid line in Fig. 2-4(c). However, the KP model, shown as a red solid line, which takes into account granularity results in an IFS that is quite different from EMT predictions. The IFS has both hyperbolic and elliptical regions, which nearly touch each other and obviously, all the transverse wave vectors within BZ are allowed, as one would expect from the Floquet-Bloch theorem [74]. Clearly, to achieve "true" ENZ, one must either use much thinner layers or revert to bulk highly doped materials with tunable plasma frequency, such as AlZnO [75].

Finally, for case D, TR=0.2, comprising very thin dielectric "gaps" sandwiched between thick metal layers. The EMT predicts two negative effective premittivities $\epsilon_{xy} = -9.41, \epsilon_z = -43.11$, which makes the HMMs an effective metal that cannot support propagating waves in any direction. However, the KP model still agrees with Floquet-Bloch theorem, hyperbolic-like solutions still exist with the IFS becoming more and more horizontal as TR decreases. Actually, the IFS for the nominally elliptical case B and for nominally metallic case D look very similar to each other. They both move "higher" and become more "horizontal" as TR goes to either o or infinity. This means that for either very large or very small TR, I am dealing with waves that propagate mostly in only the lateral direction. This corresponds to the behavior of "weakly coupled" modes in the arrays of dielectric waveguides [76]. Clearly,

the modes of HMMs can be thought of as coupled modes of plasmonic waveguides. In metallic region D of small TR, those modes are the coupled gap SPPs modes. In elliptic region B with large TR, they are coupled slab SPPs modes [77]. To further investigate this analogy, we must first explore HMM characteristics beyond IFS curves.

2.2.2 Fields, Energy Density and Poynting Vector in HMM

Now let's look at the spatial distribution of the field components and the energy and Poynting vectors in HMMs. By using the normalized fields and parameters, the magnetic and electric field energy density can be expresses as

$$
\begin{cases}
U_H = \frac{1}{4} u_0 |H_y|^2 = \frac{1}{4} \varepsilon_0 \varepsilon_d |H'_y|^2 \\
U_E = \frac{1}{4} \varepsilon_0 \frac{\partial \omega \varepsilon(z)}{\partial \omega} E^2 = \frac{1}{4} \varepsilon_0 \varepsilon_d \varepsilon'_g (z) |E|^2
\end{cases}
\tag{2.18}
$$

where $\varepsilon'_g (z) = \varepsilon_d^{-1} \partial \left(\omega \varepsilon_{m(d)} (z) \right) / \partial \omega$ is the normalized frequency dependent "group" permittivity. For metal $\varepsilon'_g = \left(1 + \omega_p^2 / \omega^2 \right) / \varepsilon_d$, while for dielectric it is obvious that $\epsilon'_g = 1$. The total energy density normalized to the energy of the plane wave in the dielectric ($U_{PW} = \frac{1}{2} \varepsilon_0 \varepsilon_d E^2$)is then

$$
U'_T = \frac{1}{2} \left(\varepsilon'_g (z) + |H'_y|^2 / |E|^2 \right) = \frac{1}{2} \left(\varepsilon'_g (z) + \eta'^{-2} (z) \right)
\tag{2.19}
$$

For the plane wave propagating in the unconstrained lossless dielectric, $\epsilon'_g = \eta' = 1$ and $U'_H(z) = U'_E(z)$, hence η' shows important facts about the energy balance in HMMs, and according to [78] when magnetic energy is much less than electric energy, a significant portion of the energy gets stored in the kinetic motion of free electrons in the metal, which leads to ohmic loss. Therefore, large η' is associated with large loss.

The Poynting vector components are also normalized to the plane wave in dielectric. They are calculated as

$$
S_{x(z)} (z) = -\frac{1}{2} \mathrm{Re} \left(E_{z(x)} H_y^* \right) = -\frac{1}{2\eta_d} \mathrm{Re} \left(E_{z(x)} H_y'^* \right)
\tag{2.20}
$$

and then normalized to the Poynting vector of the plane wave in the dielectric

$(S_{PM} = \frac{1}{2\eta_d} \mid E \mid^2)$ to obtain

$$S'_{x(z)}(z) = \operatorname{Re}\left(E_{z(x)}H'^{*}_{y}\right)/|E|^2 \sim e_{z(x)}/\eta'(z) \qquad (2.21)$$

where $e_{x(z)} = E_{x(z)}/ \mid E \mid$ is the projection of the unit vector $\tilde{e}$ indicating the field polarization. It is clear that when magnetic field decreases (and hence effective impedance increases) the power flow gets reduced. This can be better expressed by introducing local energy velocity $\nu_{ex}(z) = S_{x(z)}/U_T(z)$ and then normalizing it to $\nu_d = c/\epsilon_d^{1/2}$ obtaining

$$v'_{ex(z)}(z) = \frac{2e_{z(x)}}{\eta'(z)} \frac{1}{\varepsilon'_g + \eta'^{-2}(z)} \qquad (2.22)$$

It is clear that the velocity gets reduced with the effective local impedance. When this observation is combined with the one made above regarding the increase of loss, it is clear that the increase in the effective impedance always indicates a reduction in the propagation distance.

In this work, I consider spontaneous emission to be simply a stimulated emission caused by the presence of "vacuum" polaritons in the mode. The energy of the polariton is then

$$\hbar\omega = \frac{1}{4}\varepsilon_0\varepsilon_d \int \left[\varepsilon'_g E^2(z) + H'^2(z)\right]dV \qquad (2.23)$$

by defining $E(z) = E_{max}q(z), H'(z) = E_{max}h(z)$ and taking out E^2_{max}, then we can obtain

$$\hbar\omega = \frac{1}{4}\varepsilon_0\varepsilon_d E^2_{max} \int_{-b}^{a} \left[\varepsilon'_g q^2(z) + h^2(z)\right]dV = \frac{1}{4}\varepsilon_0\varepsilon_d E^2_{max}\bar{F}^2 V \qquad (2.24)$$

where V is the quantization volume, and

$$\bar{F}^2 = \int_{-b}^{a} \left[\varepsilon'_g q^2(z) + h^2(z)\right]dz \frac{V}{a+b} \qquad (2.25)$$

is the averaged mode energy. From Eq. 2.24 we obtain $E^2_{max} = 4\hbar\omega/\left(\varepsilon_0\varepsilon_d\bar{F}^2 V\right)$. The square of the matrix element of the interaction Hamiltonian is then

$$\left|M_{x(z)}\right|^2 = e^2 Z^2 E^2_{x(z)}(z) = \frac{2e^2 Z}{\varepsilon_0\varepsilon_g} \frac{q^2_{x(z)}(z)}{\bar{F}^2} \frac{\hbar\omega}{V} \qquad (2.26)$$

where Z is the dipole moment of the transition. Now the factor $\frac{q_{x(z)}^2(z)}{\bar{F}^2} = \frac{q_{x(z)}^2(z)}{\langle \varepsilon'_g q^2 + h^2 \rangle} \equiv \frac{E_{x(z)}^2(z)}{\langle \varepsilon'_g E^2 + H'^2 \rangle}$ is simply the ratio of the local to average field and therefore describes the degree of localization of the electric field. The density of states in HMMs can be calculated by evaluating the volume of the IFS shell for frequency interval $\Delta\omega$ through integration over k_z

$$\rho_{HMM} = 2 \times \frac{1}{8\pi^3} \int\limits_0^{k_{z,\max}} 2\pi k_x \frac{dk_x}{d\omega} dk_z = \frac{1}{2\pi^2} \int\limits_0^{k_{z,\max}} k_x \frac{dk_x}{d\omega} dk_z = \frac{k_d^3}{2\pi^2} \int\limits_0^{k_{z,\max}} k'_x \frac{dk'_x}{d\omega} dk'_z \tag{2.27}$$

where the factor of 2 in the front comes from the fact that the volume of IFS shell extends over both positive and negative z, $+z$ and $-z$ space, respectively. Then according to Fermi's golden rule, the lifetime of energy level of emitter in HMMs can be expressed as

$$\begin{aligned}
\Gamma_{HMM}(z) &= \frac{2\pi}{\hbar} \sum_k |M|^2 \delta(\hbar\omega - \hbar\omega_k) \\
&= \frac{2\pi}{\hbar} \frac{e^2 Z}{2\varepsilon_0 \varepsilon_d} \frac{E^2(z)}{\langle \varepsilon'_g E^2 + H'^2 \rangle} \frac{\hbar\omega}{V} \sum \delta(\hbar\omega - \hbar\omega_k) \\
&= \frac{2\pi}{\hbar} \frac{2e^2 Z}{\varepsilon_0 \varepsilon_d} \frac{\hbar\omega}{V} \frac{V}{\hbar} \int\limits_0^{k_{z,\max}} \frac{E^2(z)}{\langle \varepsilon'_g E^2 + H'^2 \rangle} dk^3 \delta(\hbar\omega - \hbar\omega_k) \\
&= \frac{2\pi}{\hbar} \frac{2e^2 Z}{\varepsilon_0 \varepsilon_d} \frac{\hbar\omega}{V} \frac{V}{\hbar} \frac{1}{2\pi^2} \int\limits_0^{k_{z,\max}} \frac{E^2(z)}{\langle \varepsilon'_g E^2 + H'^2 \rangle} k_x \frac{dk_x}{d\omega} dk_z \\
&= \frac{2}{\hbar\pi} \frac{e^2 Z^2 \omega}{\varepsilon_0 \varepsilon_d} k_d^3 \int\limits_0^{k_{z,\max}} \frac{E^2(z)}{\langle \varepsilon'_g E^2 + H'^2 \rangle} k'_x \frac{dk'_x}{d\omega} dk'_z
\end{aligned} \tag{2.28}$$

In free space (dielectric) the energy of each mode is $\hbar\omega = 1/2\varepsilon_0\varepsilon_d E^2 V$, where v is the quantization volume. Then for the Hamiltonian we have $|M| = e^2 z^2 E^2 = 2\hbar\omega e^2 Z^2 / (\varepsilon_0\varepsilon_d V)$, and the density of states in free space can be calculated as

$$\rho_{free} = 2 \times \frac{1}{8\pi^3} \times 4\pi k_d^2 \times \frac{dk_d}{d\omega} = \frac{k_d}{\pi^2} \frac{dk_d}{d\omega} \tag{2.29}$$

So the radiative decay rate in unrestricted dielectric is

$$\begin{aligned}
\Gamma_{free} &= \frac{2\pi}{\hbar} \sum_k |M|^2 \delta(\hbar\omega - \hbar\omega_k) \\
&= \frac{2\pi}{\hbar} \frac{2\hbar\omega e^2 Z^2}{\varepsilon_0 \varepsilon_d V} \sum_k \delta(\hbar\omega - \hbar\omega_k) \\
&= \frac{2\pi}{\hbar} \frac{2\hbar\omega e^2 Z^2}{\varepsilon_0 \varepsilon_d V} \frac{V}{\hbar} \int\limits_0^k dk^3 \delta(\omega - \omega_k) \\
&= \frac{2\pi}{\hbar} \frac{2\hbar\omega e^2 Z^2}{\varepsilon_0 \varepsilon_d V} \frac{V}{\hbar} \frac{1}{\pi} k_d^2 \frac{dk_d}{d\omega} \\
&= \frac{4}{\hbar\pi} \frac{\omega e^2 Z^2}{\varepsilon_0 \varepsilon_d} k_d^2 \frac{dk_d}{d\omega}
\end{aligned} \tag{2.30}$$

Hence the Purcell factor can be achieved by the ratio of the above two lifetimes in HMMs and free space

$$
\begin{aligned}
PF_{x(z)}\left(z\right) &= \frac{\Gamma_{HMM}(z)}{\Gamma_{free}} \\
&= \frac{\frac{2}{\hbar\pi}\frac{e^2 Z^2 \omega}{\varepsilon_0 \varepsilon_d} k_d^3 \int\limits_0^{k_{z,\max}} \frac{E_{x(z)}^2(z)}{\left\langle \varepsilon'_g E^2 + H'^2 \right\rangle} k'_x \frac{dk'_x}{d\omega} dk'_z}{\frac{4}{\hbar\pi}\frac{\omega e^2 Z^2}{\varepsilon_0 \varepsilon_d} k_d^2 \frac{dk_d}{d\omega}} \\
&= \frac{k_d v_d}{2} \int\limits_0^{k_{z,\max}} \frac{E_{x(z)}^2(z)}{\left\langle \varepsilon'_g E^2 + H'^2 \right\rangle} k'_x \frac{dk'_x}{d\omega} dk'_z \\
&= \frac{1}{2} \int\limits_0^{k_{z,\max}} \frac{E_{x(z)}^2(z)}{\left\langle \varepsilon'_g E^2 + H'^2 \right\rangle} k'_x \frac{1}{v'_g} dk'_z \\
&= \int\limits_0^{k_{z,\max}} PF'_{x(z)} dk'_z
\end{aligned}
\tag{2.31}
$$

where I have neglected the small difference between the group and phase velocities in the dielectric and introduced the differential Purcell factor

$$
PF'_{x(z)}\left(z\right) = \frac{1}{2}\frac{E_{x(z)}^2\left(z\right)}{\left\langle \varepsilon'_g E^2 + H'^2 \right\rangle} k'_x \frac{1}{v'_g} dk'_z
\tag{2.32}
$$

This factor lets us see which states contributes the most to the Purcell factor. If both
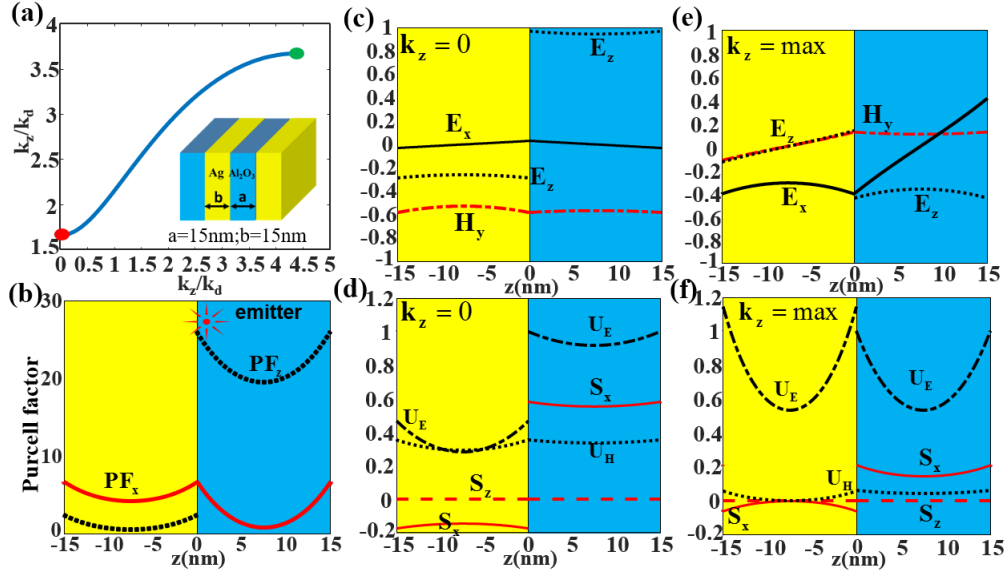
Figure 2-5. (a) IFS at $\lambda = 500$nm for TR=1. (b) PF as a function of the position of the emitter in the dielectric for two polarizations. (c) Fields and (d) energies and Poynting vector for the minimum value of the transverse wavevector and (e),(f) the same for the maximum value of the transverse wavevector.

hyperbolic and elliptic IFSs are present, the total PF is obtained by the summation of

the two. Obliviously, the contribution of the elliptical branch is of the order of unity and is, thus, negligibly small relative to the hyperbolic one. The energy averaging in the denominator is over one period of HMMs, and $\nu'_{gx} = \omega^{-1}\partial\omega/\partial k'_x$ is the lateral group velocity normalized to the speed of the light in dielectric. From Eq. 2.32 there are three factors contribute to the PE: the field enhancement, wave vector and, most importantly, low group velocity. Fig. 2-5(a) shows the IFS when the metal and dielectric have the same thickness (TR = 1). Fig. 2-5(c) shows the spatial dependence of the PF, which reaches 25 for this configuration. To better observe the behavior of SPPs in HMMs, I choose two points on IFS. The first point is chosen with transverse wave vector $k_z = 0$, the fields and energy are shown in Figs. 2-5(c) and (d). We can see that magnetic field is symmetric inside the metal (similar to the so called "long-range" SPP mode in a slab waveguide [79, 80]), the energy is contained mostly inside the dielectric and the magnetic energy is about a factor of 2 less than electric energy. Meanwhile, we can see that the energy propagates in opposite directions in the metal and dielectric. The second point is chosen near the edge of BZ, the field and energy are shown by Figs. 2-5(d) and (f), the magnetic field now becomes antisymmetric inside the metal. It is known that, in slab waveguide this mode referred to as "short-range plasmon" [77], can extend to large lateral wave vectors but also suffers from large loss. We can see from Fig. 2-5(f) that nearly 50% of the energy is contained inside the metal, hence the loss is expected to be high [78]. Moreover, I also notice that $U_H \ll U_E$, which means that the energy balance in the mode is now maintained in a different way as the energy oscillates between the "capacitance" of the dielectric and the "kinetic inductance" of the moving free electrons in the metal. Naturally, the moving electrons always dissipate energy hand high loss ensues. Finally, note that in the virtual absence of a magnetic field, the Poynting vector is small and so should be the group velocity. Then according to Eq. 1.14, the modes with large k are expected to contribute disproportionally to the density of states and the PE. However, they are

also are expected to have higher loss and shorter propagation distances

2.2.3 Effective and Mean Parameters in HMM

In addition to the energy density and Poynting vector, for better insight into the physics of HMMs, it is helpful to define a number of the additional effective parameters. Here I define a number of k-vector dependent parameters, such as the effective mode loss

$$\gamma_{eff}\left(k'_z\right) = f_m\left(k'_z\right)\gamma_m\left(k'_z\right) \tag{2.33}$$

where $f_m = \int\limits_{-b}^{0} U'_T dz' / \int\limits_{0}^{a} U'_T dz'$ is the fraction of energy contained inside the metal; the effective impedance is defined as

$$\eta_{eff} = \int\limits_{-b'}^{a'} |E\left(z'\right)| dz / \int\limits_{-b'}^{a'} |H'\left(z'\right)| dz' \tag{2.34}$$

We can also use a different definition of the effective impedance

$$\eta_{eff} = \left[\int\limits_{-b'}^{a'} |E\left(z'\right)|^2 dz / \int\limits_{-b'}^{a'} |H'\left(z'\right)|^2 dz'\right]^{1/2} \tag{2.35}$$

but our calculation shows that the difference between them is insignificant as I only use effective impedance as a qualitative measure of the mode properties. Finally, the effective energy velocity is defined as

$$v'_{ex(z)} = \int\limits_{-b'}^{a'} S'_{x(z)}\left(z'\right) dz' / \int\limits_{-b'}^{a'} U'_T dz' \tag{2.36}$$

and the effective propagation length

$$L_{x(z)} = v'_{ex(z)} / \gamma_{eff} \tag{2.37}$$

can also be defined and the used to estimate the propagation of the coupled modes in HMMs. In addition to the effective parameters, I also reintroduce the differential PF, Eq. 2.32, it describes the relative contribution of the states, with a given transverse wave vector, to the density of states and the PE. Figure 2-6(a) shows the two

36
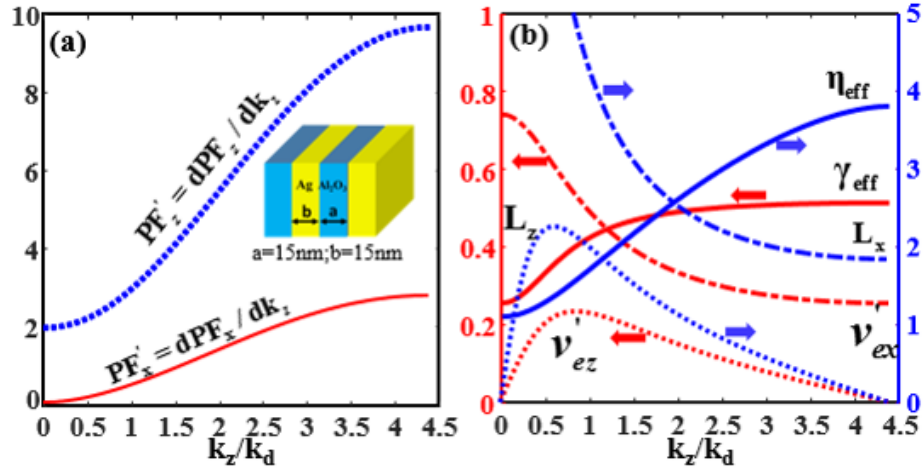
Figure 2-6. Change of (a) differential PF, and (b) effective parameters with wavevector at TR=1.

components of differential PF increase with the increase of the wave vector, especially when the emitting dipole is polarized along the z axis (which is no wonder given the TM character of the waves in HMMs). Figure 2-6(b) shows the change the defined effective parameters with wave vector. We can see that the effective loss and impedance increase with the wave vector, while the effective energy velocity and propagation length decrease with wave vector. Hence, most of the "additional" radiation caused by the PE actually couples into the lossy modes that do not propagate far, and, moreover, get reflected at the HMM surface due to their large effective impedance.

The effective parameters defined above provide us the information about each particular mode. However, according to Eq. 2.31, it is the modes with large wave vector that play the paramount role in the Purcell enhancement, most of the energy couples into those modes. So it is convenient to define a new set of parameters which would provide a measure of the properties of the average mode that gets excited in the HMMs by the emitter. Thus here I define the mean parameters by weighing the effective parameters over the Purcell enhancement, hence, the mean loss, mean

impedance, mean energy velocity, mean propagation length are defined as

$$\langle \gamma_{eff} \rangle = \int \gamma_{eff} PF' dk_z / \int PF' dk_z \qquad (2.38)$$

$$\langle \eta_{eff} \rangle = \int \eta_{eff} PF' dk_z / \int PF' dk_z \qquad (2.39)$$

$$\left\langle v'_{ex(z)} \right\rangle = \int v'_{ex(z)} PF' dk_z / \int PF' dk_z \qquad (2.40)$$

$$\left\langle L_{x(z)} \right\rangle = \int L_{x(z)} PF' dk_z / \int PF' dk_z \qquad (2.41)$$

Figure 2-7(a) shows the change of the PF calculated from EMT and KP model with TR. We can see that in the hyperbolic region the PF calculated by KP model in less than the PF predicted by the EMT. This is the result of derivation of the KP IFS from the perfect hyperbola. What's more interesting is that strong PF exists not only outside of the hyperbolic region, but is substantially higher there than in the hyperbolic region. Hence, PE appears to have very little to do with the nature of dispersion. Apparently, all the enhancement occurs "locally" and can be treated as enhancement by weakly coupled gap (metallic region) or slab (dielectric region) SPPs. The change of the mean parameters with TR is shown in Figs. 2-7(b) and (c), we can see that larger PF is always accompanied by higher loss and impedance, shorter propagation length and smaller velocity. The reason here is that the energy simply couples into the large k-vector waveguide modes traveling along the plane and that these modes are no different from the short-range modes in gap and slab SPPs. The emitter energy gets coupled into the kinetic motion of electrons in the metal and then dissipated. In essence, what is observed is simply a quenching of radiative lifetime of the emitter [81].
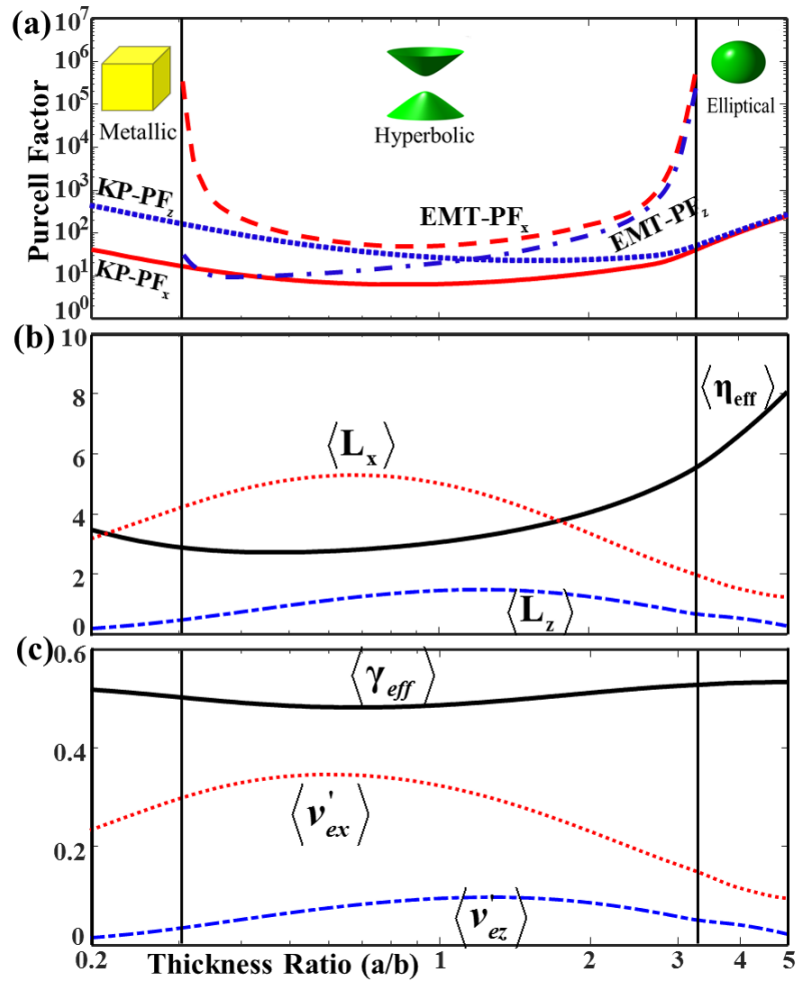
Figure 2-7. (a) Comparison of EMT PF with the results of the KP model. (b) Change of the mean loss and energy velocity with TR. (c) Change of the mean impedance and propagation length with TR.

2.2.4   Impact of Granularity

As mentioned in [47], the EMT does offer a good guidance for HMMs properties, yet fails to take their granularity into account. Figure 2-8(a) shows the IFS of HMMs for different periods when TR=1, and the granularity is defined as $G = (a+b)/\lambda_d$. Here we can see that the IFS is strongly dependent on the granularity. For smaller granularity, the IFS get closer to the IFS of EMT, but for large k wave vector, the difference persists. Figure 2-8 shows the relation between the maximum in the dielectric and the granularity for the same TR as in Fig. 2-8. As expected, extension of the BZ increase the density of states and PF. But as discussed above, the "new" large wave vector states are the ones with larger loss. Hence, while the radiative lifetime is expected to shorten even further with a decrease in period, the external efficiency would also decrease. In essence, shortening the period will only increase the quenching.
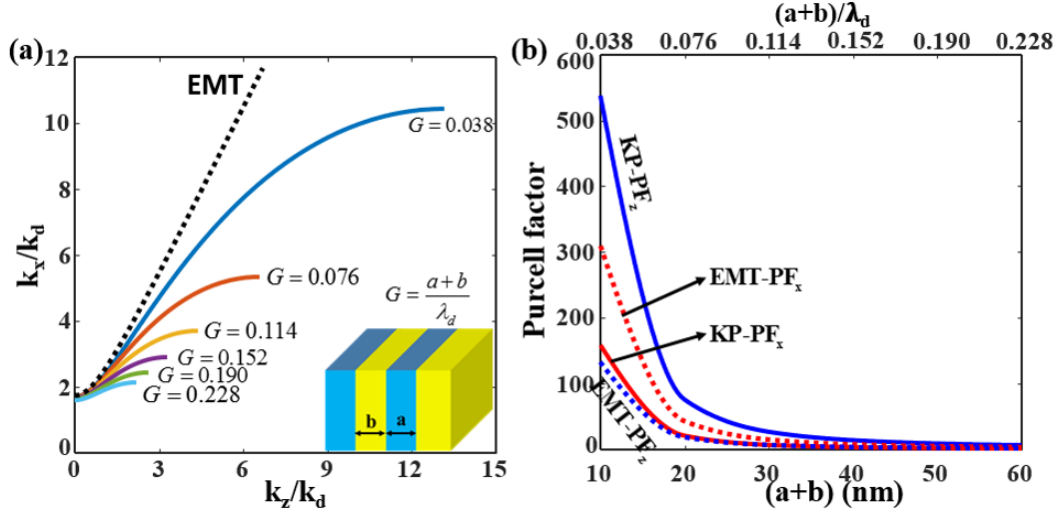
Figure 2-8. (a) IFS for different periods. (b) Change of maximum PF for the two components of the emitting dipole in the dielectric with granularity.

2.2.5   Comparison With Slab and Gap SPPs

As I pointed above, the SPP modes in HMMs sometime are similar to the SPP modes in dielectric gap and metal slab waveguide. Here I compare the HMMs with

dielectric gap and metal slab plasmonic waveguide, referred to as gap and slab SPP waveguide,respectively. This issue was first addressed recently in [65], where it has been shown that one can always obtain a density of states that is as large as that of HMMs using just a single metallic layer. Here I expand on this treatment and demonstrate that depending on the TR, the HMMs can be shown to be nothing but coupled gap and slab SPPs and that not just the density of states bit virtually all the characteristics of HMMs are no different from SPPs. Unlike [65], our model does not rely on numerical calculation. Figure 2-9(a) shows the comparison of the fields (left) and PF (right) of the HMM (top) and the gap SPP waveguides (bottom). We can see that the fields are quite similar, with the normal electric field confined strongly inside the dielectric gap, leading to strong PE. The only difference is that, for the gap SPP waveguide, a smaller thickness is required to achieve the same PF with HMMs. The comparison between HMM (top) and slab SPP waveguide (bottom) in Fig. 2-9(b) follows the same story line, except that the resemblance is ever stronger. It is important to notice that the magnetic field inside that metal slab changes sign, indicating that the mode is antisymmetric or so-called short-range SPPs [77]. Therefore, one can say that as TR increases and layered material changes its character from metallic to hyperbolic to elliptical (dielectric), the nature of the "hyperbolic" or "large-k-vector" mode gradually changes from the symmetric mode of the gap SPPs to the antisymmetric mode of the slab SPPs. We can also see that the elliptical (small k-vectors) mode corresponds to the long-range or symmetric slab SPP mode.

Figure 2-10 shows the calculation of the PF and effective parameters of short-range slab (Figs. 2-10(a)-(c)) and long-range gap SPPs (Figs. 2-10(d)-(f)). As expected, as the thickness of the metal layer in the slab SPPs decreases the PF increases, because the mode gets more confined and the group velocity decrease. It is easy to see that, by reducing thickness, we can always match and surpass the PF in HMMs, which is similar to the main conclusion of [65]. Similarly, PF of the gap SPP mode increases with the
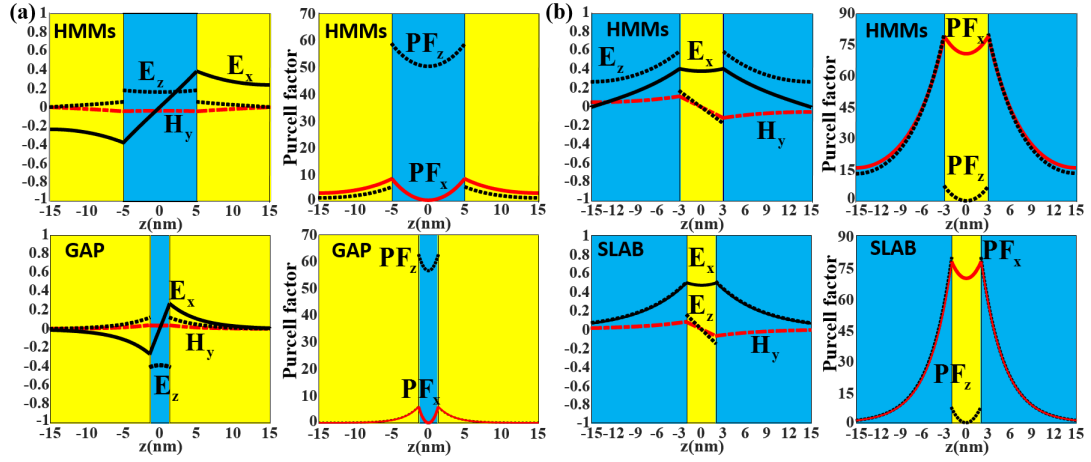
Figure 2-9. Comparison of HMMs with (a) a dielectric gap waveguide (b) and a metal slab waveguide.
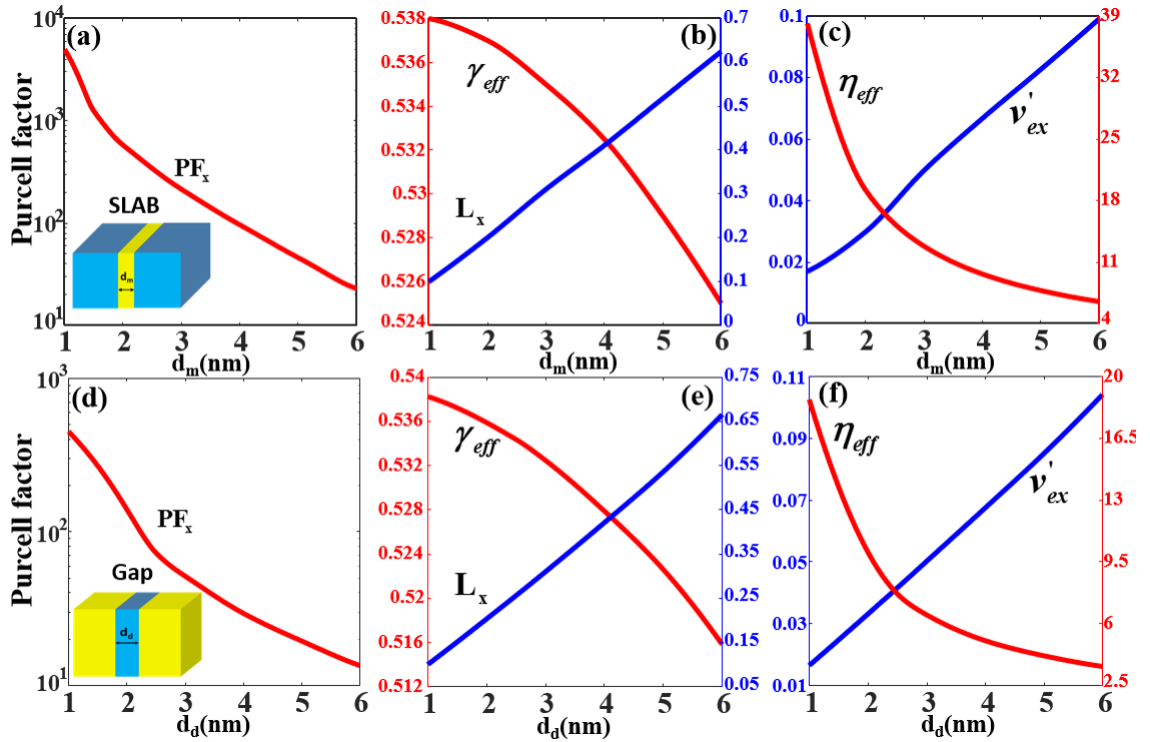
Figure 2-10. Change of PF and effective parameters of a metal slab and a dielectric gap with thickness of the middle layer. (a), (d) PF; (b), (e) propagation length and effective loss; (c), (f) energy velocity and effective impedance.

decrease of the thickness of the dielectric spacer. Just as in HMMs, this increase of PF is always accompanied by rapid decrease in propagation length and increase of effective impedance, indicating that what appears to be a genuine enhancement of the emission is in reality just a quenching. Going beyond the conclusion of [65] and to further confirm the similarity between HMM and SPP waveguides, I have also calculated and compared their dispersion curves. In Fig. 2-11, the IFS at $\lambda = 500$nm for the 24nm Al$_2$O$_3$/6nm Ag layered structure is shown with both elliptic and hyperbolic branches present at this wavelength, By fixing the normal component of the wave vector at $k_z' = 0.4$ (vertical dashed line in Fig. 2-11), we can find that values of the lateral wave vector for the range of frequencies from 0 to $1.25\omega_{sp}$, where $\omega_{sp} = \omega_p/\sqrt{1 + \epsilon_d}$ is the surface plasma frequency, and produce the lateral dispersion curves Fig. 2-11, which look remarkably similar to the dispersion curves of slab SPPs shown in Fig. 2-11(c). The upper branch, which, depending on wavevector, can correspond to elliptical or hyperbolic IFS, obviously originates from the coupled long-range (symmetric) slab SPP modes. The lower branch, always hyperbolic in nature, corresponds to the short-range (antisymmetric) mode. On the other hand, by fixing the lateral component of the wave vector at $k_x' = 0.8$ (horizontal dashed line in Fig. 2-11), I obtain the dispersion curves in the normal direction, as in Fig. 2-11, which looks precisely how one would expect to see weakly coupled modes of slab SPPs waveguides. Using a condensed matter analogy, in this tight binding approximation, the elliptical curve looks like a "conduction band" and the hyperbolic curve like a "valence band". The curvature of the hyperbolic band is much smaller than that of the elliptical band, indicating low velocity of propagation and larger PE.

2.2.6 Bandwidth of PE

One of the purported advantage of HMMs is that strong PE can be achieved over a wide range of frequency [33, 58], unlike the enhancement s near the single met-
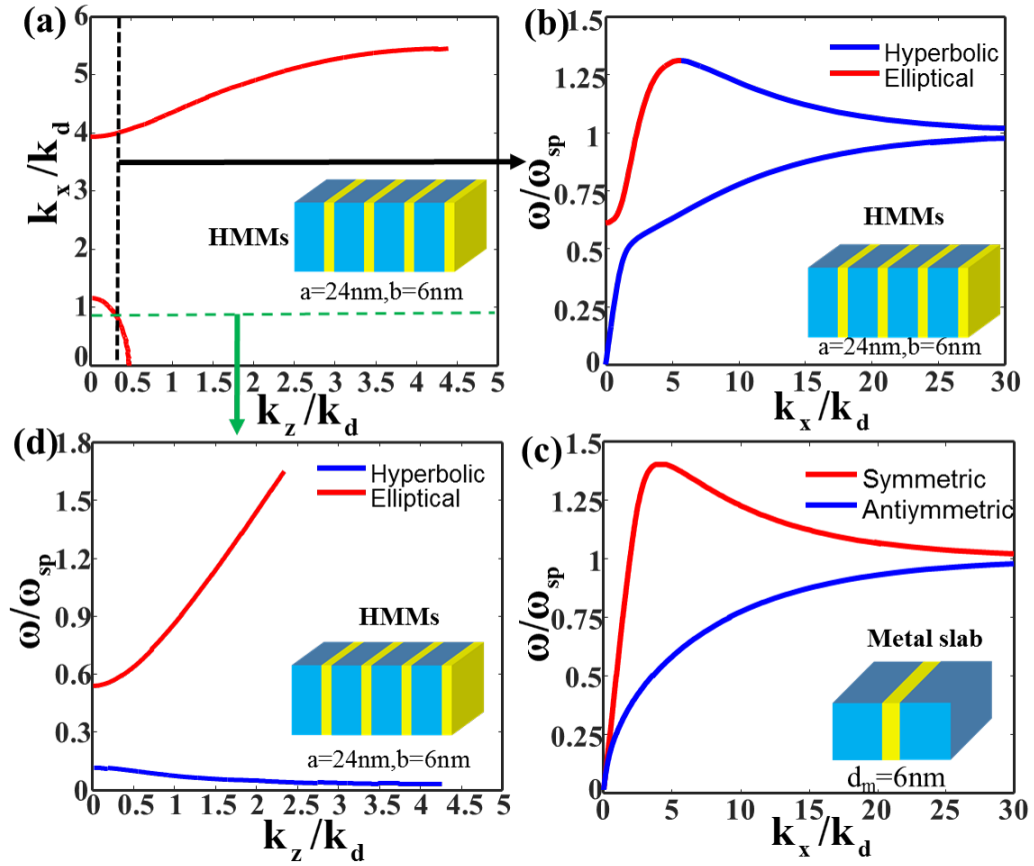
Figure 2-11. (a) IFS at $\lambda = 500\mathrm{nm}$ nm when the thickness of the dielectric and metal are 24 and 6 nm, respectively. (b) Lateral dispersion relation for HMMs in (a). (c) Dispersion relation of a metal slab waveguide when the thickness of the metal is 6 nm. (d) Normal dispersion relation of HMMs in (a).

al/semiconductor interface that are attainable only in the vicinity of surface plasmon resonance. Figure 2-12 shows the change of PF of HMMs (red solid line), slab SPP waveguide (blue dotted line) and gap SPP waveguide (green dashed line) with frequency. We can see that wide range and strong PE can also be achieve by gap SPP and metal SPP waveguide. Hence, we can easily engineer the PF over a broad wavelength range by simply varying the thickness of slab and gap SPP waveguides without resorting to fabrication of a multilayer structure. Here I stress the fact that most of the enhancement amounts to the quenching of radiative lifetime. Note also that in both HMMs and SPPs, we can increase out coupling of the high impedance modes with high k to some degree by using a grating or simply a rough surface with virtually identical results [82].

It is also interesting to see how many alternating metal/dielectric layers are required to fully achieve HMM behavior. I have performed the analysis using the transfer matrix method (TMM) and found that, after about eight periods, the characteristics of the structure no longer change, as shown in Fig. 2-13. But, as shown above, the same characteristics can also be obtained with just alternating layers in either a gap SPP or short-range slab SPP configuration.

2.2.7 Physical origin of PE

Extensive discussion of the characteristics of HMMs has led us to an unavoidable conclusion: the large wavevectors and, consequently, large density of states in these materials are all accompanied by large loss in the metal. In that respect, HMMs are no different from simple slab and gap SPPs, and, furthermore, the densities of states get larger only in the regions where the metamaterial is nominally "metallic" or "elliptical", i.e., they have very little to do with the "hyperbolicity". This conclusion is, of course, only logical as long as one accepts the obvious fact that the quantum "states" do not appear out of nowhere and their density can be altered only by coupling
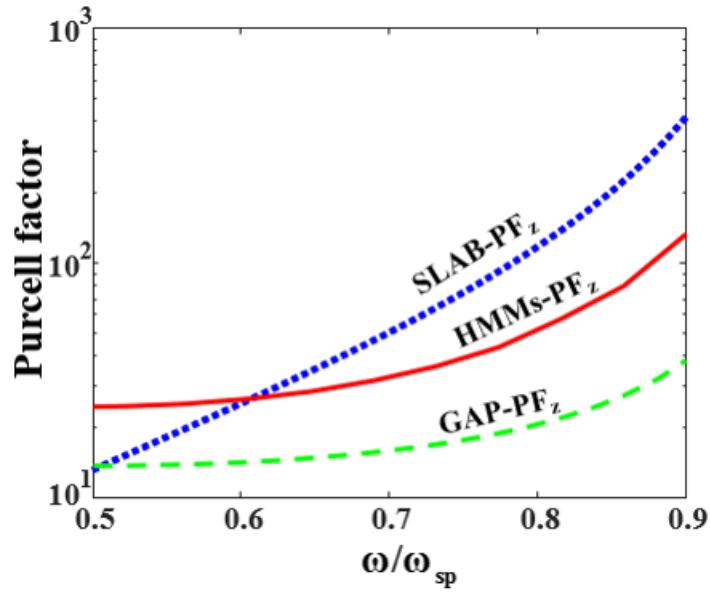
Figure 2-12. Change of PF with frequency for HMMs ($a = 24nm; b = 6nm$) (red solid line), metal slab ($d_m = 6nm$) SPP waveguide (blue dotted line), and dielectric gap waveguide ($d_d = 6nm$) (green dashed line).
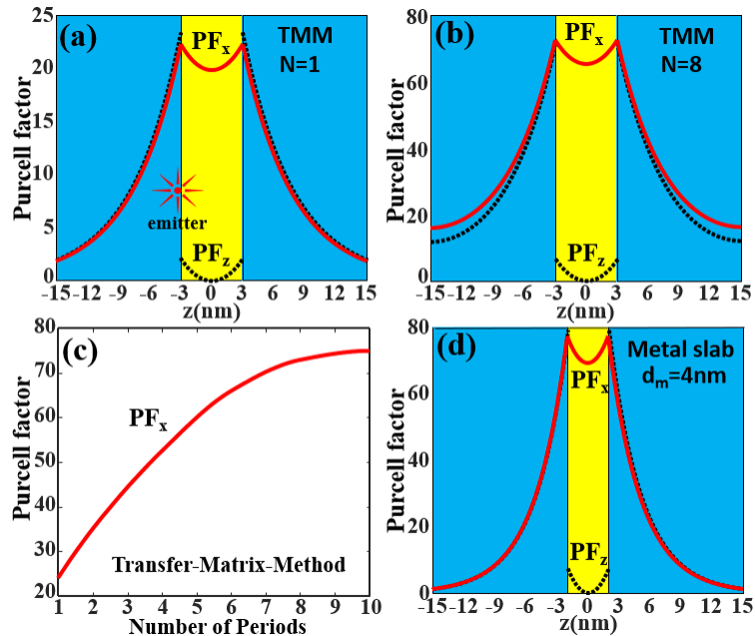
Figure 2-13. (a), (b) PF calculated using the transfer-matrix-method for different periods. (c) Change of PF with the increase of periods. (d) PF obtained with a metal slab with smaller thickness can be the same as HMMs in Fig. 2-9(b) (top).

46

between the different states. In this respect, the density of photons always remains the same and it changes inside the dielectric medium only because the photons couple with the polarization oscillations of atoms or molecules forming polaritons. This essentially adds the "degrees of freedom". In plasmonic structures, including HMMs, the photons couple with the collective oscillations of free carriers in the metal.
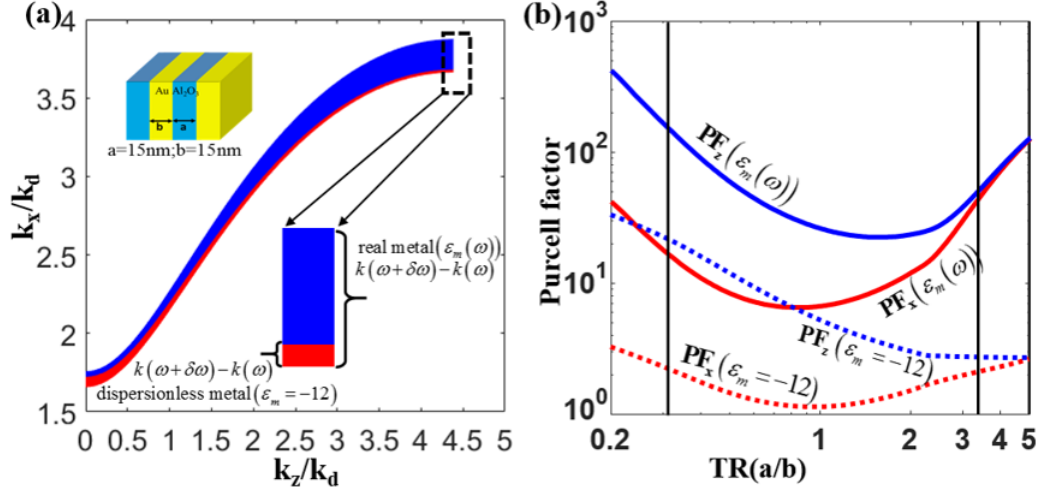
Figure 2-14. Comparison of (a) IFS and (b) PF of the HMMs with real metal and hypothetical dispersionless metal indicates that most of the density of states and PE originate from the metal dispersion.

The density of states for free electrons near the Fermi energy is roughly 8 orders of magnitude higher than the density of photons, mostly because the electron velocity is much slower than the speed of light. As a result, new coupled plasmon–polariton modes have a much larger density of states. In other words, the giant PF in any plasmonic structure including HMMs is simply the consequence of having large density of free carriers. To check this conjecture, I first note that the presence of a large number of moving free carriers is manifested by the large "normalized group dielectric constant" $\epsilon_g' = \epsilon_d^{-1} \partial(\omega \epsilon_m)/\partial \omega \approx \epsilon_d^{-1} \omega_p^2/\omega^2$. It is this large derivative that causes plasmon polaritons to propagate slowly, which, in turn, leads to large density of states and PF. What if one considers a hypothetical material with negative permittivity equal to that of actual metal ($\epsilon_m = -12$) but dispersionless in the region of interest

(such material of course cannot exist because the electric field energy in it would be negative)? I plot two IFSs separated by small frequency interval $\delta\omega = 0.9\%\omega_{\mathrm{sp}}$ of this HMM made up of "dispersionless metal" in Fig. 2-14(a), next to the IFS of the HMMs made up of real Ag, whose permittivity has dispersion. The difference is dramatic—for real Ag the two curves diverge at large wavevectors, while for the dispersionless metal the IFS converges. This is expected even in EMT, where without dispersion, hyperbolic IFSs of all frequencies converge to the same asymptote. As a result, the density of states without dispersion decreases dramatically, and, as shown in Fig. 2-14(b), so does the PF. One can see that about 90% of the giant PE comes simply from coupling of the emitter's energy into the kinetic motion of free electrons and owes preciously little to exactly how the layers are arranged. Needless to say, once the energy is coupled into the collective motion of free carriers, it dissipates at the femtosecond rate and, thus, giant PF usually indicates a quenching of radiative lifetime. This discussion of the origin of giant PE in layered HMMs is also relevant to the natural HMs, such as hexagonal BN [83], where the modes with large wavevectors are, of course, nothing but phonon polaritons in which the energy is contained mostly not in the form of an electromagnetic field but in the form of ionic vibrations (optical phonons). In other words, the energy of the emitter placed inside natural HMs is coupled directly into ionic vibrations. The ionic vibrations are of course damped, albeit not as strongly as free electrons (picoseconds versus tens of femtoseconds), but then the density of states of these vibrations is also less than the density of free electrons at the Fermi level. Hence, the basic trade-off between the large density of states and low loss is maintained in this material, as well.

2.3 Conclusions

In this work I have investigated the optical properties of sub-wavelength layered metal/dielectric structures, also known as hyperbolic metamaterials, using an exact,

straightforward, and fully analytical KP model. On the one hand, I have revealed a number of important features that have not been previously given proper attention. First of all, not only, as previously noted in [47], can hyperbolic and elliptical IFSs co-exist, but hyperbolic IFSs can exist for all combinations of layer permittivities and thicknesses. Most importantly, the largest PE of spontaneous radiation is achieved away from the hyperbolic region. Second, I demonstrate that large wavevectors and PE in layered plasmonic structures are inextricably tied to the loss, slow group velocity, small propagation distances, and large impedances. This indicates that the much heralded PE in the HMMs is actually direct coupling of the energy into the free electron motion in the metal, commonly known as quenching of radiative lifetime. There are far easier and well proven ways to modify the luminescence time, such as adding defects and using low-temperature-grown materials [84]. Third, looking deeper into the physics of PE in HMMs shows that it has very little to do with the hyperbolicity per se and everything to do with the large dispersion of permittivity in the metals or polar dielectrics, as our conclusions are relevant also for the naturally infrared HMs occurring in nature. Finally, by offering detailed analysis and comparison of field distribution, dispersion, PF, bandwidth of the PE, and the guide mode in metal/dielectric SPP waveguides, I not only demonstrate that HMMs are nothing but weakly coupled SPPs modes, but that the PE in HMMs can be achieved by using simple dielectric gap and metal slab SPP waveguides, and their bandwidths are equally broad.

Chapter 3

The limits of imaging with multi-layer hyperbolic metamaterials

3.1 Introduction

In this chapter, I study the metal-dielectric layered hyperbolic metamaterial's ability to get high-resolution image. From the previous chapter, we know that hyperbolic metamaterial can support very large propagating wave vector due to their special iso-frequency surface. Hence, hyperbolic metamaterial is a good candidate to break the diffraction limit and obtain high-resolution image. For the conventional imaging process based on traditional optical devices, such as lenses, the resolution limited by the diffraction limit due to the loss of fine details, the fine details are carried by evanescent waves with large vector. For hyperbolic metamaterial, suppose a point source is placed near it, the emitted evanescent waves with large in-plane wave vector can excite propagating modes inside hyperbolic metamaterial, and final, the modes will transfer the near-field information to the other side of hyperbolic metamaterial, which is the image space.

Based on this point, the realization of such a configuration using hyperbolic metamaterials has been suggested to achieve a "hyperlens". Hyperlens designed to

enhance its imaging abilities have been investigated in several studies [35, 40, 85, 86]. A hyperlens works for terahertz frequencies that is based on a fan-like arrangement of graphene sheets has been proposed, and other hyperlenses have been experimentally realized for acoustic waves and in the microwave, optical and near-ultraviolet regions. The hyperlens consists of a curved stack of alternating Al_2O_3 and Ag layers that are 35nm thick. To create a subwavelength object, the word "ON" was inscribed on a 50nm thick chrome layer deposited on the inner surface of the hyperlens. The object was illuminated with a laser beam (central wavelength is 365nm with linewidth 10nm). The far-field image was focused onto the image plane by a conventional lens. Based on this experimental configuration, a subwavelength resolution of 130nm was achieved. From that on, many similar hyperlenses have been achieved. Meanwhile, hyperlenses were also modeled extensively, but most of the models are numerical and failed to reveal the physical reasons that eventually limit the resolution. This work
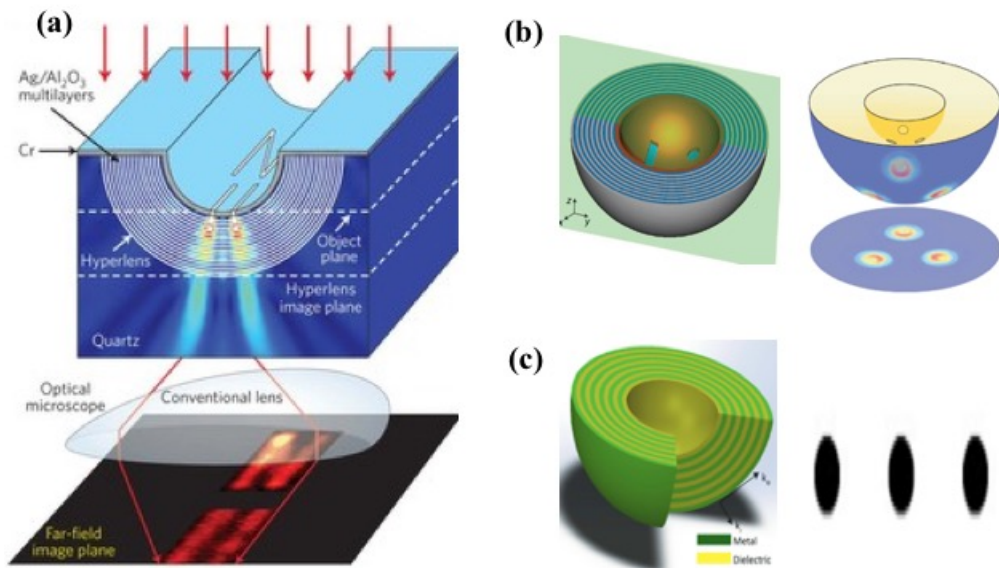
Figure 3-1. (a) Hyperlensing experiment configuration; (b) Schematic of a spherical hyperlens comprised of nine pairs of silver and titanium oxide layers [40]. (c) multi-layered spherical hyperlens structure. Metal and dielectric thin films are deposited on a spherical shape of substrate [87].

is based on our previously developed "eigen-mode" model for superlens in which the

whole phenomenon of "superlensing" was explained as the coupling of light scattered (or emitted) by the sub-wavelength features of the object into the surface plasmon polaritons modes of the metal slab and their subsequent combining into the image on the other side of the slab. The destructive interference between symmetric and antisymmetric modes was shown to suppress the optical transfer function (OTF) at large spatial frequencies and thus limiting the resolution of superlens. More recently, I have studied hyperbolic materials and shown that their eigen-modes are nothing but coupled SPPs modes which exist in any multi-layer metal-dielectric structure, irrespective of their classification as hyperbolic or non-hyperbolic as per the effective medium approximation.

Armed with this knowledge, we can now extend our eigen-mode model to the image-forming multi-layer structures, which for the sake of generality we shall refer to as "plasmonic lenses" and explore their limitations. Although in this work I only consider the flat structures, the main conclusions can also be applied to the cylindrical hyperlens. While the eigen-mode approach is indispensable for revealing the physics behind performance of the plasmonic lens, the same outcomes can be essentially achieved using several numerical methods. One such technique is the Transition Matrix Method (TMM) that we have employed in numerous examples later explained using the eigen-mode theory.

3.2   The Eigen-mode Approach

In this work, I estimate the quality and resolution of image obtained through a multi-layer hyperlens, by applying the "eigen-mode" model, which was developed in our group for hyperlens consists of only one metal layer, to the hyperlens consists of multi-layers. Through the "eigen-mode" model, we know that the phenomenon of "superlensing" can be explained as the coupling of light scattered (or emitted) by the sub-wavelength features of the object into the surface plasmon polaritons (SPPs)

modes of the metal slab and their subsequent combining into the image on the other side of the slab. The destructive interference between symmetric and antisymmetric modes was shown to suppress the optical transfer function (OTF) at large spatial frequencies and thus limiting the resolution of superlens. In the last chapter, I have studied hyperbolic metamaterials and showed their eigen-modes are nothing but coupled SPPs, which exist in any multi-layer metal-dielectric structure, irrespective of their classification as hyperbolic or non-hyperbolic as per the effective medium approximation.

In this section, based on the previously developed "eigen-mode" model and our study about HMMs, I extend our eigen-mode model to the image-forming multi-layer structures, which for the sake of generality we shall refer to as "plasmonic lens" and explore their limitations. Although in this work we only consider the flat structures, the main conclusions can also be applied to the cylindrical hyperlens. While the eigen-mode approach is indispensable for revealing the physics behind performance of the plasmonic lens, the same outcomes can be essentially achieved using several numerical methods. One of such technique is the Transition Matrix Method (TMM) that we have employed in numerous examples later explained using the eigen-mode theory.

The eigen-mode approach is built based on a simple principle: the energy of the object, when treated here as a superposition of oscillation dipoles, can only be coupled into the physical eigen-modes of the system. Hence, if the system is capable of supporting the "sub-wavelength" modes with wave vectors (spatial frequencies) k exceeding the diffraction limit $2\pi n/\lambda$, then a subwavelength image can be formed by superposition of these modes. The The structures incorporating metal layers are obviously capable of supporting such large k-vector modes, called surface plasmon polaritons (SPPs). In the multi-layer structures, such as one shown in Fig. 3-2, these modes couple with each other to give rise to the so-called supermodes extending

throughout the entire structure.
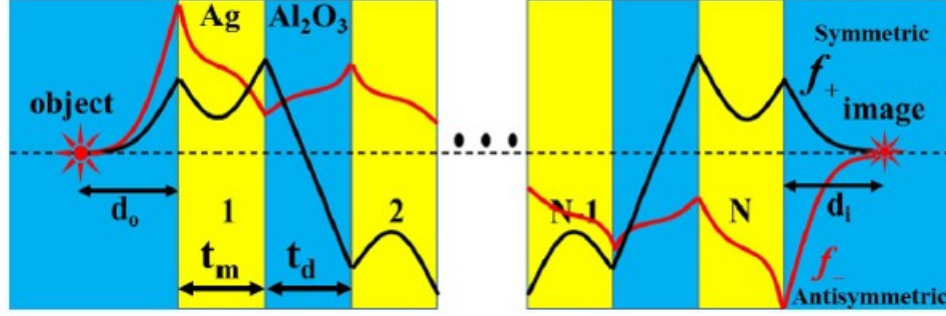
Figure 3-2. Symmetric and antisymmetric eigen modes in multi-layers hyperbolic metamaterials contain N metal layers with thickness t_m and separated by dielectric with distances t_d. d_o and d_i are the distance between object, image and hyperbolic metamaterials.

Figure 3-2 shows an example of plasmonic lens containing N metal layers with complex permittivity $\epsilon_m = \epsilon'_m + i\epsilon''_m$, where ϵ'_m and ϵ''_m are the real and imaginary parts respectively, and thickness t_m separated by dielectric with permittivity ϵ_d and thickness t_d, and is capable of supporting $N+1$ coupled SPPs eigen-modes $f_k^n(z)\exp(i k \cdot r - \omega_n t)(n = 1, 2, 3 \cdots N + 1)$ where k is the in-plane wave vector. Each eigen-mode contains in-plane and and out of plane contributions and has a dispersion relation $\tilde{\omega}_n(k) = \omega_n(k) + i\gamma_n(k)$ which connects the complex eigen-mode resonant frequency $\tilde{\omega}_n$ with the real in-plane wave vector f; and the imaginary part frequency $\gamma_n(k)$ is the effective loss rate estimated via the ratio of energy in metal to the total energy in the multi-layer structure. Each of the eigen-modes is a solution of the homogeneous wave equation.

$$\left[\frac{\partial^2}{\partial z^2} - k^2 + \epsilon(z, \omega)\epsilon_0 \frac{(\tilde{\omega}_n)^2}{c^2} \right] \boldsymbol{f}_k^n(z) = 0, \tag{3.1}$$

For the convenience of calculation, the eigen-modes are normalized as $\int_{-\infty}^{\infty} \boldsymbol{f}_k^n(z)^* \boldsymbol{f}_k^m(z) = \delta_{mn}$. For the most general case, the object can be treated as an amplitude mask, phase mask or fluorescence object, all of which can be represented as a superposition of the oscillating electric dipoles $p(\boldsymbol{r}, z, t)$ in the object plane, which can be expressed as a

Fourier series,

$$p(\boldsymbol{r}, z, t) = e^{i\omega t}\delta(z_0 - z)\int\limits_k \boldsymbol{p_k}e^{i\boldsymbol{k}\cdot\boldsymbol{r}}d\boldsymbol{k}, \tag{3.2}$$

where z_0 is the object distance and p_k is the polarization of dipoles, hence the wave equation of the system is,

$$\nabla^2\boldsymbol{E}(\boldsymbol{r}, z, t) - \epsilon(z,\omega)\epsilon_0\mu_0\frac{\partial^2}{\partial t^2}\boldsymbol{E}(\boldsymbol{r}, z, t) = \omega^2\mu_0\boldsymbol{p}(\boldsymbol{r}, z, t), \tag{3.3}$$

The electric field can be represented as a superposition of all the eigen-modes at different in-plane wave vectors

$$\boldsymbol{E}(\boldsymbol{r}, z, t) = e^{i\omega t}\int\limits_0^\infty\sum_{n=1}^{N+1}C_k^n(\omega)\boldsymbol{f}_k^n(z)e^{i\boldsymbol{k}\cdot\boldsymbol{r}}d\boldsymbol{k}, \tag{3.4}$$

Then by substituting Eqs. 3.2 and 3.4 into Eq. 3.3 one obtain the time-independent set of equations for each lateral wave vector k,

$$\sum_{n=1}^{N+1}C_k^n\left[\frac{\partial^2}{\partial z^2} - k^2 + \epsilon(z,\omega)\epsilon_0\frac{\omega^2}{c^2}\right]\boldsymbol{f}_k^n(z) = \omega^2\mu_0\boldsymbol{p_k}\delta(z - z_0). \tag{3.5}$$

By substituting Eq. 3.1 into Eq. 3.5 one can now obtain,

$$\sum_{n=1}^{N+1}C_k^n\left[\epsilon(z,\omega)\epsilon_0\omega^2/c^2 - \epsilon(z,\omega)\epsilon_0(\widetilde{\omega}_n)^2/c^2\right]\boldsymbol{f}_k^n(z) = \omega^2\mu_0\boldsymbol{p_k}\delta(z - z_0), \tag{3.6}$$

and then, by multiplying $f_k^m(z)^*$, integrating over z-axis, and using orthogonality condition, the amplitudes of each mode can be founds as,

$$C_k^n = \frac{\omega^2}{\omega^2 - \widetilde{\omega}_n^2}\frac{p_k}{\epsilon_0}f_k^n(z_0). \tag{3.7}$$

So, the total field in the image space with distance z_i from the system can be collected by detector is,

$$\boldsymbol{E}(z_i) = \int\limits_{|k|>k_{0,n}}\left[\frac{\omega^2}{\omega^2 - \widetilde{\omega}_n^2}\frac{p_k}{\epsilon_0}\boldsymbol{f}_k^n(z_0)^*\right]\boldsymbol{f}_k^n(z_i)e^{-i\boldsymbol{k}\cdot\boldsymbol{r}}d\boldsymbol{k} + \int\limits_{|k|<k_0}e^{i\boldsymbol{k}\cdot\boldsymbol{r}}E_k(z_i)d\boldsymbol{k}. \tag{3.8}$$

And the OTF for the sub-wavelength spatial frequencies becomes,

$$OTF(\boldsymbol{k}, z_0, z_i) = \sum_{n=1}^{N+1}\frac{\omega^2}{\omega^2 - \widetilde{\omega}_n^2(\boldsymbol{k})}\boldsymbol{f}_k^n(\boldsymbol{k}, z_0)^*\cdot\boldsymbol{f}_k^n(\boldsymbol{k}, z_i). \tag{3.9}$$

Since the two dimensional OTF does not depend on the choice of in-plane coordinate axes x and y, it can be always be found as a product of two one-dimensional OTF, $\text{OTF}(\boldsymbol{k}, z) = \text{OTF}(k_x, z) \times \text{OTF}(k_y, z)$. In the following discussion, I shall describe one-dimensional $\text{OTF}(\boldsymbol{k}, z_0, z_i)$, where $\boldsymbol{k}$ can be either k_x or k_y.

A dimensionless point object's image, which can describe the resonance of the imaging system is called point spread function (PSF) and can be easily calculated by using OTF,

$$PSF(x) = \int_k e^{ikx} E_{k,imag} dk \sim \int_k e^{ikx} OTF dk. \tag{3.10}$$

The eigen-mode approach outlined there presents a clear picture of the sub-wavelength image formation and the expression Eq. 3.6 elucidates the two most important features responsible for the image quality. The first feature is the resonant character of energy transfer from the object into the image highlighted by the denominator of Eq. 3.9. One should expect to see some peaks in OTF whenever the resonant coupling in one of the eigen-mode takes place. The second feature is the fact that the terms in Eq. 3.9 tend to change sign depending on the parity of the eigen-modes hence a fair amount of cancellation (destructive interference) takes place in the image space causing the suppression of the OTF and resulting in image deterioration.

3.3 Transfer-Matrix-Method Derivation
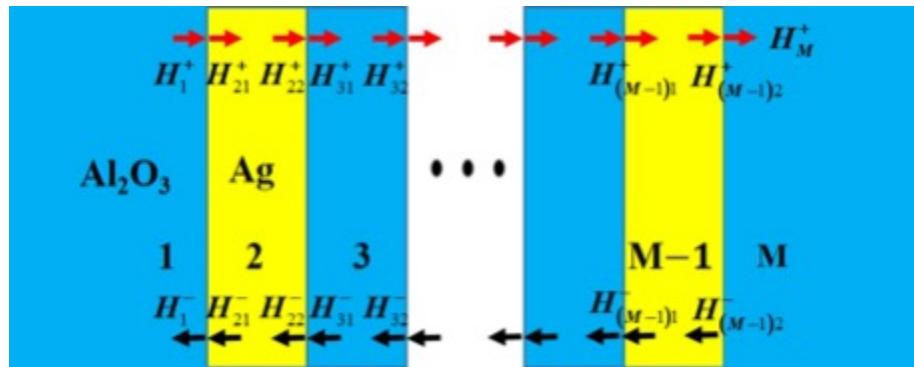
Figure 3-3. Configuration of multilayer metal/dielectric superlens.

Despite the fact that we have developed the eigen-mode approach, it is easier to calculate the OTF by a more direct transfer matrix method (TMM) which can be easily calculated for any spatial frequency, including the small ones corresponding to propagating (rather than evanescent) waves and thus not easily describable by the eigenmode model. Therefore, we can use TMM to calculate OTF and the eigenmode model to explain its feature. The following is a concise description of the TMM applied to the multilayer structure that contains M total layers (N metal layers and M-N dielectric layers) as shown in Fig. 3-3, it has 2N metal/dielectric interfaces. Due to the existence of reflection at every interfaces, there are both right and left going waves inside the multilayer superlens, indicated by $'+'$ and $'-'$ respectively. For transverse magnetic (TM) mode, we use the magnetic field component H_y , whose polarization is along the interface and is continuous inside the structure, to help us build the matrices. As shown in Fig. 3-3, the subscripts show the layer number and the interface in the present layer, the superscripts show the direction of the wave. For example, H_{21}^+ indicates the right going wave at the first interface in the second layer. Inside each layer, the tangential magnetic fields are the superposition of the right and left going plane waves, i.e. $\mathbf{H} = \mathbf{H}^+ + \mathbf{H}^-$. The propagating waves inside every layer and at each interface are connected by 2×2 matrices. The defined dynamic matrix D relates the fields on two sides of each interface. The dynamic matrices for propagating wave from dielectric to metal (Dd!m) and from metal to dielectric ($D_{m \to d}$) are shown in Eq. 3.11 and Eq. 3.12:

$$D_{d \to m} = \begin{bmatrix} \left(\frac{1}{2} + \frac{\epsilon_m(f)K(k,f)}{2\epsilon_d Q(k,f)}\right) & \left(\frac{1}{2} - \frac{\epsilon_m(f)K(k,f)}{2\epsilon_d Q(k,f)}\right) \\ \left(\frac{1}{2} - \frac{\epsilon_m(f)K(k,f)}{2\epsilon_d Q(k,f)}\right) & \left(\frac{1}{2} + \frac{\epsilon_m(f)K(k,f)}{2\epsilon_d Q(k,f)}\right) \end{bmatrix} \tag{3.11}$$

$$D_{m \to d} = \begin{bmatrix} \left(\frac{1}{2} + \frac{\epsilon_d Q(k,f)}{2\epsilon_m(f)K(k,f)}\right) & \left(\frac{1}{2} - \frac{\epsilon_d Q(k,f)}{2\epsilon_m(f)K(k,f)}\right) \\ \left(\frac{1}{2} - \frac{\epsilon_d Q(k,f)}{2\epsilon_m(f)K(k,f)}\right) & \left(\frac{1}{2} + \frac{\epsilon_d Q(k,f)}{2\epsilon_m(f)K(k,f)}\right) \end{bmatrix} \tag{3.12}$$

where ϵ_m and ϵ_d are the permittivities of metal and dielectric; $K = (k^2 - \epsilon_0 k_0^2)^{1/2}$ and $Q = (k^2 - \epsilon_m k_0^2)^{1/2}$ are the decay constants in dielectric and metal, respectively.

k_0 is the wavevector in vacuum.

For the fields inside each layer, we write the propagation matrices for dielectric (P_d) and metal (P_m) respectively, as shown in Eq. 3.13 and Eq. 3.14,

$$P_d = \begin{bmatrix} exp(K(k,f)t_d) & 0 \\ 0 & exp(-K(k,f)t_d) \end{bmatrix} \tag{3.13}$$

$$P_m = \begin{bmatrix} exp(Q(k,f)t_m) & 0 \\ 0 & exp(-Q(k,f)t_m) \end{bmatrix} \tag{3.14}$$

where t_m and t_d are the thickness of metal and dielectric. With the dynamic and propagation matrices, we can connect the electric field in the object and image space:

$$\begin{bmatrix} E_{xn}^+ \\ E_{xn}^- \end{bmatrix} = D_{m \to d}(k,f)P_m(k,f) \overset{N metal layers}{\cdots} P_m(k,f)D_{d \to m}(k,f) \begin{bmatrix} E_{x1}^+ \\ E_{x1}^- \end{bmatrix}$$
$$= \begin{bmatrix} M_{11}(k,f) & M_{12}(k,f) \\ M_{21}(k,f) & M_{22}(k,f) \end{bmatrix} \begin{bmatrix} E_{x1}^+ \\ E_{x1}^- \end{bmatrix} \tag{3.15}$$

One can obtain the eigen-solutions f_n^k from Eq. 3.15 by imposing the condition of no input wave ($E_{xn}^+ = E_{x1}^- = 0, \epsilon_m'' = 0$), i.e. $M_{11}(k;f) = 0$ to find the dispersion relations and then eigenfunctions themselves for using these solutions to explore the physics of imaging in the multilayer structure as described in the main text. At the same time, one can obtain OTF directly as ($\epsilon_m'' \neq 0$),

$$OTF(k,f) = \frac{E_{img}}{E_{obj}} = \frac{1}{M_{11}(k,f)}, \tag{3.16}$$

Figure 3-4 demonstrates that the two approaches do give similar results which only start deviating from each other at large wave-vectors where the SPPs are highly damped.

3.4 Results and discussion

3.4.1 Effect of Number of Metal Layers and Metal Loss

First, I solve numerically using TMM to obtain the SPP eigen-mode profiles and the dispersion as shown in Fig. 3-5. I use an example of the standard hyperbolic
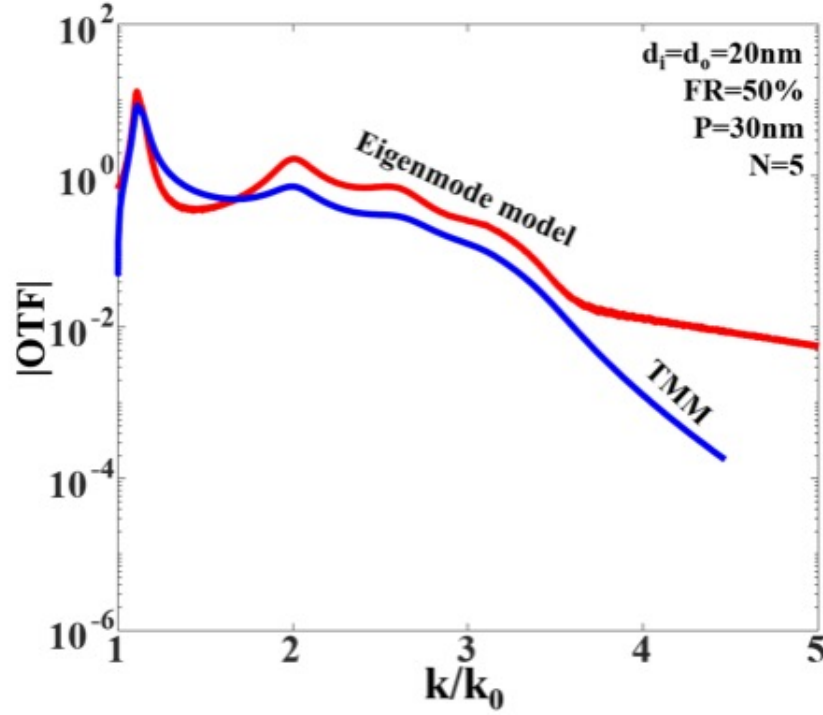
Figure 3-4. Comparison of the calculated OTF with eigenmode model and TMM.

metamaterial consisting of alternating 15nm layers of silver and aluminum oxide, which means the metal fill ratio ($FR = t_m/(t_m + t_d)$) is 50%, and the length of one period is 30nm ($P = 30$nm). The permittivity of Ag, is described by the Drude model $\epsilon_m = 1 - f_p^2/(f^2 + i\gamma f)$, where the plasma frequency is $f_p = 2.166 \times 10^{15}\text{s}^{-1}$, and the damping is $\gamma = 2.02 \times 10^{13}\text{s}^{-1}$. Al_2O_3 is assumed to have a constant permittivity $\epsilon_d = 3.61$ within the spectral region of interest. Figure 3-5(a) shows the dispersion curves for a $N = 5$ period metamaterial, while in Fig. 3-5(b) are the profile of the in-plane component of electric field (real part) for the six eigen modes. Note that the first two modes, labeled as "1" and "2" are the "surface" (in the sense of the surface of whole metamaterial as first introduced in [88]) SPP modes peak at the interfaces between the metamaterial and surrounding dielectric, extending significantly into the latter. Since the absolute values of $\boldsymbol{f}_k^n(z_0)^* \cdot \boldsymbol{f}_k^n(z_i)$ for these modes are larger, these two modes are expected to have larger contribution to the OTF. However, from Fig.
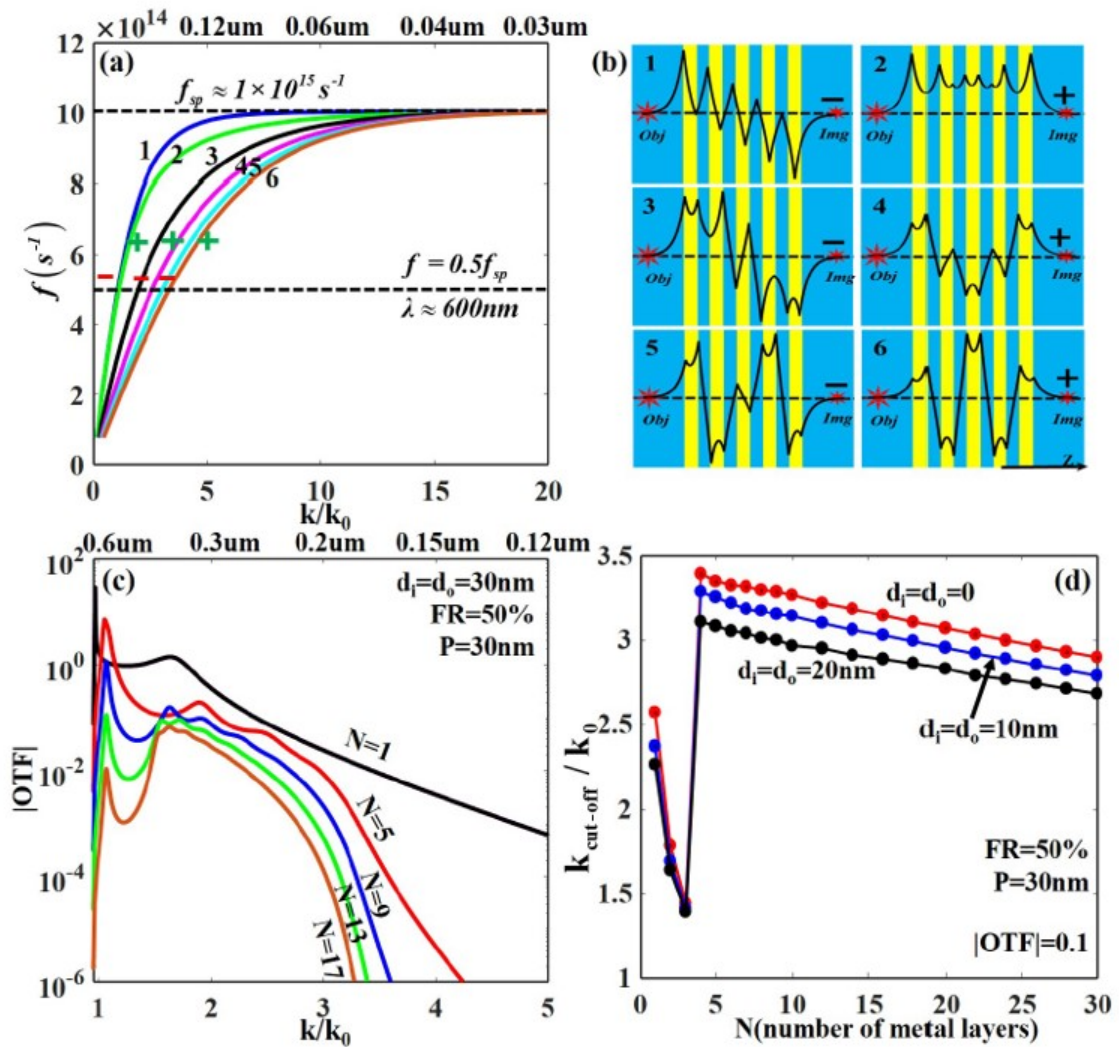
Figure 3-5. (a) The dispersion curves of the eigen modes when the superlens contains five metal slabs; (b) The profile of electric in-plane component of each eigen modes inside the superlens; (c) The absolute value of OTF when N=1, 5, 9, 13, 17, respectively; (d) The cut-off lateral wavevectors versus the number of metal layers for three different object and image distances.

3-5(b) we can also see that one of them is symmetric and the other is antisymmetric, which means that their contributions to the OTF have opposite signs. As the number of layers increases, the dispersion curves of the two eigen modes get closer and become degenerate which according to [88] the other modes ("3"-"6") are the "bulk" (in the sense of being inside the whole metamaterial) plasmon polariton (BPP) modes, and compared to the first two modes, they have stronger field confinement, which means that the BPP modes have smaller contribution to the process of imaging. Actually, half of the $N+1$ eigen modes are symmetric and the other half are antisymmetric, so due to the opposite symmetry, their contribution to the OTF tends to cancel each other. The only factor preventing complete cancellation is the difference of resonant frequencies, so as N increases, the resonant frequencies get closer and the cancellation between symmetric and antisymmetric eigen modes gets progressively stronger, especially at the large wavevector k, and resolution is expected to decrease. The absolute value of the OTF for the imaging using the multi-layer structure (calculated using TMM) is shown in Fig. 3-5(c) at the wavelength $\lambda \approx 600$nm (which corresponds to half of surface plasmon frequency) for N increasing from 1 to 17. The OTF goes through some peaks and valleys for small spatial frequencies due to resonances with eigen-modes and then decays steadily. The key feature of Fig. 3-5(c) is the fact that as N increases, the OTF curves not only shift downward (this is simply the result of absorption by larger number of layers) but also experience progressive rapid fall-off at large spatial frequencies, shifting leftward. This a the clear manifestation of the increased cancellation in the structures with large N.

This cancellation effect can be further gauged by first normalizing the OTF curve to its value at the second (broadest) peak and introducing the *cut-off spatial frequency* $k_{cut-off}$ such that $|OTF(k_{cut-off})| = 0.1$, which can be construed as an admittedly arbitrary yet reasonably appropriate resolution limit. The plot of $k_{cut-off}$ as a function of N is shown in Fig. 3-5(d) for different values of object and image distances. After a

sharp jump for N = 3 associated with the "merging" of the dispersion curves of the first two modes (and hence their nearly complete cancellation), the resolution of the "lens" experiences a steady decrease with an increasing number of metal layers. This is an important result, relevant for any multi-layered imaging contraption, including the hyperlens as the number of layers increases not only does the overall amount of light getting to the image is reduce (this can be mitigated in principle using optical amplifiers and/or more sensitive low noise detectors), but the resolution of the scheme also decreases which cannot be undone by any amplification or post-processing.
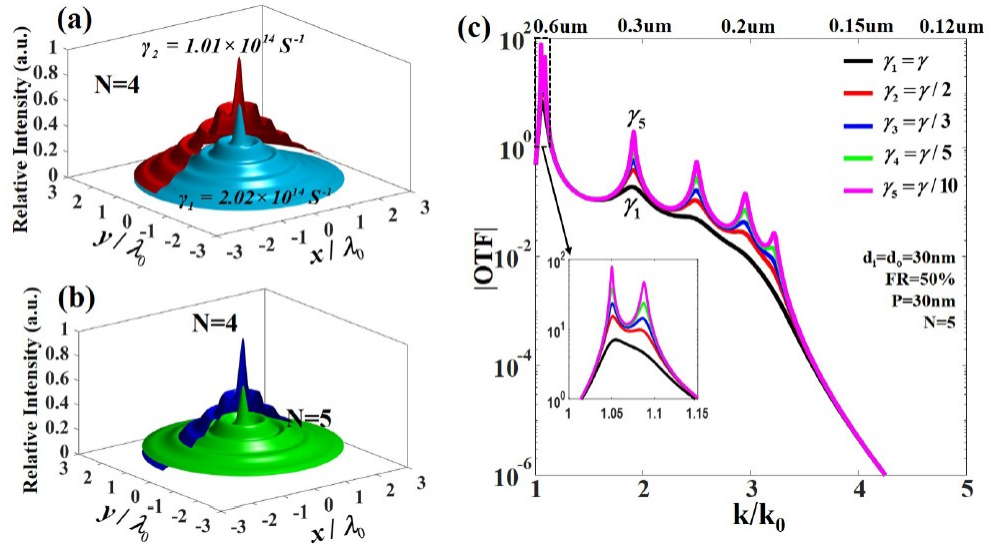
Figure 3-6. (a) Comparison of PSF with different metal loss when the superlens contains four metal slabs; (b) Comparison of PSF when the superlens contain four and five metal slabs respectively; (c) Change of OTF with different metal loss, when $N = 5, FR = 50\%$, $P = 30nm, di = do = 30nm$. λ_0 is the wavelength of signal.

In addition to the OTF, I also calculated the point spread function (PSF) to estimate the specific resolution of the multi-layer superlens. As shown in Fig. 3-6(a), an increase in the loss from $\gamma_2 = 1.01 \times 10^{14} s^{-1}$ to $\gamma_1 = 2.02 \times 10^{14} s^{-1}$ causes not only a decrease in the height of the PSF but also its spread, i.e. the resolution of the "lens". This effect is similar to the changes in the PSF with the number of layers as shown in Fig. 3-6(b). Figure 3-6(c) demonstrates the impact of the loss in metal on the OTF-at

small (admittedly unrealistic) values of loss, the OTF shows multiple peaks associated with excitation of the individual SPP modes, but as the loss increases to realistic values the peaks disappear and the whole OTF gets reduced by different values of metal loss.

3.4.2   The Cancellation effect
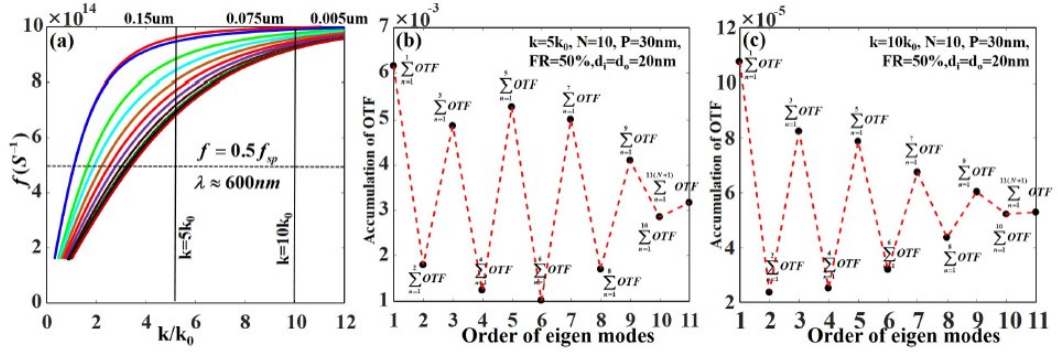
Figure 3-7. (a) Dispersion relations of the eigen modes when N=10; (b, c) The "OTF oscillations" as a function of the number of layers in the sum Eq. 3.9 for two values of special frequencies k = 5k$_0$ and k = 10k$_0$.

Before proceeding further, I want to present an illustration of how an increase in the number of layers suppresses the OTF at large spatial frequencies, thus reducing resolution, and the different contributions of modes to image. In Figs. 3-7(b) and 3-7(c) I show the evolution of the OTF for the N = 10 layered structure at two different values of k as keep adding the individual terms in Eq. 3.9. As one can see, the sum shows large swings with addition of each SPP mode since each two adjacent modes have different parities, until the sum converges. Moreover, from Figs. 3-7(b) and 3-7(c), we can see that the contribution of each eigen mode to the OTF are different; higher order modes have smaller contributions because of their stronger field confinement. Hence, the total OTF will not converge to zero, even though it contains a large number of metal/dielectric layers, the real main limit of OTF or resolution is metal loss.

One can also see how the cancellation gets stronger with increasing spatial frequency k from the dispersion curves shown in Fig. 3-7(a). As spatial frequency increases, the dispersion curves practically merge and the resonant denominators in the coupling coefficients in Eq. 3.7 become equal, ensuring more complete cancellation. Indeed, the oscillations in Fig. 3-7(c) converge much faster and to a lower steady value. It is important to note that this steady value is low yet not zero because cancellation is never complete when one of the modes is in resonance, or, when the frequency is between the eigen frequencies of two adjacent modes of different parities. Indeed, according to Eq. 3.9, these two modes get added with opposite signs which means that the fields in the image space will actually add up.

3.4.3 Impact of Granularity

Besides the number of layers and metal loss, the performance of the multi-layer lens gets affected by the geometrical parameters, such as the size of one metal/dielectric period and its composition, i.e. the fill ratio of metal ($FR = t_m/(t_m+t_d)$). The effect of different periods for the FR=1/2 is shown in Fig. 3-8. The first three (a)-(c) panels in this figure display the dispersion relations of eigen modes when the period is increased from P = 10nm to 30nm and 50nm. Rather naturally, as the period is increased and the separation between the interfaces grows, the individual surface plasmon polaritons becomes less and less coupled to each other and the eigen modes dispersion curves become denser, with the first two dispersion curves merging. As explained in the section 3.2 above, the cancellation gets stronger and the OTF gets drastically reduced with increase of the period as evidenced from Fig. 3-8(d). The impact on the resolution is even more pronounced as seen from Fig. 3-8(e) where cut-off spatial frequency $k_{cut-off}$ is displayed. Reducing granularity clearly benefits imaging but using metal structures in the visible range reducing the period beyond $\lambda/10$ is difficult. Better results may be attained with the semiconductor based multi-layers operating in the
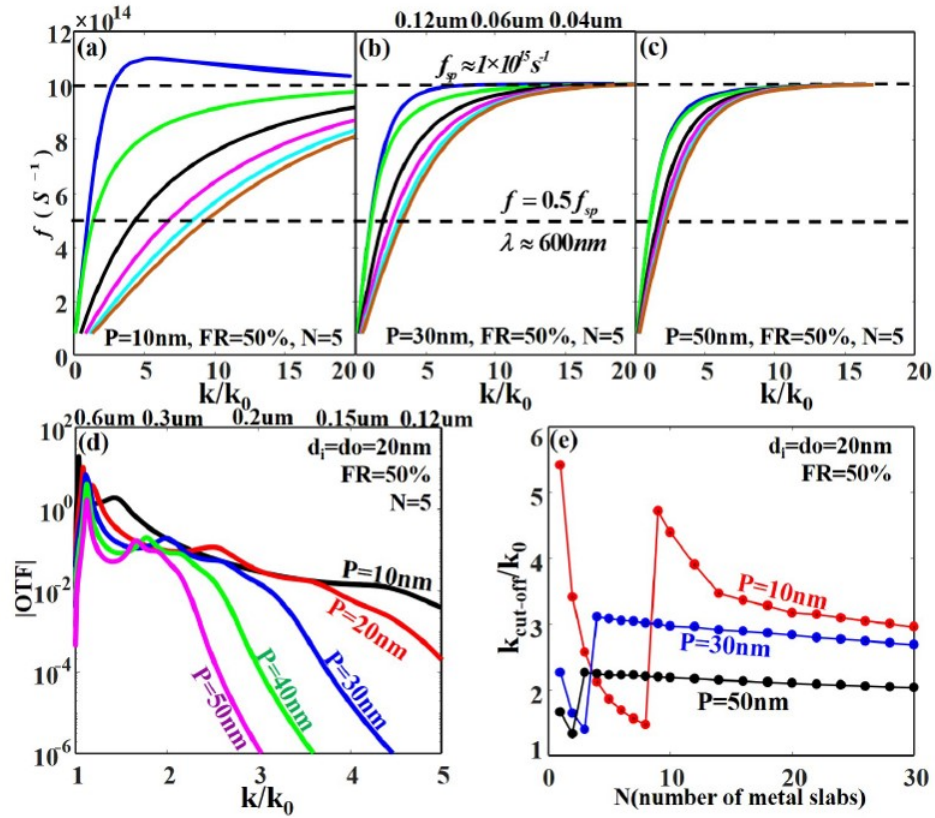
Figure 3-8. (a)-(c) The dispersion relations of eigen modes when the period $P = 10\text{nm}, 30\text{nm}, 50\text{nm}$ respectively; (d) Change of the OTF with increase in period when the metal fill ratio is set at 50%; (e) Change of the cut-off wavevector with different period when the fill ratio is set at 50%.

mid-IR region, although the loss in them can be quite large.

3.4.4   Impact of Metal Fill Ratio
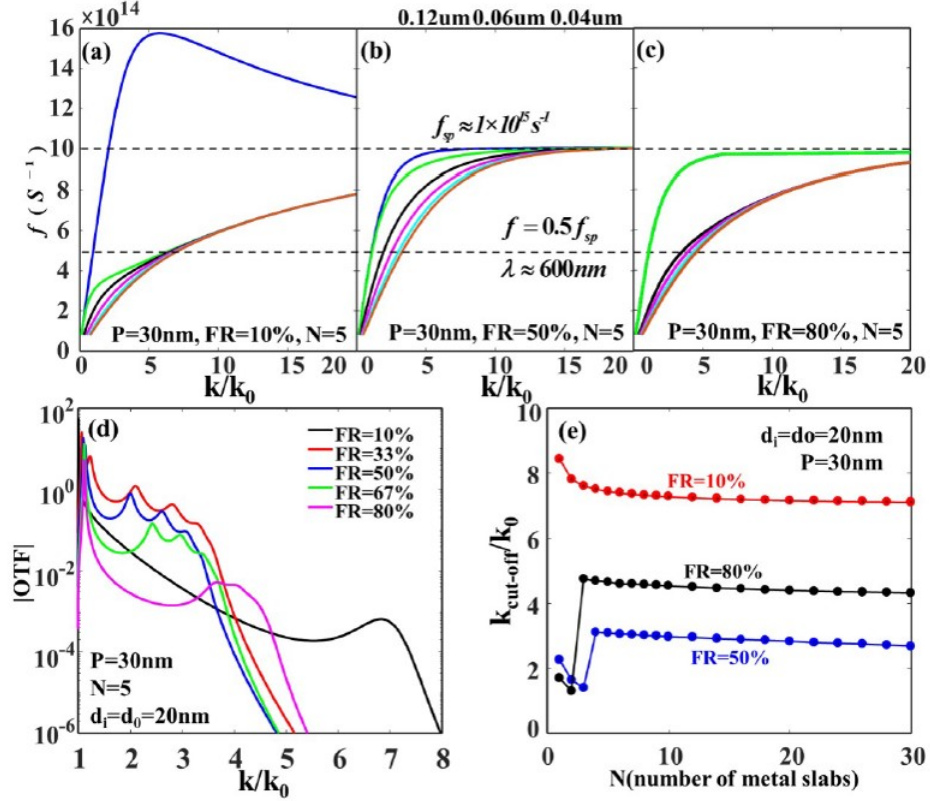
Figure 3-9. (a)-(c) are the dispersion relation of eigen modes with metal fill ratio $10\%, 50\%, 80\%$ respectively; (d) The absolute value of OTF for different metal fill ratios; (e) The cut-off wavevector for different fill ratios.

The fill ratio can also play an important role in determining the "lens" performance. I have calculated the OTF for different metal fill ratios ranging from 10% to 80% for the fixed period P = 30nm, and N = 5. Figs. 3-9(a)-(c) display dispersion curves for the filling ratio of 10%, 50% and 80% respectively. One can see that the curves for small fill ratio of 10% (Fig. 3-9(a)) are those of coupled slab SPPs with the first mode being a "long range SPPs" and the rest are closely spaced short range SPPs. In the opposite extreme of 80% fill ratio (Fig. 3-9(c)), the closely spaced dispersion curves correspond to weakly coupled "gap SPPs". For 50% fill ratio (Fig. 3-9(b)),

66

the distribution of dispersion is more uniform. From Fig. 3-9(d), we can see that even though 10% fill ratio has smaller metal loss, due to the denser dispersion curves and larger resonance spatial frequency, the OTF is still smaller than other fill ratios. For 80% fill ratio, due to both larger metal loss and denser dispersion curves, the OTF is much smaller. Fig. 3-9(e) shows the change of cut-off spatial wavevector with the number of period for different metal fill ratios. Due to larger resonance spatial frequency, after I normalized the OTF to its second peak to obtain the cut-off wavevector, extra small and large fill ratios have a large cut-off spatial frequency; practically however, from Fig. 3-9(d), we can tell that a large OTF (better resolution) can be obtained with a metal fill ratio around 33%.

3.4.5 multi-layered imaging at the extreme
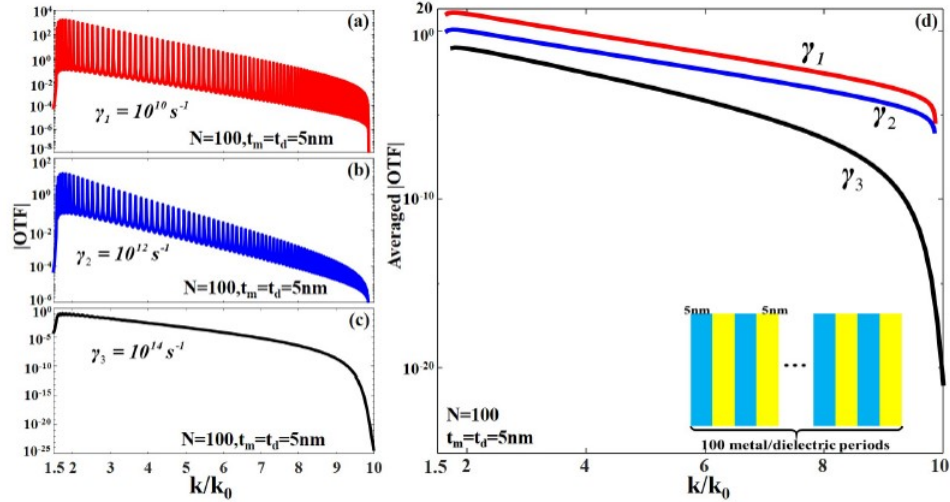
Figure 3-10. (a)-(c) The OTF of hyperlens contains 100 metal/dielectric period for different metal loss when the thickness of meta and dielectric are $t_m = t_d = 5$nm; (d) The averaged OTF of hyperlens contains 100 metal/dielectric period for different metal loss when the thickness of meta and dielectric are $t_m = t_d = 5$nm.

Next, I explore the limitation of imaging with multi-layered structures that contains large number of metal layers with different granularity. As the number of metal/dielectric periods increases and granularity decreases the multi-layered structure approaches

67

the limit in which it can be characterized by effective permittivity and continuous hyperbolic (or elliptical) dispersion. In other words, the eigen functions f becomes the Bloch [89] functions. However, the Bloch function method does not describe the previously mentioned "surface modes" well and these modes play an important role in imaging with hyperlens.

Even though these structures would be impractical from the fabrication point of view at the present time, it is worthwhile to consider what limits they can reach in the future. Also, while as far as we know it is next to impossible to reduce substantially the ohmic losses in metals, let alone completely cancel them, it is also interesting to consider what happens when the number of layers increases and the loss becomes very small. When N becomes large, while the loss gets small, let us say $N > 50$, the OTF under monochromatic illumination will contain a number of sharp resonant peaks; in the practical situation when the light is not strictly monochromatic these peaks will be averaged out and it is these averaged OTF that presents practical interest. In Figs. 3-10(a)-(c), I show an example of the OTF for $N = 100$ and three different values of loss ($\gamma = 10^{10}\text{s}^{-1}, 10^{12}\text{s}^{-1}$, and 10^{14}s^{-1}) which shows rapid oscillation as loss decreases to admittedly unrealistic values. Next to it in Fig. 3-10(d) I show the "incoherent OTF" obtained as $\overline{\text{OTF}_n} = \left[\int_{k_{n-l}}^{k_{n-r}} \mid \text{OTF(k)}_n \mid^2 \text{dk}/(k_{n-r} - k_{n-l}) \right]^{1/2}$, where k_{n-l} and k_{n-r} are the valley wavevectors on the left and right side of the $n - \text{th}$ OTF peak. The "smoothed" OTF of Figs. 3-10(a)-(c) shows that reduction of loss increases the OTF and the cut-off wavevector but with diminishing returns. Two orders of magnitude reduction of loss from 10^{14}s^{-1} to 10^{12}s^{-1} bring 12-fold improvement in the OTF but the further reduction to 10^{10}s^{-1} (highly unrealistic) value only yields a 10-fold. In other words, cancellation is still at work at low loss. To compare the effects of granularity and the number of layers, I now plot the averaged OTF for $N = 50$ and $N = 100$ with two different granularities in Fig. 3-11 for three aforementioned values of loss.
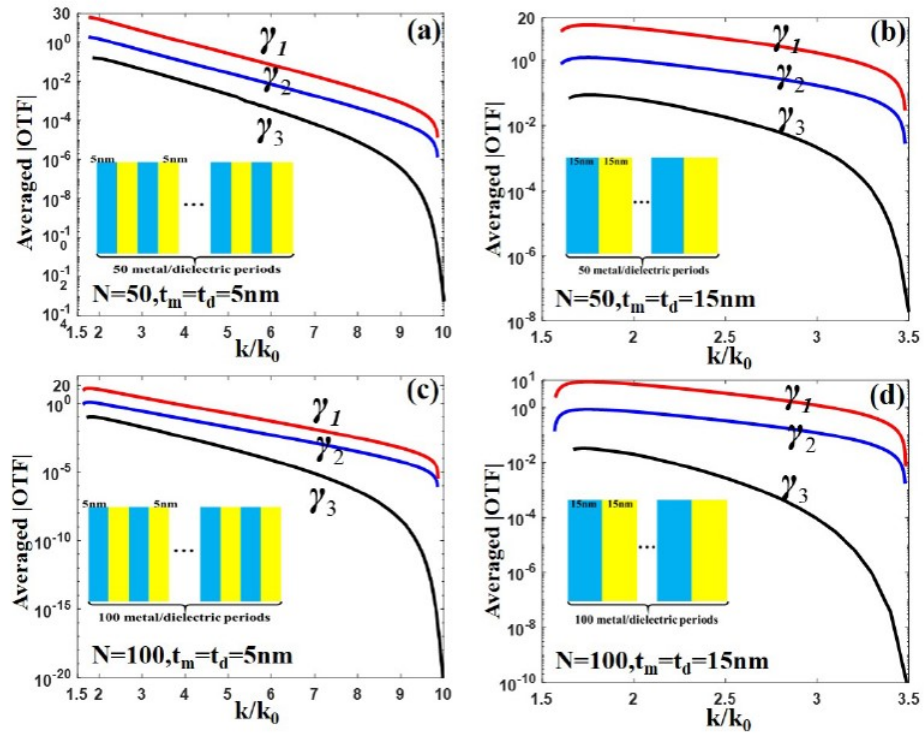
Figure 3-11. (a) and (b) The averaged OTF of hyperlens contains 50 metal/dielectric periods for different metal loss when the thickness of meta and dielectric are $t_m = t_d = 5nm$ and $t_m = t_d = 15nm$ respectively; (c) and (d) The averaged OTF of hyperlens contains 100 metal/dielectric periods for different metal loss when the thickness of meta and dielectric are $t_m = t_d = 5nm$ and $t_m = t_d = 15nm$ respectively.

Comparing Figs. 3-10(a) with 3-10(c) and Figs. 3-10(b) with 3-10(d) reveals that an increase in the number layers from 50 to 100 still causes the OTF deterioration and fall in $k_{cut-off}$-result of the cancellation, but the reduction is small as discussed in the end of section 3.2. A comparison of Figs. 3-10(a) with 3-10(b) and Figs. 3-10(c) with 3-10(d) shows the improvement achieved with lower granularity as expected from the effective hyperbolic medium, yet the benefit from lower granularity is quite insignificant for the large number of layers. It is possible that these advantages can be put into productive use with all-semiconductor structures in mid-IR range.

3.5   Conclusions

In this work, we investigated performance of the multilayer metal/dielectric near field imaging structures. We have demonstrated that the imaging process of these multilayer structure can be best understood as coupling of object signal into the SPP eigenmodes supported by the structure and subsequent formation of the image on the other side. Due to the ensuing strong cancellation of the contributions of symmetric and antisymmetric eigen modes, the resolution decreases with more metal layers thus limiting the number of layers to less than 20 and the object to image distance to only a fraction of a micrometer-much less than what can be expected from the simple metal loss considerations. We have also investigated and explained the impact of metal loss, granularity, and fill ratio on the near field imaging performance of the multilayer structure. Our main conclusion, which is also relevant to the cylindrical hyperlenses is that multilayer metal dielectric structures do not offer a performance superior to the single layer superlenses, but may find limited range of niche applications where one needs to have object to image distance increased beyond tens of nanometers. These results will hopefully be useful to the researchers active in the area.

Chapter 4

Sub-wavelength field enhancement in the mid-IR: photonics versus plasmonics versus phononics

4.1   Introduction

In the past two decays, due to the emergence and fast development of the discipline of plasmoncis, metamaterials and metasurfaces,numerous novel optical phenomena that cannot be realized using natural materials have been achieved, this also directly results in the explosive growth of nanophotonics. One of the most important and interesting features is that the electric field can be confined on a subwavelength scale, then strong electric field enhancement can be obtained, and mamy applications have been developed.

To achieve strong field enhancement, people have developed and tried many structures and methods. One of the most common is via the propagating and localized surface plasmon polaritons (SPPs), which can generate high field enhancement by confine the field at the surface, because the excited plasmon modes dissipate very fast along the surface normal and in the propagation direction. Based on this mechanisms, people have successfully achieve the strong field enhancement and developed applications such as optical sensing [90, 91], imaging [14], photovoltaics

[92] , nonlinear optics [93], optical micromanipulation and a plethora of other diverse fields. So far, the cause of this disappointing state of affairs is the aforementioned ohmic loss in the metals [78] which limits both the magnitude of the field enhancement and its spectral selectivity in accordance with the SPP quality factor $Q = \omega/\gamma_{\mathrm{m}}$, where $\gamma_{\mathrm{m}} \sim 10^{14}\mathrm{s}^{-1}$ is the intrinsic (material) energy damping rate in a typical noble metal [71]. In the visible and near-infrared (IR) ranges, it is unlikely to find a low-loss alternative to metals, since alternative materials such as TiN [94], ITO [95, 96], AlZnO [97], and others have damping rate orders of magnitude higher than those of noble metals, while their plasma frequencies are lower. High scattering rates are associated with either the d-shell character of states near the Fermi level, as is the case in TiN, or with the lack of stoichiometry. Therefore, while these materials may present an alternative to metals in terms of availability, complementary metal–oxide–semiconductor (CMOS) compatibility, or higher melting point, they are not likely to offer field concentration performance comparable to metals. However, for longer wavelengths, especially in the all-important mid-IR region ($3˘20\mu$m), a number of what appear to be viable low-loss alternatives to metals have recently emerged. These alternatives include surface phonon polaritons (SPhPs) in the Reststrahlen region of polar dielectrics [98], heavily doped high-mobility semiconductors [99] and, last but not least, high-index all-dielectric structures operating just outside the Reststrahlen region [100]. The intrinsic, or material momentum loss rates, γ, in all these materials, are substantially (an order of magnitude or more) lower than in the noble metals and, therefore, it is quite reasonable to posit that large and more frequency selective field enhancements can be achieved with the new material systems. However, the intrinsic loss rate is not the only relevant characteristic that determines the field enhancement. Just as important is the way the energy is distributed between the energy of the fields and the energy of the matter, as shown in Refs. [101–103]. In Ref. [101, 102], we have shown first analytically, and then numerically that, due

to a larger concentration of free electrons in metal structures, a smaller fraction of energy needs to be stored in the form of kinetic motion of these carriers, and most of the energy stays in the form of a magnetic field. As a result, the effective loss of metallic structures can be lower than in the semiconductor ones, despite higher intrinsic loss. However, to achieve SPP resonance in the mid-IR, metal nanoparticles must have large aspect ratios that are hard to fabricate, as was pointed out in Refs. [104, 105]. We have also shown in Ref. [101] that in phononic structures, a significant (if not dominant) share of potential energy resides in the form of ion displacements, which means that the electric field enhancement is far more modest than the energy density enhancement. What has been absent from the accumulated work is the direct comparison of different material systems for field enhancement in the mid-IR region, which would give an unambiguous answer to the question of what would be the best practical structure causing the strongest enhancement of electric field in the sub-wavelength mode (relative to wavelength in vacuum). (Note that the physical dimensions of the structure may be comparable or even larger than that wavelength.) In this Letter, we perform such a comparative analysis for different material/shape systems capable of providing resonant field enhancement in the wavelength region $10\check{\ }15\mu$m [all shown in Figs. 4-2(a)–(e)] and arrive at a set of clear conclusions that will hopefully assist researchers in designing field enhancement schemes to suit their needs.

$$\varepsilon_r\left(\omega\right)=\varepsilon_\infty\left(1+\frac{\omega_p^2}{\omega_{TO}^2-\omega^2-j\omega\gamma}\right) \tag{4.1}$$

$$\varepsilon_{met}\left(\omega\right)=\varepsilon_\infty\left(1-\frac{\omega_p^2}{\omega^2+j\omega\gamma_f}\right) \tag{4.2}$$

In this work, I compared several field enhancement mechanisms in the mid-IR region via theoretical analysis and simulation.

4.2 Energy Balance of Light Matter Interaction

In this section, let's dive into the energy balance analysis in polar dielectric structures first. Suppose a mode contained within some volume of dielectric with permittivity $\epsilon_r(\omega)$, and suppose the characteristic dimension of the volume is a, then the electric field can be written as roughly $E \sin(\pi x/a) \sin(\omega t)$ and the magnetic field as $H \cos(\pi x/a) \cos(\omega t)$. By using the Maxwell equations one can get the relation between the magnitudes of the above fields,

$$H \approx \frac{\omega a}{\pi} \varepsilon_0 \varepsilon_r E = \frac{2a}{\lambda} \frac{\varepsilon_r E}{\eta_0}. \tag{4.3}$$

The time-averaged electric energy density can be written as,

$$\langle U_E \rangle = \frac{1}{4} \varepsilon_0 \frac{\partial (\omega \varepsilon'_r)}{\partial \omega} E^2 \tag{4.4}$$

where ϵ'_r is the real part of dielectric constant and the time-averaged magnetic energy density is,

$$\langle U_M \rangle = \frac{1}{4} \mu_0 |H|^2 \sim \left(\frac{2na}{\lambda}\right) \frac{1}{4} \varepsilon_0 \varepsilon'_r E^2, \tag{4.5}$$

and $n = \mathrm{Re}(\sqrt{\epsilon_r})$. Here I consider only the lowest order mode in the cavity, then $a = \lambda/2n$, by neglecting the dispersion one can obtain the energy conservation relation $\int \langle U_E \rangle d^3 r = \int \langle U_M \rangle d^3 r$.

However the time averaged picture does not properly represent the energy balance in the mode since the electric energy includes contributions oscillating 90 degrees out of phase with each other (in-phase and quadrature components). From Lorentz oscillator model, the relative dispacement of ions is,

$$x(t) = \frac{e^*/M_r}{\left[(\omega_{TO}^2 - \omega^2)^2 + \omega^2 \gamma^2\right]^{1/2}} E \sin(\omega t - \varphi) \tag{4.6}$$

where $\tan(\phi) = \gamma^2 \omega^2 / (\omega_{TO}^2 - \omega^2)^2$, and the velocity of this motion is

$$\dot{x}(t) = -\omega \frac{e^*/M}{\left[(\omega_{TO}^2 - \omega^2)^2 + \omega^2 \gamma^2\right]^{1/2}} E \cos(\omega t - \varphi). \tag{4.7}$$

74

Then one can get the expressions for the kinetic energy and potential energy densities inside the volume,

$$U_K(t) = \frac{1}{2}NM_r\dot{x}^2(t) = \frac{1}{2}\frac{\omega^2\omega_p^2}{\left(\omega_{TO}^2 - \omega^2\right)^2 + \omega^2\gamma^2}\varepsilon_0\varepsilon_\infty E^2\cos^2(\omega t - \varphi) \qquad (4.8)$$

$$U_P(t) = \frac{1}{2}NM_r\omega_{TO}^2 x^2(t) = \frac{1}{2}\frac{\omega_{TO}^2\omega_p^2}{\left(\omega_{TO}^2 - \omega^2\right)^2 + \omega^2\gamma^2}\varepsilon_0\varepsilon_\infty E^2\sin^2(\omega t - \varphi) \qquad (4.9)$$

And the potential energy density can be split into two parts,

$$U_P(t) = \frac{1}{2}\frac{\omega_p^2\left(\omega_{TO}^2 - \omega^2 + \omega^2\right)}{\left(\omega_{TO}^2 - \omega^2\right)^2 + \omega^2\gamma^2}\varepsilon_0\varepsilon_\infty\sin^2(\omega t - \varphi) = U_{P1}(t) + U_{P2}(t), \qquad (4.10)$$

the first part is

$$U_{P1}(t) = \frac{1}{2}\frac{\omega_p^2\left(\omega_{TO}^2 - \omega^2\right)}{\left(\omega_{TO}^2 - \omega^2\right)^2 + \omega^2\gamma^2}\varepsilon_0\varepsilon_\infty E^2\sin^2(\omega t - \varphi) = \frac{1}{2}\varepsilon_0\left(\varepsilon'_r - \varepsilon_\infty\right)E^2\sin^2(\omega t - \varphi)$$
$$(4.11)$$

where ϵ'_r is the real part of the dielectric constant, the second part is

$$U_{P2}(t) = \frac{1}{2}\frac{\omega^2\omega_p^2}{\left(\omega_{TO}^2 - \omega^2\right)^2 + \omega^2\gamma^2}\varepsilon_0\varepsilon_\infty E^2\sin^2(\omega t - \varphi) = \frac{1}{4}\varepsilon_0\omega\frac{\partial\varepsilon'_r}{\partial\omega}E^2\sin^2(\omega t - \varphi), \qquad (4.12)$$

it has the same amplitude as the kinetic energy density, but its phase it shifted by 90 degrees. Then the total electric energy density can then be found as

$$U_E(t) = U_{P1}(t) + U_{P2}(t) + U_\infty(t) + U_K(t) = \frac{1}{2}\varepsilon_0\varepsilon'_r E^2\sin^2(\omega t - \varphi) + \frac{1}{4}\varepsilon_0\omega\frac{\partial\varepsilon'_r}{\partial\omega}E^2$$
$$(4.13)$$

where

$$U_\infty(t) = \frac{1}{2}\varepsilon_0\varepsilon_\infty E^2\sin^2(\omega t) \approx \frac{1}{2}\varepsilon_0\varepsilon_\infty E^2\sin^2(\omega t - \varphi) \qquad (4.14)$$

is the sum of energy stored in the electric field proper $U_{EF} = \frac{1}{2}\epsilon_0 E^2$, and the potential energy associated with oscillations of valence electrons $U_V = \frac{1}{2}\epsilon_0(\epsilon_\infty - 1)E^2$. Then bt neglecting a small phase shift ϕ in Eq. 4.14 amounts to a very small error on the scale of γ^2/ω_p^2. By averaging Eq. 4.13 over time immediately leads to Eq. 4.4.

Now we can see that the energy oscillating roughly in phase with the electric field, which can be referred to as either "in phase" or "potential" is

$$U_I(t) = U_\infty(t) + U_{P1}(t) + U_{P2}(t) \tag{4.15}$$

and has three components. The first one $U_\infty(t)$ is entirely static electric field energy because it is frequency independent. The second one $U_{p1}(t)$ is only weak resonant and dominates the frequency response in the normal dispersion region. The third component $U_{P2}(t)$, whose amplitude is equal to the amplitude of kinetic energy $U_K(t)$, is very dispersive and becomes the dominant factor in the anomalous dispersion region.

In the Anomalous region, when $\omega > \omega_{TO}$, U_{p1} becomes negative but the total potential energy Eq. 4.10 is of courst always positive. The energy taht oscillates roughly 90 degrees out of phase with the electric field, and can be referred to as either "quadrature" or kinetic in the Lagrangian mechanics sense

$$U_Q(t) = U_K(t) + U_M(t), \tag{4.16}$$

and it has two components, the actual kinetic energy of the ions $U_K(t)$, which is strongly dispersive, and the magnetic energy $U_M(t)$. Whether kinetic of magnetic energy dominates depends on the dimensions of the mode. Comparing Eq. 4.8 with Eq. 4.5 immediately yields

$$\frac{U_K}{U_M} \sim \left(\frac{\lambda}{2a}\right)^2 \frac{\omega}{a|\varepsilon'_r|^2} \frac{\partial \varepsilon'_r}{\partial \omega} \sim \frac{1}{2}\left(\frac{\lambda}{2a}\right)^2 \left(\frac{\omega^2}{\varepsilon_\infty \omega_p^2}\right) \sim \frac{1}{2}\left(\frac{\lambda_p}{2an_\infty}\right)^2 \tag{4.17}$$

$$\gamma_{eff} = \gamma\frac{U_K}{U_M + U_K} \sim \left(\frac{\lambda_p}{2an_\infty}\right)^2 \Big/ \left[\left(\frac{\lambda_p}{2an_\infty}\right)^2 + 2\right] \tag{4.18}$$

Equation 4.18 is the effective loss obtained based on the energy balance analysis. It shows the main difference between the plasmonic and phononic subwavelength structures. The plasma wavelength of metals is in the range of 140–150 nm; hence, if metallic structures operate in the mid-IR range, the characteristic dimension may be

substantially smaller than the operating (resonant) wavelength λ_0 but still an order of magnitude larger than $\lambda_P/2an$ and the effective loss can be orders of magnitude smaller than the metal damping rate $\gamma \sim 10^{14}\text{s}^{-1}$. When one operates far from plasma frequency ($\lambda \gg \lambda_P$) and the kinetic energy of electrons is small, it is preferable not to invoke the term "plasmon" and instead use the terms "metal waveguides" or "metal nanoantennas." For phononic structures, on the other hand, the operational wavelength is always much shorter than the plasma wavelength, meaning that in the subwavelength phononic structure, the effective loss is always equal to the phonon damping rate (which is, as mentioned above, two orders of magnitude less than the electrons damping rate in the metal). Hence, even though the momentum damping rate is lower, it does not offer any significant advantage over the metallic structures.

4.3   Field Enhancement Comparison

I refer to the first field enhancement scheme as a "phononic" scheme, since field enhancement occurs via excitation of localized SPhPs, i.e., collective oscillations of ions in polar dielectrics coupled with the electric field. I consider the widely used example of silicone carbide (SiC), whose dielectric constant is described by

$$\epsilon_{SiC}\left(\omega\right) = \epsilon_{\infty,SiC}\left(1 + \frac{\omega_{LO}^2 - \omega_{TO}^2}{\omega_{TO}^2 - \omega^2 - j\omega\gamma_{ph}}\right) \tag{4.19}$$

where $\epsilon_{\infty,\text{SiC}} = 6.7$ is the high frequency dielectric constant, $\gamma_{\text{ph}} = 10^{12}\text{s}^{-1}$ is the damping rate, $\omega_{\text{TO}} = 2\pi \times 23.88\text{THz}$ and $\omega_{\text{LO}} = 2\pi \times 29.16\text{THz}$ [106, 107] are the transverse and longitudinal optical phonon frequencies respectively. This dispersion shown in Fig. 4-1(a) indicates that, in the Reststrahlen region between the TO and LO frequencies, the dielectric constant is negative; hence, it can support localized SPhP modes. The exact position of the resonance depends on the shape of the SiC and, for air-clad spherical SiC particles (Fig. 4-2(a)), the resonance occurs at $934\text{cm}^{-1}(10.7\mu\text{m})$ [108]. Since the damping rate of SiC is about two orders of magnitude smaller than

that of metal, the resonance spectrum of a SiC sphere is expected to be much sharper than others.

Alternatively, rather than operating in the Reststrahlen region, one can achieve field enhancement at a wavelength somewhat longer than that of a TO phonon, where the dielectric constant is large. As shown in Fig. 4-1(a), away from the Reststrahlen band and, at frequencies below TO, the real part of permittivity and therefore the refractive index of SiC can be positive and quite large, and the imaginary part is reasonably small. By using a high-index material spherical structure, the electromagnetic field can be enhanced through the different Mie *photonic* resonance modes inside the high-index sphere. Of all these photonic resonance modes, the magnetic dipole mode shown in Fig. 4-2(b) can generate the strongest field enhancement [109]. The relation between the wavelength of the magnetic dipole (MD) resonance and the size of the spherical particle of diameter D, is approximately given as $\lambda_{\mathrm{MD}} = nD$, [110, 111] where n is the refractive index. Note that, while many semiconductor and polar materials can be utilized to build a high-index structure, for convenience, I still use SiC. While the structure is not strictly sub-wavelength relative to λ/n, the region in which the field gets enhanced is substantially smaller than the wavelength in free space. This field enhancement scheme to which I refer as *all-dielectric Photonic*, has small non-radiative loss, and the radiative loss is quite high; hence, it is not clear at first glance how competitive this scheme is.

The third scheme studied here is the sphere made from a heavy doped semiconductor whose dispersion is,

$$\epsilon_{GaAs}\left(\omega\right) = \epsilon_{\infty,GaAs}\left(1 - \frac{\omega_{p,GaAs}^2}{\omega^2 + j\omega\gamma_s}\right) \tag{4.20}$$

and has been shown in Fig. 4-1(b), where, using the example of GaAs, $\epsilon_{\infty,\mathrm{GaAs}} = 12.9$, its damping rate is $\gamma_{\mathrm{s}} = 2 \times 10^{13}\mathrm{s}^{-1}$, and $\omega_{\mathrm{p,GaAs}}^2 = \mathrm{N_d^+}e^2/\epsilon_0\epsilon_\infty m^*$ is the bulk plasma frequency, the effective mass m^* is 0.067 times of electron mass and $\mathrm{N_d^+}$ is the doping

density. The sphere is capable of supporting the localized SPP for frequencies less than ω_{p} and when $\mathrm{N_d^+} = 7.97 \times 10^{17} \mathrm{cm^3}$ one can achieve the resonance at exactly the same wavenumber of $934\mathrm{cm^{-1}}$ as SPhP of Fig. 4-2(a). Since the operating frequency is close (factor of $1/\sqrt{3}$) to the plasma frequency, a significant part of energy is coupled into the collective motion of electrons (rather than magnetic field) and this structure can be referred to as operating in "*true Plasmonic*" regime that is expected to offer some degree of field enhancement.
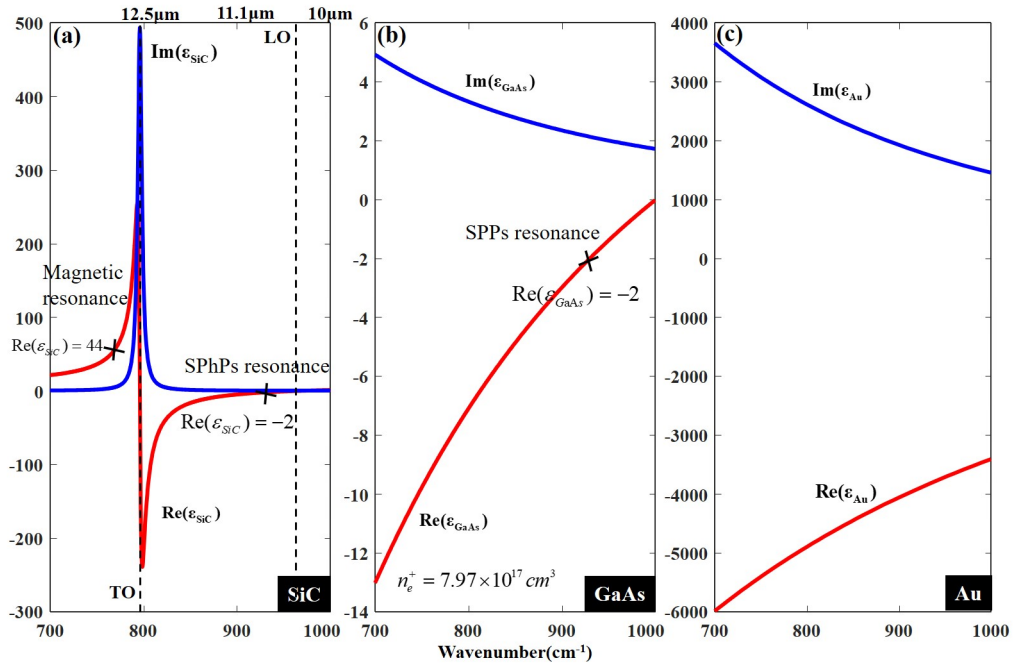
Figure 4-1. Permittivities of real and imaginary parts of the dielectric constant of (a) SiC, (b) n doped GaAs, and (c) gold in and around the Reststrahlen region of SiC.

Last, but not least I consider metal-insulator-metal (MIM) structure of Fig. 4-2(e) also known as the nano-patch antenna [107]. This structure is easier to fabricate than the prolong ellipsoids considered in [102], and, although with sizes approaching $\lambda/2$ they cannot be qualified as "sub-wavelength", the field enhancement region in them is clearly sub-wavelength. I shall refer to MIM and other antenna-like structures incorporating metals as "*metal photonic*" rather than "*plasmonic*" because in the mid-IR region, operating far below the plasma frequency, the real part of the dielectric

constant of the noble metal, such as gold and copper, as shown in Fig. 4-1(c), can be very large in absolute value ($|\mathrm{Re}\,(\epsilon)| \sim (3000 - 5000)$) in the wavelength range $10 - 15\mu$m. The field then hardly penetrates the metal and the energy remains in the form of electric and magnetic fields with only a tiny fraction of it being coupled into the kinetic motion of carriers. As a result, despite the high damping rate of the kinetic energy, the overall effective damping rate is expected to remain low, causing the high field enhancement. To get a comprehensive and convincing comparison, I also consider the field enhancement of patch antennas built using polar material (SiC) and doped semiconductor (GaAs), as shown in Figs. 4-2(d) and (f). Just as I have pointed out above, with energy being channeled into lattice vibrations in polar dielectrics, and the large penetration depth in doped semiconductors, the field enhancement is expected to be less than that of MIM.
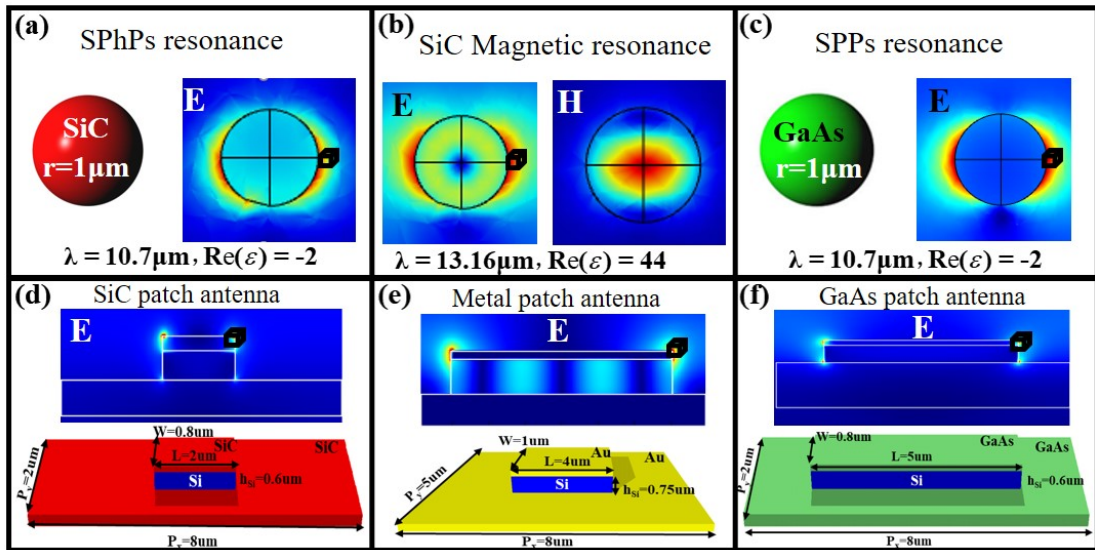
Figure 4-2. (a) Enhanced electric field profile when the SPhPs ("phononic") resonance occurs at the surface of a SiC sphere, whose radius is 1μm. (b) Electric and magnetic field profile when the magnetic "all-dielectric photonic" resonance occurs in the same sphere as (a). (c) Enhanced electric field profile when the SPP "plasmonic" resonance occurs at the surface of a doped semiconductor sphere whose radius is 1μm. (d)–(f) Electric field profiles of the SiC "phononic", Au "metal photonic", and GaAs "plasmonic" patch antennas. The $0.1\mu\mathrm{m}^3$ cube indicates a volume within which the mean field enhancement is calculated.
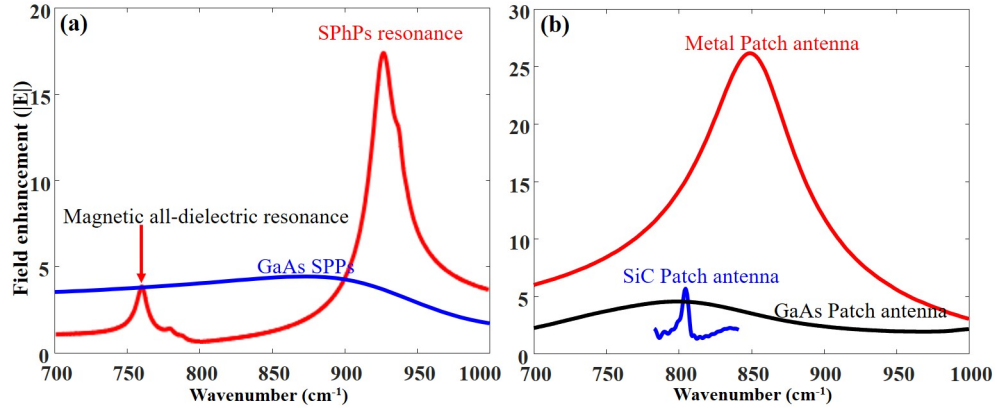
Figure 4-3. (a) Field enhancement spectra of phononic (SiC), all-dielectric photonic (SiC), and plasmonic (GaAs) resonances in spherical nanoparticles of Figs. 4-2(a)–(c). (b) Field enhancement spectra of metal photonic (Au), phononic (SiC), and plasmonic (doped GaAs) patch antennas of Figs. 4-2(d)–(f).

I have compared the field enhancing performances of the mid-IR structures introduced above with the help of a finite-different time-domain commercial program (Lumerical FDTD). In simulations of SiC and GaAs spheres, a single sphere whose radius is 1um was put in the air, light comes from the z direction, and in the x and y directions, perfect matched layers were set to absorb the scattered field and avoid reflection. For the simulation of a "*metal photonic*" MIM, SiC patch antenna, and GaAs patch antenna schemes, a unit cell was simulated by setting a periodic boundary condition in the x and y directions.

From the practical point of view, for many applications, particularly in sensing, the field enhancement region ("hot spot") should be sufficiently large so that it will not be problematic to actually introduce the molecules or clusters to be studied into these volumes. Therefore, to obtain a fair estimate of the enhancement, the calculated fields are always averaged over a $0.1\mu m^3$ cube around the "hot spot" where the maximum enhancement takes place as shown in Fig. 4-2.

The spectra of the mean field enhancement in all the aforementioned schemes are shown in Figs. 4-3(a) and (b). The peak enhancement magnitude and full width half maximum (FWHM) bandwidth are then summarized in Fig. 4-4. A few important
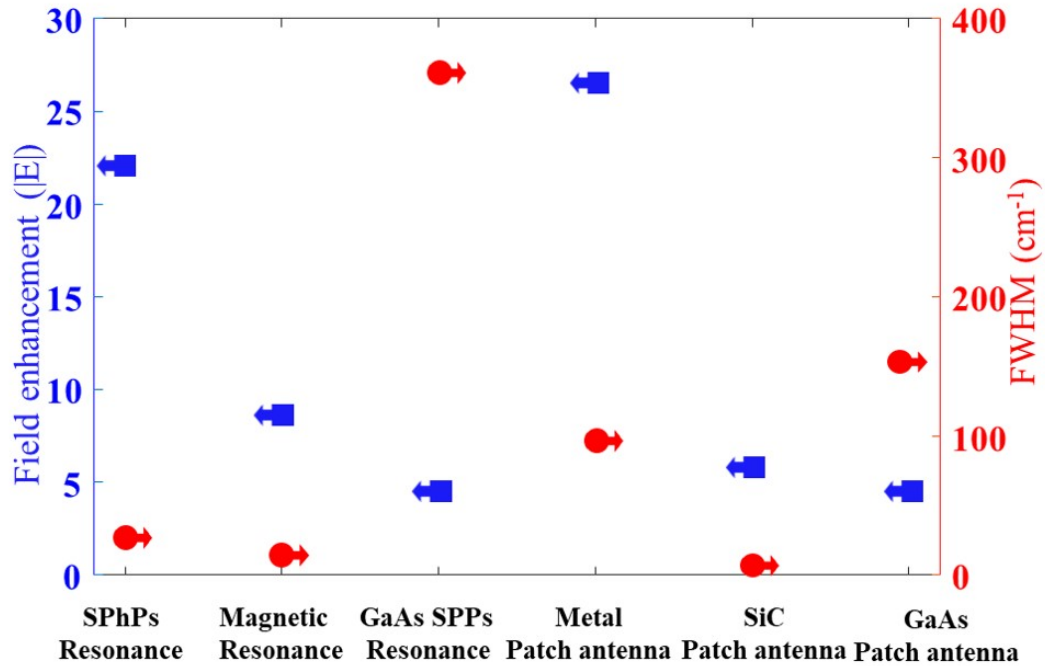
Figure 4-4. Comprehensive comparison of the field enhancements and bandwidths for all the mechanisms and structures considered in this Letter.

trends can be observed.

First, of all the schemes it is the SiC *Phononic* structure (Fig. 4-3(a)) that shows the sharpest resonance around 930cm^{-1} which is entirely expected based on by far the lowest intrinsic loss rate in SiC. The narrow bandwidth of phononic enhancement makes it undeniably the best for applications requiring high frequency selectivity, meaning sensing based on specific changes in either refractive or absorptive properties of analytes. But the range in which this sharp resonance can exist is limited, practically speaking, to about one half of the Reststrahlen band. At the same time, the degree of field enhancement by SPhPs is not as high as would be expected based on their low damping rate. That's because when the phonon material interacts with an electromagnetic field, the oscillating ions carry not only kinetic energy but also [102, 103]. Actually, in the Reststrahlen region, the magnitudes of these two kinds of energy are comparable; hence in SPhP the energy transfers back and forth between the kinetic and potential energy, with just a small fraction of energy contained inside the electric

82

field. For a dispersive material in the near absence of the magnetic field, the energy density is $\mu = \left[\partial \left(\omega \epsilon \right) / \partial \omega \right] |E|^2/4$, and the value of $\partial \left(\omega \epsilon \right) / \partial \omega \sim 88$ which means that most of the energy resides in the form of potential energy of the oscillating ions. Hence, field enhancement of phononic material cannot be as dramatic as metal.

Next, I turn our attention to the performance of the *all-dielectric photonic* structure near the magnetic resonance of a SiC sphere, also shown in Fig. 4-3(a). As I have mentioned before, just below the TO phonon frequency, the SiC dielectric constant can be quite large; hence the small (in comparison to the free space wavelength) all-dielectric structure can be resonant. In our example magnetic resonance takes place near 760cm^{-1}, where the refractive index is n $\approx$ 6.63, and the electric field enhancement outside SiC is much smaller than that of the Phononic SiC structure, while the bandwidth is just as narrow as within the phononic structure. The performance of the all-dielectric photonic scheme is limited by the large radiation loss and the fact that most energy still goes into ion vibrations $\partial \left(\omega \epsilon \right) / \partial \omega \sim 245$. A more detailed study of the field enhancement ability of all-dielectric structures has been conducted [109], and it also identified the high radiation efficiency of the magnetic mode as the main culprit behind the low field enhancement. Note that the magnetic dipole resonance frequency and the field enhancement vary with the size of the SiC sphere, but our simulation results show that the electric field enhancement is always smaller than that of the SPhPs.

The heavily-doped GaAs sphere *plasmonic* structure performance is also shown in Fig. 4-3(a). It clearly belongs to the opposite end of the performance spectrum: the enhancement is much lower in magnitude and wider when compared to the Phononic structure. This has to do with the significantly stronger damping rate in doped GaAs, and, given that one operates close to the plasma frequency, the field permeates the nanoparticles and the effective damping rate is commensurate with the intrinsic rate. At the same time, unlike ions, free carriers in GaAs do not have potential energy.

Therefore, whatever enhancement of energy density is achieved is translated into enhancement of the electric field. This can be formally seen from the fact that in doped GaAs the value of $\partial\left(\omega\epsilon\right)/\partial\omega \sim 25$ is significantly less than in SiC.

Finally, for the MIM structure – referred to by us as "*metal photonic*" (Fig. 3.3(b)) – the field enhancement is much stronger in magnitude while simultaneously occurring over a much wider bandwidth than that of either "*phononic*" or "*all-dielectric photonic*" structures. Because the electron density in metal is very high, and the high-density electrons can support strong surface currents, the energy is confined inside the dielectric gap. Since the free conduction electrons have no potential energy, the strong energy density enhancement is directly translated into the enhancement of the electric field. The width of the resonance, as in the case of all photonic structures is determined by the strong radiative coupling of this patch antenna rather than by the intrinsic material damping. This breadth of the resonance makes MIM less effective than dielectric structures for "passive" sensing applications where one tries to sense minute changes of the refractive index or absorption by observing the shift of the resonances. But MIM with its much higher field enhancement is far more effective in "active" sensing based on photoluminescence [112], Raman scattering [113], Surface Enhanced Infrared Absorption Measurements [114], as well as in such potential applications as photo detection and nonlinear optics [93, 115]. In the end, in order to obtain a strong local electric field, it's necessary to excite large numbers of oscillating dipoles with a small mass, and from this point of view, metal still remains the best choice. This is confirmed by Fig. 4-3(b) and Fig. 4-4 where one can see that the maximum field enhancement obtained width SiC and GaAs patch antennas are much smaller, than with the MIM patch antenna. That is because for the SiC patch antenna, a large chunk of energy is trapped in the form of potential energy; and for the GaAs patch antenna, most energy dissipates inside GaAs.

4.4 Conclusions

To summarize, in the mid-IR spectral range, the scope of material systems capable of providing strong field enhancement broadens beyond metals to include heavy doped semiconductors, as well as polar dielectrics operating either within or near their Reststrahlen region. While all of these alternative systems have intrinsic energy loss rates that are much smaller than those in metal, the large density of free carriers in metals assures that the effective modal loss is small as the energy is concentrated outside of the metal, and the magnitude of the field enhancement in the MIM nanoantenna is much larger than is achievable with any alternative material. That makes these "*metal photonic*" structures the best candidates for a large variety of IR sensing and other applications, but not all of them as the all-dielectric phononic and photonic structures offer the important advantage of narrow linewidth which makes them preferable for a number of sensing applications, and, perhaps in thermal photovoltaics [116]. Highly doped semiconductors offer neither strong field enhancement nor narrow linewidth, but due to the ability to integrate them with electronic devices, such as photodetectors, as well as their inherent tunability, these materials may also find their niche.

Chapter 5

Nanoimprinted Mid-IR Corrugated Metal-Insulator-Metal (MIM) Metasurfaces

5.1 Introduction

As we mentioned in Chapter 1, metasurfaces are inherently two-dimensional (2D) metamaterials, composed of monolayer or few-layered planar stacks that offer same functionality as bulk metamaterials but in a more compact, lighter and loss-efficient manner (lower Q-factors)[117]. Metasurfaces can even manipulate light in more complex ways in 3D to create broadband circular polarizers [118], quarter wave plates [21], helical phase beams [119] and computer generated holograms [120]. As compared to fully 3D metamaterials, a major advantage of metasurfaces is that they are easier to fabricate as most lithographic patterning techniques are inherently planar. With metal, dielectric and semiconductor building blocks at their core, metasurfaces can be patterned using wafer-scale production with integration capability [121]. This key feature is critical to advance practical use of this promising technology in smart nanophotonic and optoelectronic devices [122]. In this work, we demonstrate the design and characterization of mid-IR metasurfaces fabricated using Nanoimprint lithography (NIL) on rigid substrates. By combining NIL with photolithography, we are able to mass produce millimeter scaled arrays with a variety of designs including novel 2D

cantilevers and even 3D accordion-like shapes with widths ranging from 400 to 600 nm and lengths ranging from 4 to 6μm. We characterize the mid-IR optical response in transmission and reflection using Fourier transform infrared (FTIR) microscopy and simulate the spectral response using Finite difference time domain (FDTD) calculations which are in good agreement with experiments. The high throughput fabrication methods offer the possibility of cost-effective fabrication of large area metasurfaces for scalable photonic and plasmonic devices with significant tunability in structure and optical characteristics. For metasurfaces of relevance to visible and infrared (IR) devices such as antenna sensing [123, 124], spatial and spectral emission control [125], perfect absorption via selective narrow-band and dual-band emission [126], radioactive cooling via solar reflectors [127] and label-free analyte-sensitive biosensing using multi-resonant responses [128], there is a prerequisite for highly parallel sub-micron patterning over large areas. Currently, most devices are fabricated using Electron-Beam Lithography (EBL) and Focused-Ion Beam lithography (FIB)[129, 130]. EBL and FIB offer high resolution but are serial techniques with low throughput and high cost. In contrast, nanoimprint lithography (NIL) [131] which uses stamps and molds allows high fidelity parallel patterning using with resolution as low as 10 nm. Like photolithography, NIL also allows repeated replication of nanoscale patterns over larger areas as the stamps and molds are reusable. Unlike photolithography, NIL relies on the thermo-mechanical deformation of polymeric resists and consequently the resolution is not limited by diffraction. NIL has previously been used to fabricate metamaterials and metasurfaces to achieve different predictable photonic effects. Initially NIL was predominantly used to exploit the localized surface plasmon resonance (LSPR) and ensemble electron density oscillations observed in noble metal nanoscale patterns [132]. Subsequently, NIL was also used to create plasmonic waveguides either planar ones on thin metal strips [133, 134] or over profiled metal surfaces [135, 136]. Experimental realizations for a wider range of wavelengths have also been realized. For example,

Wu et al. [137, 138] reported fabrication of a mid-IR metamaterial and Yao et al [139] fabricated a large area metasurface with stacked subwavelength gratings and observed asymmetric transmission response with superior extinction in visible to mid IR range. NIL has even been creatively used in derived forms, such as to make exotic multilayer structures based on a stacking process to demonstrate negative index 'fishnet' and 'Swiss-cross' metamaterials [140]. Another such variant is soft UV-NIL where the soft polymeric stamp is transparent and in contact with UV-curable resist in absence of external pressure. This method was used to make 2D nanocavities for biosensing with near perfect absorption capability in the near IR [141]. A similar fabrication methodology was used to make cylindrical nanowells for LSPR sensing and SERS substrates [142]. With the aid of angled deposition, elliptical gold nanodisks were realized for clinical immunoassay [143] which highlights the geometric adaptability of NIL. Direct nanoimprinting on metallic films [144] or nanoparticles [145] has also been previously utilized to manufacture plasmonic nanostructures with strong SERS effects and highly sensitive LSPR sensing arrays respectively. Using colloidal gold nanocrystal based nanoantennas patterned using NIL, Chen et al. [146] demonstrated an ultrathin polarizing plasmonic metasurface and a quarter wave plate. Similar devices when used with a hydrogel layer on top serve as an angle independent optical moisture sensor [147]. More recently, Park et al. [148] patterned Fe/Al_2O_3 films via NIL to engineer the modulation of effective density and refractive index of CNT forests. These examples highlight the compatibility of NIL with diverse types of metallic and non-metallic materials.

Here, we report the design and characterization of mid-IR metasurfaces fabricated using NIL coupled with conventional photolithography. Our metasurfaces consist of sub-micron periodic antenna units with selective dual band spectral responses in the wavelengths $4 - 6$m and $10 - 15\mu$m. We were motivated to mass produce mid-wave IR (MWIR) responsive metasurfaces for several reasons. First, the atmosphere is

transparent in two mid-IR windows [149, 150] due to minimal vibrational and rotational absorption of atmospheric gases such as oxygen and carbon dioxide [151]. Consequently, signals in the mid-IR are widely used for environmental and remote sensing [152]. Second, commonly encountered thermal emissions from humans and hot objects such as aircraft engines correspond to temperature ranges of 300 to 1000 K in the MWIR band [153]. Thus MWIR metasurfaces have potential applications in energy harvesting, tracking, camouflaging, and ambient radiative cooling. Conventional MWIR optics requires is bulky and expensive. Finally, the losses in metallic metasurfaces are lower in the MWIR range as compared to shorter wavelength regions such as the visible or near IR. We note that NIL allows us to create features on the order of several hundred nm which is commensurate with the subwavelength size and periodicity of 'meta-atoms' in the MWIR range. We utilize a comprehensive approach for design and prediction of the optical responses for various antenna shapes and sizes in the mid-IR wavelengths using numerical simulations in COMSOL. Using the fabrication protocol described lin subsequent sections , we reproducibly create metasurfaces over large areas using NIL and measure the optical responses using Fourier transform infrared (FTIR) microscopy. We observed good agreement between simulations and experiments. The results demonstrate the versatility of the method for two different types of metasurfaces: disjointed-hook (DHM) and accordion-like (ALM). Our study demonstrates that the electromagnetic wave can be artificially modulated by designing optical nano antenna array.

5.2   Design of Mid-IR Metasurfaces

Our two-fold comprehensive approach uses numerical simulations in finite difference time domain (FDTD) to design and predict the optical response in transmission and reflection for various antenna shapes and sizes in the mid-IR wavelengths. Using the fabrication protocol described later, we reproducibly make these metasurfaces and

the results demonstrate the versatility of the method with different geometries. Later, we characterize them using Fourier transform infrared (FTIR) microscopy to achieve reasonable agreement with our FDTD calculations in the form of shallow dual band mid-IR response for different cases. The metasurfaces are designed to have novel optical properties in the Mid-IR region via 2-D nano-optical antenna arrays. For the radio frequency and microwave regimes antennas are widely used to convert electromagnetic radiation into localized energy and vice versa. But at optical frequencies, lenses and mirrors are used to redirect the wavefronts of propagation radiation and the antenna concept is widely unexplored. Consequently, the best possible localization of optical radiation is governed by the diffraction limit. Many foreseeable application can be expected by extending the antenna concept into the optical wavelength range, such as high-resolution microscopy and spectroscopy, optical sensors, photovoltaics, solid state lighting and lasing. Traditional antenna design makes use of structures with characteristic length L that are directly related to the wavelength λ of the imcoming (outgoing) radiation, such as $L = \text{const} \times \lambda$, where the constant is an antenna-design constant. For example, an ideal half-wave dipole antenna is made of a thin rod of length $L = (1/2)\lambda$. However, at optical frequencies the simple wavelength scaling breaks down due to the the fact that incident radiation is no longer perfectly reflected from the antenna surface. Instead, the radiation with higher frequency penetrates into the metal and cause the oscillations of the free-electron gas. So, at optical frequencies the antenna no longer responds to the external wavelength but to a different effective wavelength λ_{eff}, which depends on the material optical properties. Some experiments showed at optical frequencies the wavelength λ should be replaced by a shorter effective wavelength, and in these experiments the resonance of lithograohically fabricated antennas turned out to be 20% shorter than the value predicted by antenna theory. In [154], Lukas Novotny derived the linear scaling law for the effective wavelength λ_{eff}

in the form,

$$\lambda_{eff} = n_1 + n_2[\lambda/\lambda_p], \tag{5.1}$$

where λ_p is the plasma wavelength and n_1,n_2 are the coefficients with dimensions of length that depend on antenna geometry and static dielectric properties, here the assumptions are that the antenna is make of liear segments with radius $R \ll \lambda$, and the metal can be described by a free-electron gas according to the Drude model.
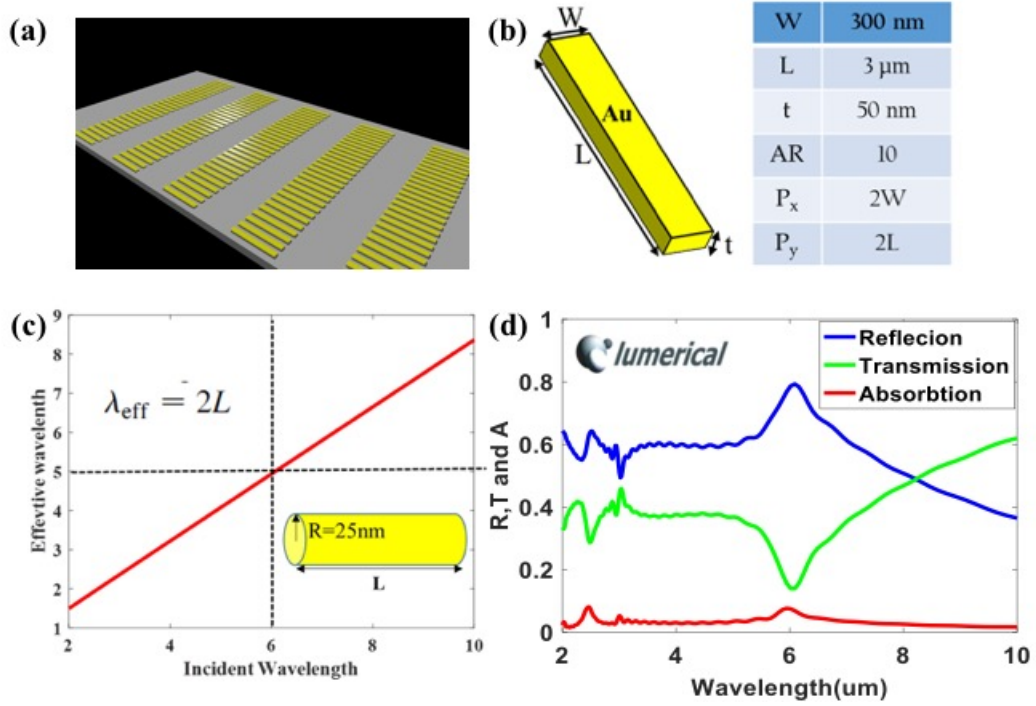
Figure 5-1. (a) The metasurfaces consist of optical antenna array; (b) The size information of single optical antenna; (c) The effective wavelength VS. incident wavelength for optical rod whose length is 2.5μm, radius 25nm; (d) The simulated optical response of the designed metasurfaces in (a), obtained through Lumerical FDTD.

As we mentioned before, our aim is to design and lab fabricate metasurfaces which can modulate the radiation of electromagnetic wave via optical antenna. Suppose we want to design a metasurface that has high reflection at 6μm, then based on the effective wavelength theroy in [154], as shown in Fig. 5-1 for the metal (Au) rod with raidus 25nm, the length should be $2.5\mu m$. But for the convenience of lab fabrication, rectangle antenna is more easy to fabricate than rod, hence as shown in Figs. 5-1 (a)

and (b), the metasurfaces consists of rectangle optical array are designed, the thickness of single rectangle optical antenna is 50nm and the length and width are 3μm and 300nm respectively. Fig. 5-1(d) are the spectrum of the designed metasurfaces, we can see that at $\lambda = 6\mu$m, the designed metasurface does have higher reflection, which is what we want.

From the simulation we can see that we have successfully designed the metasurfaces with the optical properties we want via the designing of optical antenna array. Next, we fabricated the above metasurfaces in our lab then tested the fabricated samples using FTIR. However, due to the fact that the optical antenna array was directly on the top of silicon wafer, and the thickness of the silicon wafer we used is about 1mm, and the wavelength range we used is 2μm to 20μm. Hence, when we use FTIR to measure the spectrum of the samples, the Fabry–Pérot resonance caused by the reflection of up and bottom surfaces are very strong, and we cannot observe the expected spectrum as shown in the simulation.

To get rid of this issue, we decided to change our structure. Instead of depositing the optical antenna array directly on the top on silicon wafer, fist of all, we deposit metallic (Au) ground plane directly on the top of silicon wafer, this metallic layer should thick enough to prevent the light transmission and can guarantee better light radiation modulation. Then on the top of ground metallic layer is a dielectric layer, the properties of this dielectric layer, such as index, thickness, can affect the performance of the metasurface. Finally, on the top of the dielectric layer is optical antenna array. By doing this, the optical antenna is spaced from the ground metallic plane, by using this configuration, this three layer metasurface couples to both the electric and magnetic components of incident electromagnetic waves and allows for minimization of the reflectance, at a certain frequency, by impedance matching to free space. Also, due to coupling, the frequency or the wavelength at which that the strongest modulation happens will be different with the effective wavelength theory. So we believe that

compared to our previous geometry, this configuration has better performance in the electromagnetic radiation modulation, and with the absence of silicon wafer caused Fabry–Pérot resonance, we can easily get the spectrum. Figure 5-2 shows the geometric structure and the size information of the three layer metasurface.
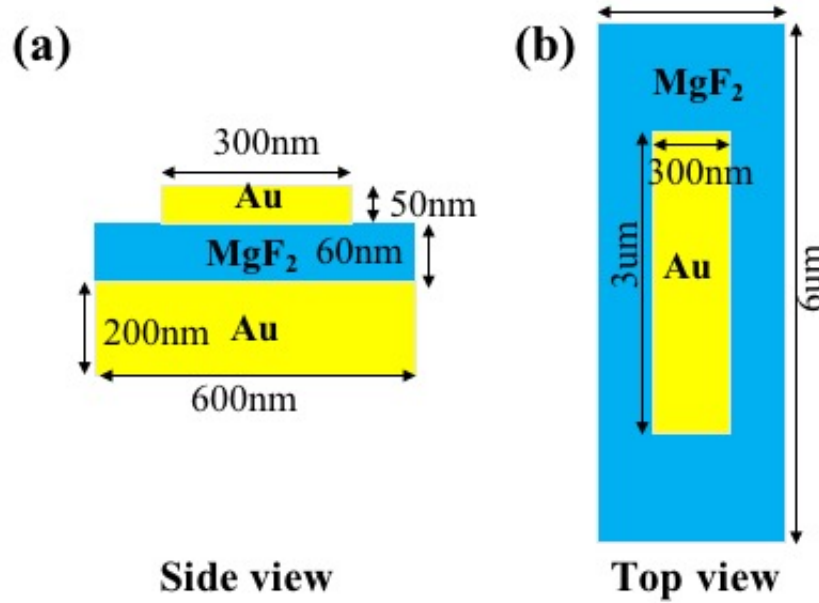
Figure 5-2. Side (a) and Top (b) view of the three layer metasurface.

5.3 Lab Fabrication of Mid-IR Metasurfaces

We first spin coated a thermally curable resist NXR-1025 (7%, Nanonex Corp) at 2000 rpm and baked the resist at 115°C for 1 minute. We stamped the wafer using a commercial NX-2000 imprinting tool with an $8 \times 8mm^2$ mold (LightSmyth) with the nanolines feature. Stamping was performed via a controlled cycle with an applied peak pressure of 200 psi and peak temperature of 120°C. The resulting samples were loaded in a dry planar etcher with 22 sccm oxygen flow at 100W RF power for a minute to reach the bottom of the substrate as shown in Fig. 5-3(D). Next, using thermal evaporation in tungsten boats, we deposited $(5 - 10nm)$ adhesive layer of chromium followed by 50nm thick gold film at a deposition rate of 0.1˘1Å/sec in 1×10^{-5} torr

chamber pressure. After this step, the residual imprint resist was dissolved in acetone for lift-off metallization using a sonication bath. Till this part, the desired width of the said nanoantennas was achieved.
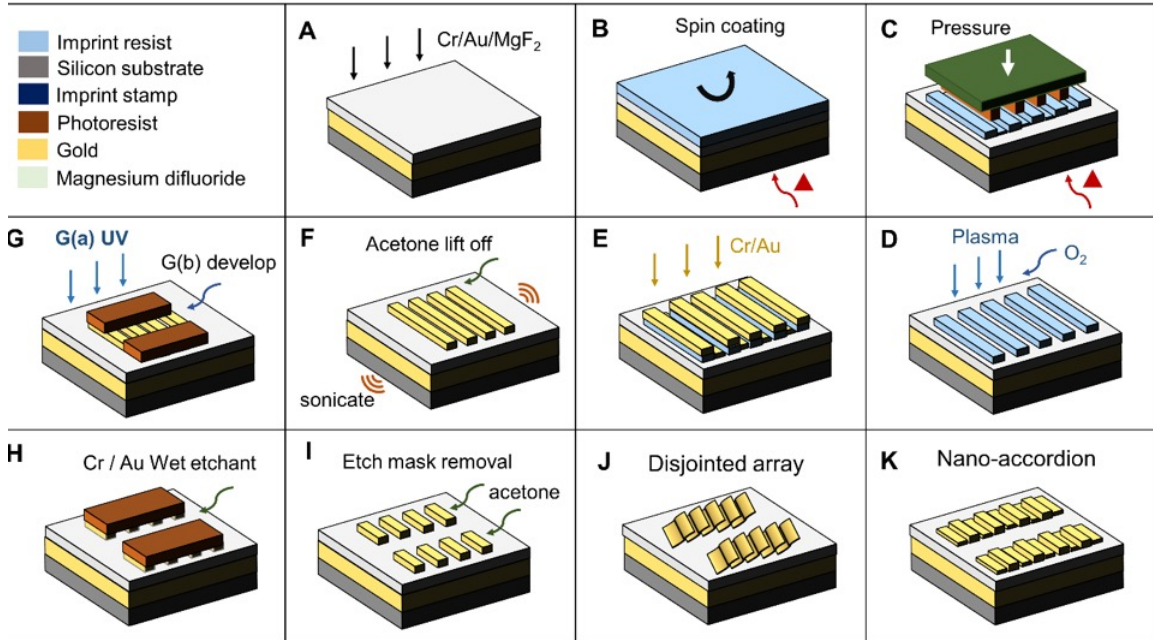
Figure 5-3. General fabrication process of both metasurfaces types: (a) Thermal deposition of Au followed by MgF_2 onto silicon substrate, (b) Spin coating of the thermoplastic resist on top for imprint process, (c) Pressure and temperature controlled NIL step under vacuum to transfer nanolines, (d) Removal of residual resist after NIL using oxygen plasma descum to reach the substrate, (e) Thermal deposition of Au thickness desired preceded by adhesive layer of Cr, (f) Lift-off metallization by sonicating in acetone bath to remove the resist, (g) Photopatterning of the resist etch mask perpendicular to direction of imprinted lines and developing thereafter to expose the unwanted Au, (h) Wet etching of Au followed by Cr in a bath using commercially available selective etchants, (i) Removal of etch mask resist layer using acetone, j) Final end product metasurface with disjointed antennas, and k) Final accordion metasurface with corrugated joined antennas

In order to fabricate rectangular cantilevers from above obtained nano-lines, we further spin coated a second UV-curable photoresist S1805 by Microposit at 4000 rpm and then baked it at 115°C for a minute. I-line (365 nm) exposure was done using a Neutronix NXQ 4000 mask aligner and the resist was developed using MF-319 developer for 7 sec. The photopatterning alignment was done such that the micron-sized periodic line pairs on the chromium photomask were orthogonal to the imprinted

metal lines, hence this step determined the final length of our antennas. The unmasked metal regions between any two resist line pairs were dissolved at room temperature using a commercially purchased wet etchant GE-8110 by Transene. The chemistry was selective towards gold and mixed with surfactant to enable wetting. Chromium etchant CR 1020 AC was applied to remove the underlying chromium below the gold removed. Eventually, the resist was washed off using acetone to give rectangular cantilever-shaped antennas. The aforementioned protocol for making single layer metasurfaces can be adapted for metal-insulator-metal (MIM) structures with the addition of two preceding steps. First, was thermal evaporation of the back reflector metal layer with thickness about 200 nm, followed by a subsequent deposition of the 60 nm thick dielectric spacer layer, which was magnesium fluoride (MgF_2) for our study. The transmission and reflectance measurements for our metasurfaces were taken using a Bruker Tensor 27 FTIR spectrometer coupled to a Hyperion 2000 microscope. The incident light from the source was focused on the sample using a 15X visible-cum-IR objective (NA = 0.4) while it is collected back by a liquid nitrogen cooled mercury cadmium telluride (MCT) detector. Transmission measurements were performed for normally incident IR light while in case of reflection, the weighted average angle of incidence was 20°. A gold mirror was used to normalize all sample spectra for reflection while an open aperture (air) was used for transmission. The collection area was confined to $100 \times 100 \mu m^2$ by a rectangular glass aperture to consider a region with low defects. An IR polarizer was placed in the path of incident light before meeting the sample at 3 optional angles of 0°, 45° and 90° to generate linearly polarized light with parallel, diagonal and perpendicular states with respect to the antenna. No analyzer for the resulting light off the metasurface was used. All spectra taken for the samples and background were collected from 2 to 16 μm at a resolution of $1 cm^{-1}$ containing 64 scans with a mirror repetition rate of 20 kHz. Since there is no dry air purge unit around the sample, the spectra were later corrected using the atmospheric

compensation tool (for H_2O and CO_2) in OPUS package by Bruker and post processed for smoothening by Savitzky-Golay algorithm.

5.4 Characterization and Optical Response Measurement of Metasurfaces
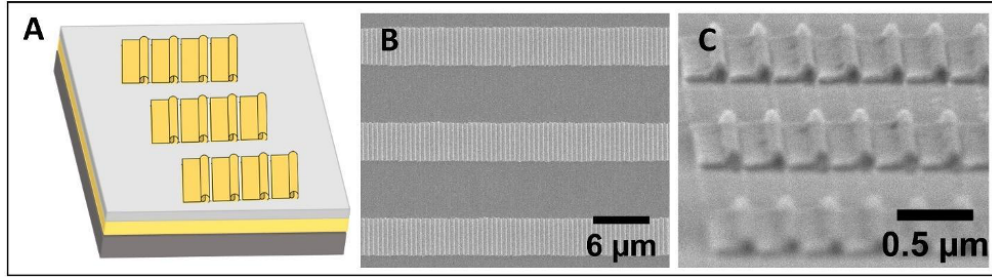
Figure 5-4. (A) Schematic of the metasurface (mts) fabricated in Fig. 5-3(J) identifying the underlying silicon substrate, the thick metal layer, insulator layer and the gold nanopatterns on top. (B) Large area SEM micrograph of DHM and (C) the magnified SEM with a tilted side view to show the novel s-topography of the individual antennas.
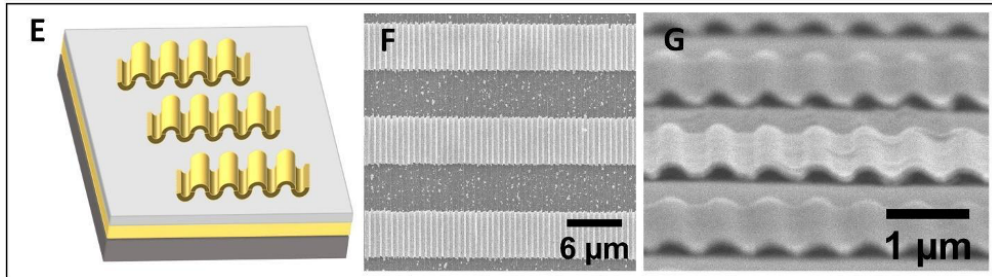
Figure 5-5. (A) Schematic of the metasurface (mts) fabricated in Fig. 5-3(J) with the same underlying layers and thicknesses as figure 2. Inset also shows a top view SEM image that made us call it accordion-like metasurface (ALM) (B) Large area SEM micrograph of ALM and (C) the magnified SEM with a tilted side view to show the continuous connectivity of the antennas.

Our fabrication procedure is highly scalable and extremely effective in creating differently sized antenna components by simply using molds and masks of varying lateral characteristics (duty cycle or period, line width, depth, angle of photopatterning). The SEM images in Fig. 5-4 show the good imprint integrity (negligible residual layers) and high fidelity patterns over large areas as designed in the schematic. The

progressively zoomed micrographs specifically show disjointed array of antennas that are asymmetric along their width (hook-shaped topography) with approximately 50 nm height, 490 nm wide and 5.5μm long with a period of 510 nm along the width and 10.1μm along the length. The non-continuity and thickness of gold antennas is crucial in determining the LSPR activity for this case as explained later. The geometrical measurements of the patterns were done using ImageJ analysis of these SEM images. Similarly, from Fig. 5-5 we realized the symmetric 3D accordion antenna array. The high magnitude SEM images show that the antennas are connected uniformly along the longer edge. High fidelity nanopatterning of the top most gold antenna ensemble was realized in both cases. A non-trivial asymmetric topography is obtained in case of DHM over a large area as shown in panels B and C of Fig. 5-4. The antennas are separated along the right longitudinal edge and are closely packed adjacent to each other. In case of the ALM, a continuous periodic corrugation was achieved in the top gold layer. The surface profile is smoother for this case compared to DHM. A key visual queue that differentiates otherwise seemingly similar metasurfaces is that if one performs an asymmetric cross-sectional but periodic partitioning of the top gold layer in ALM, the DHM topography can be fathomed. Hence a simple yet elegant variation in lithography can be creatively exploited to fabricate tunable metasurfaces.

The bottom gold layer in our metasurfaces was sufficiently thick to prevent any transmission to take place when the light is incident from above. Based on the electromagnetic resonance in metal-insulator subwavelength bilayer, we saw reduced reflection for certain mid IR frequencies. We have analyzed the reflection responses for 3 different cases and compared our results with the experimental measurements. The panels A, B and C in both Fig. 5-5 and Fig. 5-6 represent the predictions from COMSOL while the panels D, E and F show the FTIR measurements over the same wavelength range, respectively for DHM and ALM. The blue and the green curves denote the measurements taken with the incident light polarized along the longer and
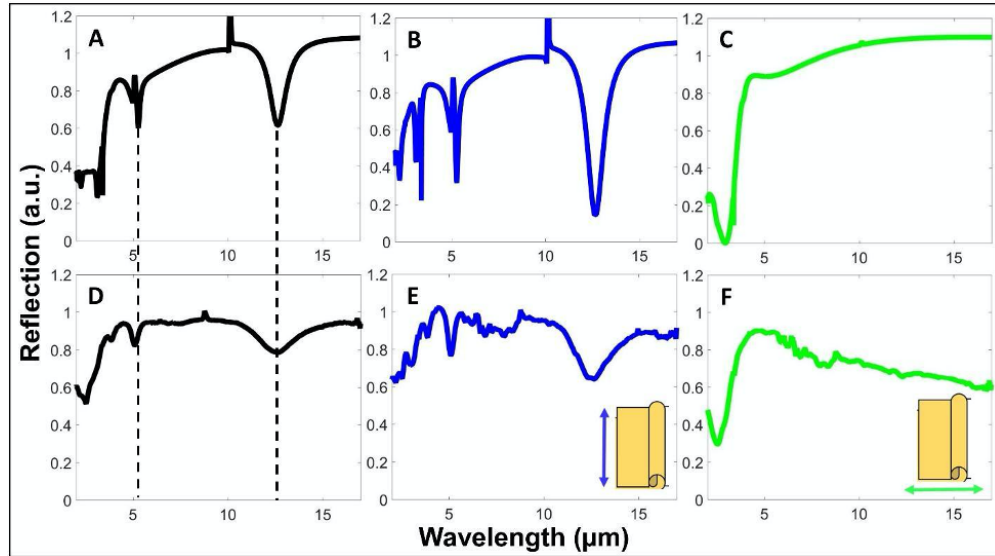
Figure 5-6. (A-C) are the reflection obtained through COMSOL simulation. (D-F) FTIR Reflection measurements for DHM explained in Fig. 5-4. The IR polarizer used generated linearly polarized incident light at different angles with respect to the antenna, from (D) being no polarizer in beam path (black curve), (E) polarization along length of antenna (blue curve), and (F) polarization along the width of antenna (red curve).

shorter edge of the antennas respectively, while the black curves are for the unpolarized incident light. While it was experimentally possible to measure for all the 3 cases in our FTIR setup using an IR polarizer as described earlier, the FEM calculation for the no polarization case (panels A) was taken as a mean of the cases in panel B and C. For the DHM, we have observed significant reflection minima in 3 different mid IR regions at around 2, 5 and 12μm respectively. The responses near 5 and 10μm originate from the surface plasmon resonances along the longer edge of the antennas as realized in panels B and E of Fig. 5-5. why, the response at 2μm is related to the plasmon resonance along the shorter edge of the antenna as seen in panels C and F of Fig. 5-5. In comparison, for the ALM case, we have observed same resonances at longer wavelengths of 5 and 12μm, with no discernable featuresseen at shorter wavelengths. The overall symmetry of the structure along the shorter edge doesn't generate the desired plasmonic interaction to limit the reflection for higher frequencies as seen in green curves in panels C and F of Fig. 5-6. All the LSPR interactions

observed at various wavelengths in FTIR responses are mostly consistent with the full wave simulations in the panels above of same figures. When light is polarized along the shorter dimension, LSPR occurs at the highest energy (transverse) and conversely at the lowest (longitudinal) when along the longer dimension. This ability to differentiate between 2 modes is possible with the orientation control given by NIL as opposed to average of irregularly shaped structures chemically synthesized. This is in agreement with the reflection measurements in both cases where the blue curve (L pol) contributes to the main peak responses. The position of these responses can be controlled and tuned using prefabrication changes. We also compared the reflection responses of metasurfaces in Fig. 5-6 and Fig. 5-7, the reflection dip observed around $\lambda = 2.5\mu$m for DHM is completely absent in the ALM. This shows that a simple change in the design can alter the optical nature of the said device from multi band to dual band response. In order to facilitate understanding of these symmetry driven
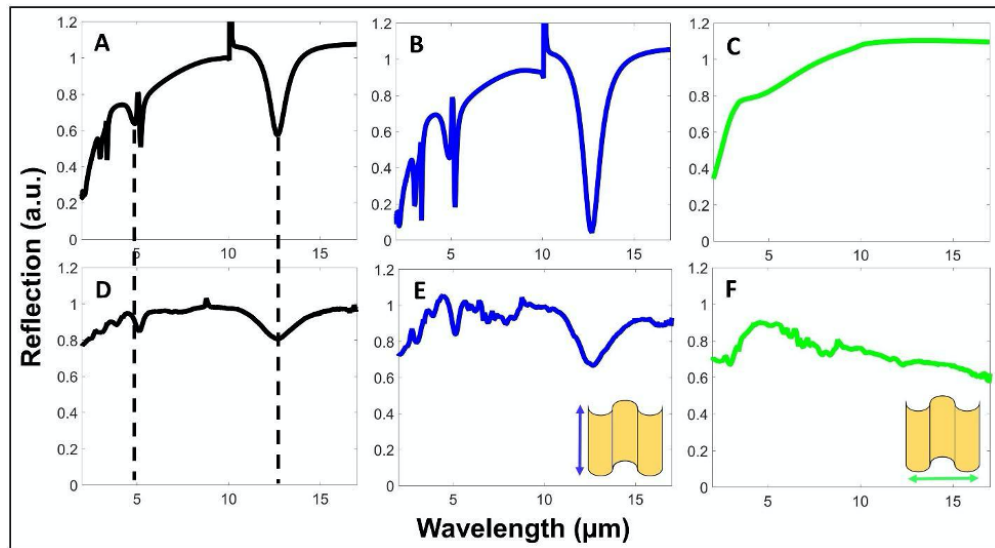
Figure 5-7. (A-C) are the reflection obtained through COMSOL simulation. (D-F) FTIR Reflection measurements for ALM explained in Fig. 5-5. The IR polarizer used generated linearly polarized incident light at different angles with respect to the antenna, from (D) being no polarizer in beam path (black curve), (E) polarization along length of antenna (blue curve), and (F) polarization along the width of antenna (red curve).

reflection responses governed by LSPR at the metal-dielectric interfaces, we also
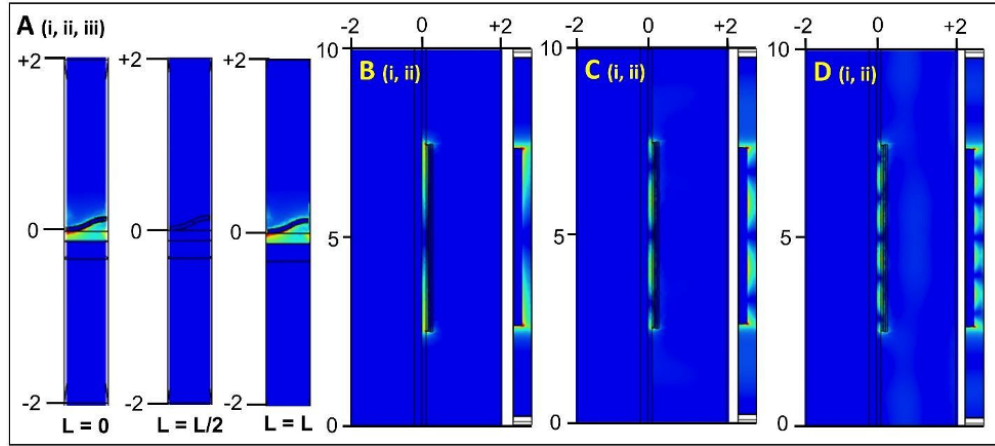
Figure 5-8. Electric field distributions around the DHM unit cell with (B), (C) and (D) representing the valleys observed in reflection response starting from right to left, and (i) and (ii) denote the side view and top view respectively.(A) shows the cross sectional view taken at 3 different planes: 2 ends of the antenna [(i) L = 0 and (iii) L = L] and one at the middle [(ii) L = L/2]
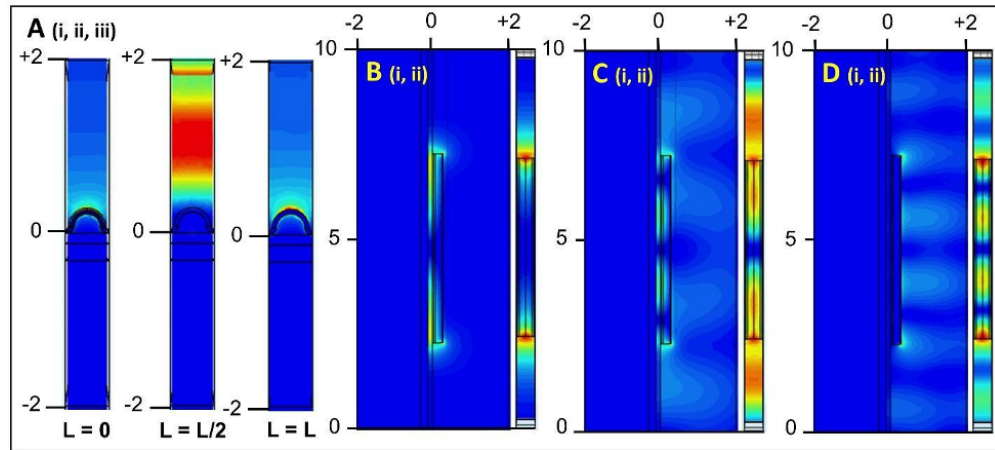
Figure 5-9. Electric field distributions around the ALM unit cell with (B), (C) and (D) representing the valleys observed in reflection response starting from right to left, and (i) and (ii) denote the side view and top view respectively.(A) shows the cross sectional view taken at 3 different planes: 2 ends of the antenna [(i) L = 0 and (iii) L = L] and one at the middle [(ii) L = L/2]

studied the electric field intensity distributions in the DHM and ALM unit cells. The intensity plots were calculated for different orders of LSPR as seen in Fig. 5-6 and Fig. 5-7. The first order being the higher intensity one, located around 12μm, second order near 12μm and the third at 2μm. While there may have been more orders occurring on either sides of the spectrum, we only kept mid IR wavelengths as our region of

interest for the purpose of this work. The asymmetry in the DHM manifested itself in the hot spot locations of the resonances as shown in Fig. 5-8 for the side view along length [panels B (i), C (i) and D (i)] and the top view as seen by encountered by incoming light [panels B(ii), C (ii), D (ii)]. For the side view, the unit cell plane used cuts the antenna on the left edge while the top view unit cell plane coincides with the interface between top metal and dielectric layer. Same holds true for Fig. 5-9. The said hot spots are shifted towards the right for the DHM, where the antenna rises in the out of plane direction. Juxtaposed against ALM, we saw more intense hot spots with ideal symmetry in the top view planes for all the orders [Fig. 5-9 panels B (ii), C (ii), D (ii)]. Given their smoother edgeless topography, the fields also extend further in the unit cell area under consideration than the DHM LSPR activity. Hence it can be conclusively said that the geometric asymmetry in the DHM manifested itself in the hot spot locations of the resonances, likewise symmetry played the same role in ALM. More specifically to explore the plasmonic interactions taking place along the width of these antennas, where the asymmetry or symmetry lies, we further looked into electric field intensity distribution for the longest wavelength (12μm), evaluated at 3 different orthogonal planes: 2 at the edges [panels A (i, iii)] and one at the center [panels A (ii)] in both Fig. 5-8 and Fig. 5-9. The hot spots were realized at the edges for DHM as opposed to the center for ALM. This observation establishes that the resulting distributions for the 2 cases are spatially complementary to each other. Using subtle symmetry manipulations in our metasurface fabrication we achieved contrasting plasmonic responses for reflected light, which can be visualized as a logic gate type control system for infrared light.

5.5   Discussion and Conclusions

The general profiles of FEM and FTIR for both cases were in great agreement in terms of positions of band responses and baseline trends. There are a few disagreements

101

present but we have sufficient insights to explain them: (i) the overall noise in FTIR measurements is higher compared to their smooth FEM counterparts. This can attributed to the ideal surface profiles constructed in COMSOL which can't be said for the fabricated metasurfaces. The process of thermally evaporating a dielectric material is susceptible to the grainy morphology of the resulting thin film. The resulting bumps or cavities created further contribute to both enhanced scattering and a more diffused reflection rather than specular. It consequently results in greater noise and (ii) low amplitude response since a lesser intensity of light is interacting with the metasurface compared to the simulation unit cell. The FTIR reflection data was corrected by a factor of 2 to take into account the 50% reduction in overall light intensity occurring due to presence of the polarizer in beam path. Based on the refractive index modelling of MgF_2 in most commonly used commercial Maxwell solvers, which is reliably researched and reported only as far as 7 to 7.5 microns [155] for both ordinary and extraordinary rays, the experimentally observed increasingly lossy behavior for higher IR wavelengths is not fairly captured in our FEM calculations. (iii) The latter hence resulted in an increasingly reflective trend for the region of 7 to 15 microns in contradiction with the FTIR measurements. The location of this cut-off wavelength can be accounted for by the vibrational mode phonon energy corresponding to MgF_2 octahedron building blocks in the material's structure [156]. (iv) Another factor that can contribute to the enhanced absorption for certain wavelengths in FTIR data is the fact that the series of fabrication steps employed in our recipe involves extensive use of various cleaning reagents, thermosetting polymers, silanizing agents, photo responsive resists and chemical etchants. Even trace residual amounts of such compounds, comprising an abundance of different bond energies present can interfere with the LSPR interactions which are again not accounted for in the simulations. (v) Sharp fano-resonant features seen in both cases. (vi) Other minor disagreements between the simulations and experiments can be attributed to the imperfections or

defects present on the sample. The experimental measurement conditions (not in vacuum) were different from the ideal simulation. With the use of Cassegrain objectives for FTIR microscopy, the reflected light can never be perfectly normal to the substrate as in case of wave optics module in COMSOL. However, the setup can still monitor a significant amount of reflected light and, therefore shouldn't alter our conclusion. The reflection of the MIM structure that we examine in this paper is determined by several elements. Since, the electromagnetic resonance on the top antennas is excited by the external incident electromagnetic wave, hence both the size of the antenna and the polarization have effect on the reflection spectrum. The bottom metal (Au) acts as a mirror, which couples to the resonance of the top antenna, enhances the interaction, then both the distance between antenna and bottom metal and the material between them will impact the interaction. As a summary, by changing the size and polarization, we can change the resonance wavelength, hence the position where the trough in the spectrum shows. Because different resonance modes can be excited by the external incident electromagnetic, we can see that there are sever troughs in the spectrum. By changing the distance or the material between the top and bottom metal, we can change the depth of the trough of the spectrum, and potentially make the MIM structure a perfect absorber.

Overall, our work demonstrated two subtly different metasurfaces with novel topographies operating in the mid IR region with highly tunable and complementary plasmonic responses sensitive to the state of linear polarization of the incoming light. To establish perspective towards the novelty of the morphology aspect of these metasurfaces and how it affects the accompanying surface plasmonics, we can compare their reflection response towards polarized light in two different states (along the length and width of antennas) to the control cases where the antennas lack any apparent degree of patterning: a single continuous flat strip of gold and non-corrugated rectangular cantilevers. By introducing these asymmetric and symmetric curvatures periodically

over a large area of the semiconductor substrates, allows us to achieve true manipulation of possible IR responses on the spectrum scale indicated by easily distinguishable and drastically unique plasmonic activity. This feature can be efficiently employed to accomplish otherwise esoteric tasks like precise biosensing of molecules in low concentration or in vivo SERS, when the antennas are patterned to realize a plasmonic resonance that fit into the energy transparency windows of the biological sample under consideration. Key shortcomings of the outcomes were thoroughly discussed and recommendations were outlined to address them. Further experimentation is needed to fabricate more complex and truly 3D metamaterials by using these surface characteristics as building blocks arranged in polyhedral spatial fashion. The materials and manufacturing techniques used for in making these metasurfaces underline the compatibility with semiconductor industry's conventional CMOS tech. Scalable and planar aspects our device can comply with the increasing demand for miniaturization of optical components for compact portable device utilities, especially where on chip integrations are required. A significant portion of findings till date have heavily explored visible or near IR wavelengths, leaving out mid IR domain due to less advanced manufacturing methods and very expensive characterization techniques, and our research surely attempts at addressing that complaint by developing solutions that agree on both experimental and modelling fronts. In the end, we realize large area manufacturing of multilayer plasmonic metasurfaces using NIL and conventional photolithography. The wavelength response can easily be shifted to visible and near IR regimes when imprint stamps with features around 100 nm with varied packing density are used. By altering the amount of plasmonic metal deposited, the intensity of response can also be enhanced. We believe that the amplitude we achieved can be sufficient for biomolecular sensing applications. When used in tandem with novel thermally, chemically or mechanically responsive materials or opto-electronically relevant family of 2D layered materials, these metasurfaces can generate further exotic

properties. Therefore, low cost fabrication protocols like ours hold great promise to advance the industrial realization of such neatly defined nanoscale metamaterials for manipulating light.

Chapter 6

Reversible MoS$_2$ Origami with Spatially Resolved and Reconfigurable Photosensitivity

6.1 Introduction

Two dimensional layered materials (2DLMs) have attracted more and more attentions in the fields of electronics [157], opto-electronics [158], energy [159], and sensing applications[160], due to their unique properties [161] including atomic-scale thickness, excellent electrical, thermal characteristics, high stability and mechanical strength [162, 163]. Despite significant progress, most monolayer 2DLM-based functional devices are configured on rigid planar substrates which can limit device functionality and increase overall device size. Because monolayer 2DLMs are extremely thin, they possess low bending rigidity [164], and it has been suggested that they could be curved or folded to create three-dimensional (3D) flexible and reconfigurable devices with small form factors [165, 166]; however, achieving this vision is challenging [167]. Most high-quality monolayer 2DLMs are grown on rigid substrates using high-temperature chemical vapor deposition (CVD) approaches not compatible with flexible and stimuli responsive polymeric materials. Also, due to the extremely low bending stiffness and strong van der Waals interactions between these ultrathin films, it is challenging to achieve well-controlled and reversible folding [168, 169].

Three-dimensional structures offer significant advantages for opto-electronic applications as has been demonstrated with conventional semiconductors such as silicon and III-V materials [170, 171]. For example, macroscale 3D silicon photovoltaic (PV) structures with integrated absorbers and reflectors [172] or kirigami-patterned gallium arsenide solar cells [173] were shown to generate much higher energy densities as compared to flat PV panels. For photodetection and imaging, 3D deformable silicon photodetector arrays were shown to have nearly infinite depth of field and a full field of view with zero aberration [174, 175].

2DLMs have unique advantages over conventional semiconductors in opto-electronics [176, 177], including light absorption over a wide energy spectrum, ultrafast carrier dynamics, tunable optical properties via doping, and low dissipation rates [178]. However, their atomically thin structure is a limitation in optical devices due to low light absorption and limited light-matter interactions [179, 180]. Strain engineering or shape transformation of 2DLMs into well-defined 3D structures provides a promising strategy to overcome this limitation [181–183]. One recent report showed that a mechanically assembled 3D device based on 2DLMs was capable of measuring the direction, intensity, and angular divergence properties of the incident light [184]. However, reversible, reconfigurable, and stimuli-responsive 3D opto-electronic devices based on monolayer 2DLMs have yet to be achieved and this is an important step in the development of biomimetic, adaptive, smart, wearable, and robotic devices [185, 186], such as those capable of sun tracking (heliotropism), leaf opening (nyctinasty), or structurally tuning color [187–189].

6.2   Fabrication and realization of MoS$_2$ Origami

In this work, we reversibly transform monolayer MoS$_2$ from a flat state to complex 3D shapes, by attaching it to differentially cross-linked and stimuli responsive polymer (SU8) films with integrated gold (Au) electrodes. We report several important

advances as compared to prior research. First, we can control both the folding extent and the direction of $MoS_2 - Au - SU8$ based on the tunable photo-cross-linking of SU8; this control enables the folding of complex Miura-ori patterns which require bidirectional hinges with rigid segments. Such geometries represent a significant advance beyond simple self-folded and unidirectionally curved structures such as cylinders and rolls [190]. The realization of the Miura fold pattern is also a major step toward realizing more complicated origami/kirigami-inspired and deployable functional devices. Second, our approach enables the arrangement and reconfiguration of MoS_2-based opto-electronic devices in predesigned 3D patterns, leading to spatially or angle-resolved photodetection and vastly tunable detection area between the flat and folded states. Third, the stimulus responsive folding is completely reversible without the need for tethers or wires, and it also has the advantage of being flexible and soft as compared to inorganic or metallic 3D structures, which paves the way for next-generation adaptive, biomimetic, and environmentally responsive opto-electronic devices. Finally, our 3D fabrication technique is based on SU8, which is a negative photoresist widely used in conventional microfabrication. The fabrication and self-folding process of the $MoS_2 - SU8$ structures with integrated Au patterns is shown in Fig. 6-1 and more details are in the SI. Briefly, the process involved MoS_2 transfer, multistep photopatterning, and etching. We used monolayer MoS_2 film synthesized using metal organic chemical vapor deposition (MOCVD), the details of which can be found in a previous report [191]. The Raman spectrum of the synthesized MoS_2 shows peaks at 386 and $406cm^{-1}$, and the photoluminescence spectrum has a pronounced peak at 658nm, which indicates the high quality of MoS_2 used in this study [192]. We transferred a monolayer of MoS_2 from the growth substrate to the top of a silicon wafer which was coated with a copper or aluminum sacrificial layer. We utilized the poly(methyl methacrylate) (PMMA) transfer method [192]. Then, we deposited and photolithographically patterned Au patterns on the MoS_2 by thermal evaporation and

a lift-off process. We subsequently deposited, differentially photo-cross-linked, and patterned the SU8 into the predesigned 2D shape. We then removed the excess MoS_2 using oxygen plasma etching. Finally, we released the $MoS_2 - Au - SU8$ structures from the silicon or glass substrate by dissolving the sacrificial layer.

Reversible self-folding of the 2D $MoS_2 - SU8$ patterned structures is driven by solvent exchange between a good (acetone) and a poor solvent (water) in the differentially photo-cross-linked SU8 films. We utilized two different approaches to achieve the self-folding of the SU8 microstructures, as illustrated in Figs. 6-1(b) and (c). In the first approach, we fabricated anSU8 bilayer with a partially photo-cross-linked top SU8 layer and fully photo-cross-linked the bottom SU8 layer. In the second approach, we created a cross-linking gradient based on the exponential light intensity decay in a single thicker SU8 layer by low UV dose exposure (Fig. 6-1(c)) [193]. Such differentially photo-cross-linked SU8 films could be created with gradients from either top or bottom by light exposure from the top or bottom of the SU8, respectively, and also interspersed with fully cross-linked rigid SU8 panels to create complex designs of bidirectional self-folding structures needed for Miura-ori (Fig. 6-1(d)). The 3D $MoS_2 - SU8$ photodetectors assembled by self-folding were characterized by measuring the photovoltage during laser illumination at different angles (Fig. 6-1(e)). We were also able to assemble reversible Miura-ori inspired photodetectors with a vastly different optical detection area in the flat and folded states (Fig. 6-1(f)). The fabrication and assembly process are parallel and can be done in a wafer-scale manner enabling the high-throughput assembly of a wide range of curved and folded 3D-shaped devices from their planar precursors. As shown in Figs. 6-2, a pyramid can be generated from its triangular precursor (Figures 6-2 (a,b); a square pyramid structure folded from a star-shaped precursor (Figs. 6-2(e) and (f)); and a closed flower structure folded from a flat six-petal precursor (Figs. 6-2(i) and (g)). It is noteworthy that in these 3D structures, the center SU8 panel are fully cross-linked and pinned on the wafer by the
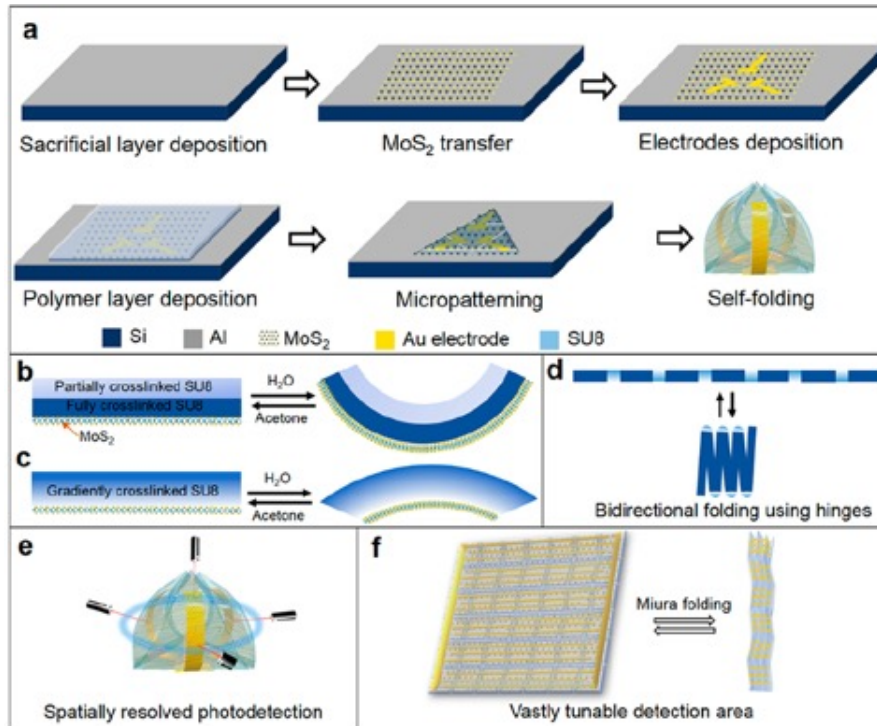
Figure 6-1. Illustration of the fabrication process for 3D self-folded $MoS_2 - Au - SU8$ photodetectors. (a) A sacrificial film was deposited on a silicon wafer substrate, followed by transfer of monolayer MoS_2 and photolithographic definition of Au patterns. Then SU8 was patterned by UV irradiation through a photomask. Finally, the $MoS_2 - SU8$ microstructure was released by dissolving the sacrificial layer and the structures self-folded in water. (b,c) Illustration of the two strategies used to fold the SU8 microstructures. (b) A bilayer SU8 structure with the bottom SU8 layer fully cross-linked, whereas the top SU8 layer partially cross-linked; (c) a thicker SU8 layer with gradient cross-linking density along the thickness. In both cases, reversible self-folding is achieved with solvent exchange. (d) Illustration of bidirectional self-folding of a flat SU8 film into a compact multilayer structure, using two groups of hinges which fold from opposite directions. (e) The 3D $MoS_2 - Au - SU8$ photodetector is capable of spatially or angle-resolved photodetection. (f) Illustration of a flat $MoS_2 - Au - SU8$ photodetector with the Miura pattern that can reversibly fold into a compact multilayer structure with significant difference in optical detection area between flat and folded states.

selective patterning of the sacrificial layer to facilitate imaging and characterization. Selective pinning of different regions of the self-folding structure is important to realize on-chip devices. Alternatively, fully freestanding devices can be generated using an unpatterned sacrificial layer.

We note that the self-folding is uniform with a high yield above 95%. The speed

of the folding process depends on the thickness and the overall dimensions of the SU8. The structures shown in Fig. 6-2 self-folded within minutes after immersion in water (Figure S5) and reversibly unfolded within 20s when the solvent was changed to acetone. This folding and unfolding process can be repeated numerous times (> 20) without noticeable changes in shape. Also, the high quality of the MoS_2 monolayer is retained before and after the solvent-induced folding/unfolding process. We note that chemically responsive self-folding can enable autonomous operation in biological, ambient, and marine environments and acetone and water are common solvents. However, for some applications solvent exchange-induced folding may be not desirable and in these cases one could replace SU8 with alternate stimuli responsive materials such as temperature or light responsive polymers. We investigated the mechanics of the self-folding process by developing a coarse-grained model to simulate the shape transformation. The SU8 photoresist is composed of an epoxy base and photoacid generator. The epoxy groups in the resin cross-link upon UV irradiation and subsequent postexposure bake. Depending on the UV exposure dose, the SU8 can be fully cross-linked or partially cross-linked. We simulated the SU8 bilayer with each of the two SU8 layers represented by a coarse-grained membrane with a facecentered cubic (fcc) lattice (a is the lattice constant) to model the location of the mass beads, and elastic springs to model the interaction between the nearest neighboring beads. The thickness (5μm of each layer) as well as the lateral dimension of each layer was set to match the experimental values exactly. In the $MoS_2 - SU8$ bilayer structures, the bottom SU8 layer was fully cross-linked, whereas the top SU8 layer is partially (about 60%) cross-linked. In the model, the bending stiffness of the fully cross-linked bottom layer (Db) is 4.2×10^{-8}Nům [194] and that of the partially cross-linked top layer (Dt) was approximately 60% of Db and could be varied depending on the cross-linking extent or UV dose (the ratio $\lambda = $ Dt/Db).

When the bilayer is transferred from a good solvent (acetone) to a bad solvent
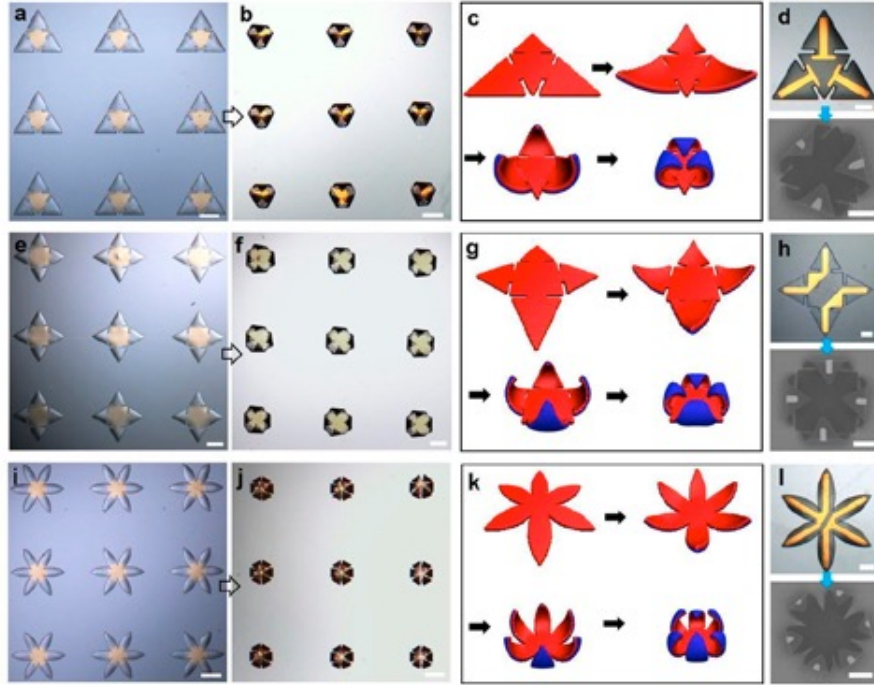
Figure 6-2. Self-folding of $MoS_2 - SU8$ structures with different shapes. (a-j) Optical microscope images of the parallel self-folding process of (a,b) pyramid, (e,f) square pyramid, and (i,j) flower-shaped $SU8$ structures, respectively. The central colored region is due to pinning of the $SU8$ by selective patterning of the sacrificial layer. (c,g,k) Snapshots of the self-folding process obtained from coarse-grained mechanics simulations for the (c) pyramid, (g) square pyramid, and (k) flower-shaped $SU8$ structures. (d,h,l) Optical image (top panels) of the patterned $MoS_2 - Au - SU8$ planar precursors and SEM image (bottom panels) of the assembled $MoS_2 - Au - SU8$ (d) pyramid, (h) square pyramid, and (l) flower-shaped photodetectors. Scale bars are $500\mu m$ for panels a, b, e, f, i, and j and $200\mu m$ for panels d, h, and l.

(water), the partially cross-linked porous top layer shrinks in order to minimize its contact with water, and the fully cross-linked bottom layer remains intact. The effect of exposing SU8 to water and the subsequent shrinkage was simulated by decreasing the equilibrium length constant of the fcc lattice in the top layer. Details of the model can be found in the SI. Snapshots of self-folded structures obtained using the coarse-grained model at different folding stages for pyramid, square pyramid, and flower, are shown in Figs. 6-2(c), (g) and (k), respectively. With the shrinkage of the top layer, the panels located around the center start to curve and eventually fold toward the center part. The final stage of the folding corresponds to a mismatch strain

$(1 - a/a0)$ of 0.15, which corresponds to a surface area shrinkage of 27.8%. We found that the bending stiffness difference between the top and bottom layer also affects the folding, and for a softer top layer the folding extent for a given mismatch strain decreases.

6.3   Photoresponse of MoS$_2$ Origami

When monolayer MoS$_2$ and Au patterns are integrated with the differentially photo-cross-linked SU8, a variety of selffolding photodetectors such as pyramid, square pyramid, and flower shapes can be generated Figs. 6-2(d), (h) and (l). We investigated the opto-electronic characteristics of the MoS$_2$ − Au − SU8 photodetectors by first measuring the photovoltage of the flat precursors. As shown in Fig. 6-3(a), we irradiated the flat precursor using a focused laser from the objective of a confocal laser scanning microscope and collected the electrical signals from copper wires bonded to the Au pads. We spatially scanned the laser position along the direction perpendicular to the electrodes (Y-direction) and observed a large photovoltage when the laser was positioned over the MoS$_2$ − Au regions, reaching a maximum at the first Au electrode and decreasing to zero when the laser spot was in between electrodes, then increasing to another maximum (opposite value) at the second electrode. This periodic pattern of vanishing and maximal photovoltage was repeatedly observed when the laser was moved over the MoS$_2$ − Au patterns along the Y-direction. We rationalize this observation by noting that the photovoltage generated is due to the combination of photovoltaic (PV) and photothermoelectric (PTE) effects [195]. In principle, both PV and PTE effects are related and associated with the injection of hot carriers across the potential barrier on the MoS$_2$ − Au interface. When photons get absorbed in the metal and its junction with MoS$_2$, electron-hole pairs are excited. When one of the carriers (usually the electron) get injected into the MoS$_2$ and then diffuses in the lateral direction, a photovoltage is generated. On the other hand, when the photoexcited hot electron
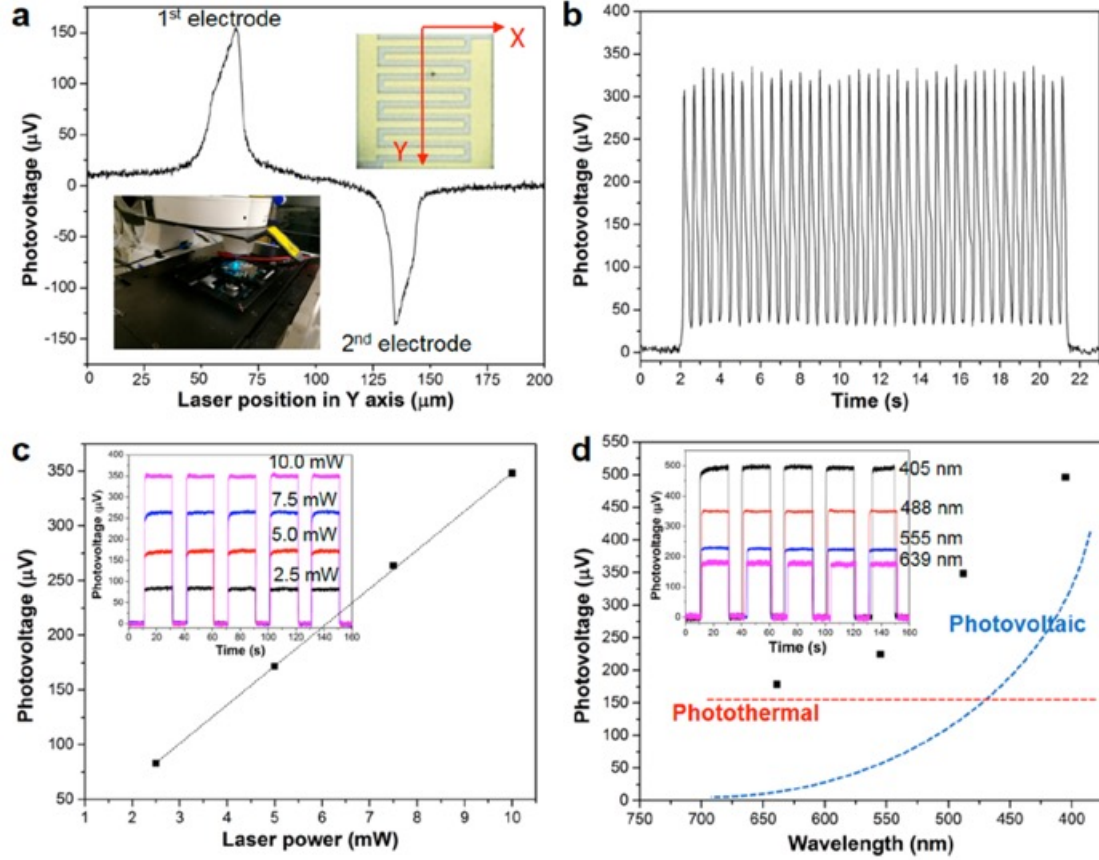
Figure 6-3. Photoresponse of the $MoS_2 - Au - SU8$ structures. (a) Plot of the photovoltage as a function of the relative position of the laser spot as it is scanned across the Y-axis of the flat $MoS_2 - Au - SU8$ photodetector. The insets show optical images of the device (top right), and the experimental setup used for photoresponse measurement (bottom left). (b) Plot of the time-resolved photovoltage when illuminated with a $488nm$ laser at $10mW$ at intervals of $500ms$ (2 Hz). (c) Plot of the photovoltage measured from the $MoS_2 - Au - SU8$ structure under$488nm$ illumination as a function of laser power. (d) Plot of the photovoltage measured from the $MoS_2 - Au - SU8$ structure under illumination with lasers of different wavelength at a constant power of $10mW$. The dashed lines represent the independence of the photothermal and quadratic functional dependence of the photovoltaic contributions to the photovoltage as a function of wavelength.

shares its energy with other electrons following rapid electron-electron scattering processes, these hot carriers undergo thermal diffusion leading to the establishment of photothermal voltage [195]. In addition to the photovoltaic response, the detector can also be operated under bias, that is, in a photoconductive mode. The I-V curves measured from the $MoS_2 - Au$ patterns are linear and symmetric for all the bias voltages, indicating an ohmic-like contact, and the current increases as the device is

illuminated. The current also increases with bias voltage due to the increase in carrier drift velocity and related reduction of the carrier transit time.

We studied the photoresponse dynamics of the $MoS_2 - Au$ patterns by measuring the rise and fall time under illumination of a modulated light source that could be switched on and off. We utilized a modulated laser with wavelength of 488nm and2Hz frequency for those experiments. The steep rise and fall edges suggest a reasonably fast response speed (Fig. 6-3(b)). We characterized the speed of the photodetector by calculating the rise time (Tr, the time interval from 10% to 90% of the maximum photovoltage) and the fall time (Tf, the time interval from 90% to 10% of the maximum photovoltage) of its response to an impulse light signal. The $MoS_2 - Au - SU8$ photodetector shows a Tr of 60ms, and a Tf of 86ms. The photoresponse speed is lower than that of similar devices fabricated on rigid substrates such as SiO_2 due to the large number of surface traps and the rough SU8 surface [196]. The response speed can be further increased by encapsulating the MoS_2 with a high-K dielectric layer such as Al_2O_3 [184].

To study the dependence of the photovoltage on laser power, we varied the 488nm laser power from 2.5 to 10.0mW, and the results are shown in Fig. 6-3(c). It can be seen that the photovoltage has a linear dependence on the laser power, and the average value increases from $83\mu V$ at 2.5mW to $348\mu V$ at 10.0mW. Increasing illumination levels results in enhanced photovoltage and photocurrent due to electron-hole pair generation by the light absorption in the Au and MoS_2. We observed that the photovoltage generated is broad in the visible spectral range, and also dependent on the laser wavelength. As shown in Fig. 6-3(d) in which lasers with four different wavelengths (405, 488, 555, and 639nm) with the same laser power (10mW) are used, the generated photovoltage is highest at 405nm and lowest at 639nm. As shown by the theoretical curves for PV and PTE indicated by dashed lines, the wavelength dependence can indeed be interpreted as the sum of two effects, a relatively weak PTE

voltage and a stronger PV response with the threshold around 650nm corresponding to the barrier height of about 1.9eV [197].

Apart from the hingeless self-folding shapes shown in Fig. 6-2, more complicated self-folding requires the incorporation of hinges interspersed by rigid panels. Also, in order to use the $MoS_2-Au-SU8$ photodetectors for spatially resolved photodetection, multiple MoS_2-Au patterns need to be defined. Both features are illustrated in the self-folded cubic and dodecahedron $MoS_2-Au-SU8$ photodetectors with interdigitated electrodes on each individual face (Figs. 6-4(a) and (b)). In order to study the effect of 3D geometry on the optical properties of MoS_2, we performed the finite-difference time-domain (FDTD) simulation on flat and cubic MoS_2 nanostructures (Fig. 6-4(c)). The absorption of a 2D monolayer MoS_2 with infinite size was first calculated, and the result agrees well with previous reports [198, 199]. Next, we simulated the optical absorption of an array of 3D MoS_2 cubes and 2D cruciform MoS_2 precursors with the same edge length of 100 nm. We observed that the 2D cruciform MoS_2 array has reduced optical absorption due to the reduced interaction area with the electromagnetic field. Importantly, after folding into a cubic shape the optical absorption is significantly enhanced as compared to the planar MoS_2 with three major broad bands at around 434, 614, and 662 nm. There are several reasons for this enhanced optical absorption. First, the electromagnetic wave interacts with multiple layers of MoS_2 in the cube as compared to a single planar layer for the 2D MoS_2. Second, we observed strong coupling of the electric field at the boundaries and corners of MoS_2 cubes, which also leads to stronger energy absorption. We also found that the size and spacing of the MoS_2 cubes have strong effects on their optical properties. Essentially, when the edge length of the cubes increases from 100 to 2000nm (Fig. 6-4(d)), the optical absorption gradually increases, except for the decrease in absorption in the $400-500$nm range for the 2000nm cubes. We rationalize this decrease by noting the edge length of the MoS_2 cubes increases to above the incident light wavelength, and there is strong
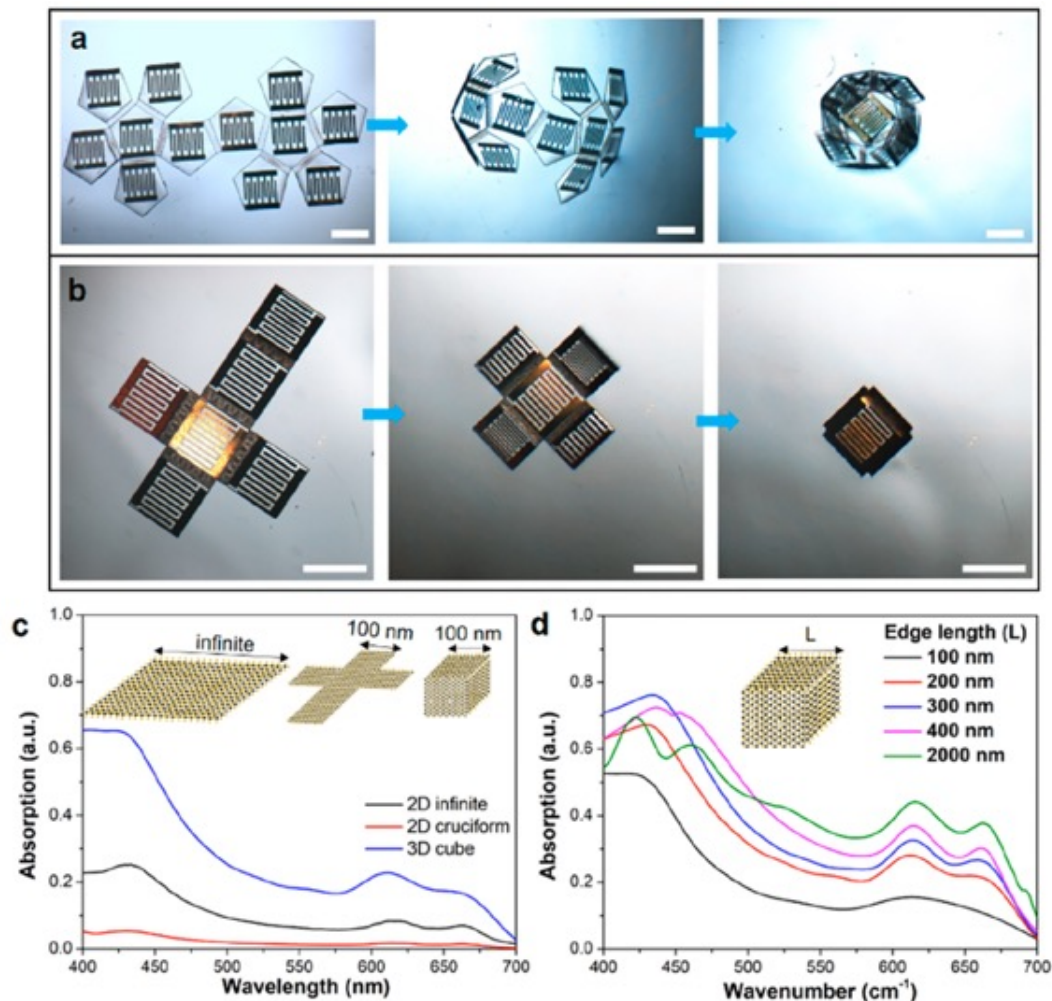
Figure 6-4. Hinged 3D $MoS_2 - Au - SU8$ photodetectors with interdigitated electrodes and FDTD simulations of 2D and 3D MoS_2. (a,b) Self-folding process of, (a) a hinged dodecahedron, and (b) a hinged cube-shaped $MoS_2 - Au - SU8$ photodetector from their 2D precursors. Scale bars are 1 mm. (c) FDTD simulated absorption spectra of 2D MoS_2 with infinite size, 2D cruciform MoS_2, and 3D cubic MoS_2. (d) FDTD-simulated optical absorption spectra of arrays of MoS_2 cubes with different edge lengths.

Fabry-Perot resonance between the top and bottom faces of the MoS_2 cubes which leads to stronger reflection and weaker absorption (Figure S18). This phenomenon is more pronounced at the $400 - 500nm$ range where the conductivity of MoS_2 is high. Also, for MoS_2 cubes with the same size, the optical absorption is stronger when the spacing between the cubes gets smaller (for instance, from 400 to 25nm). The main reason is that with increasing cube size or decreasing spacing between the cubes, the

fill ratio is increased, the electric field coupling at the boundaries is also enhanced, and both contribute to the higher energy absorption. The FDTD simulations suggest that such origami-inspired approaches could be used across length scales, and future experiments using electron-beam patterning at sub-100 nm line widths would further augment the present study. The 3D $MoS_2 - Au - SU8$ photodetectors also enable spatial and angle-resolved photodetection in all three dimensions. In comparison with conventional 2D photodetectors, which only collect light at limited incident angles (Fig. 6-5(a)), a 3D photodetector can have multiple electrodes arranged in a 3D fashion and collect light at a wider range of incident angles. In fact, there are major efforts to create 3D optical imagers inspired by the human eye for angular and efficient light detection and imaging [174, 175]. We performed photovoltage measurements using three different shapes of 3D $MoS_2 - Au - SU8$ photodetector (Fig. 6-5(b)), with the laser beam (488nm) irradiated in parallel to the basal plane. Additional details of the experimental setup can be found in the SI. For all the $MoS_2 - Au - SU8$ structures, multiple equally spaced electrodes were placed, one at each folded panel so that photovoltage would be generated only when the laser beam was incident at those angles or locations (Fig. 6-5(c)). We chose one of the electrodes as the reference position (zero degree to the center), then successively measured the photovoltage between the reference electrode and all the other electrodes in a counterclockwise manner, while recording the rotating angle of the device in reference to the incident light. For the pyramid-shaped $MoS_2 - Au - SU8$, the angle-resolved photovoltage was detected at 0°, 120°, and 240°. Similarly, for the square pyramid $MoS_2 - Au - SU8$, the angle-resolved photovoltage was detected at 0°, 90°, 180°, and 270°. For the sixpetal flower-shaped $MoS_2 - Au - SU8$, the angle-resolved photovoltage was detected at 0°, 60°, 120°, 180°, 240°, and 300°. We note that the bending which occurs during self-folding can induce some elastic strain in the MoS_2, which can lead to band gap modulation [200, 201] with associated changes in the photoresponse [202] of the 3D
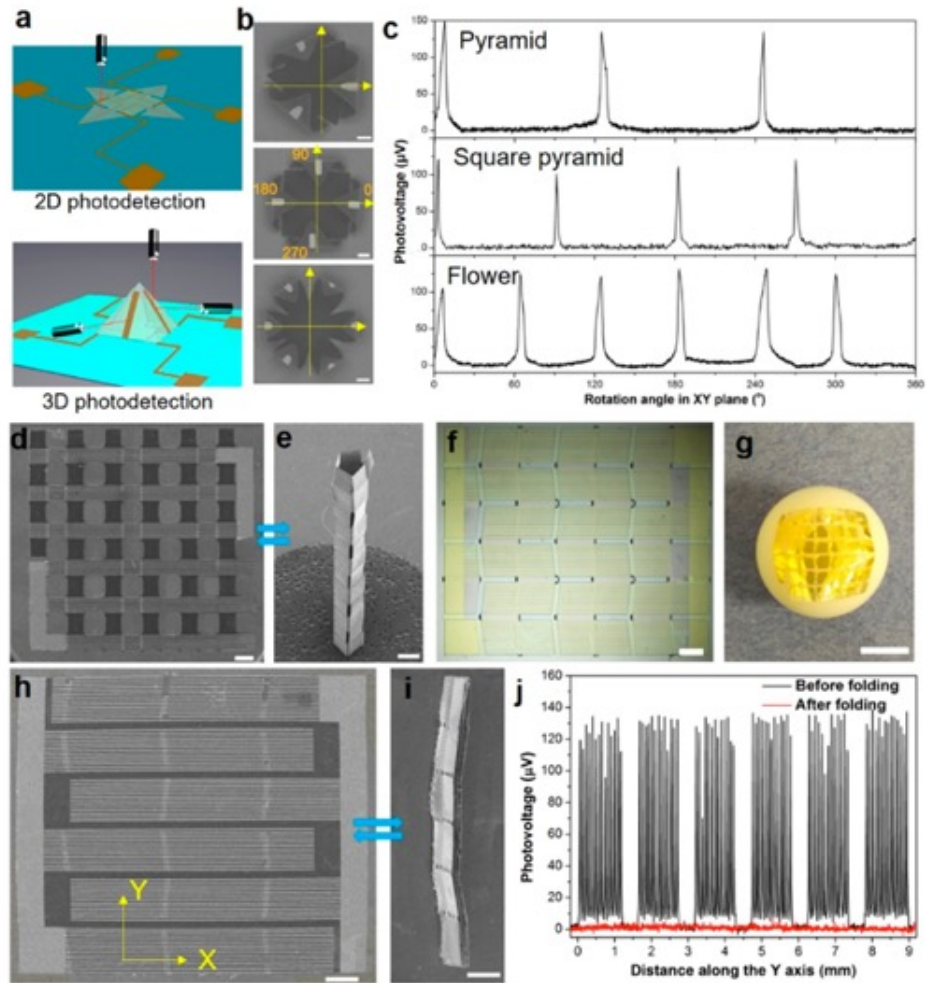
Figure 6-5. Spatially resolved and reconfigurable photoresponse of self-folded 3D $MoS_2 - Au - SU8$. (a) Schematic illustration of angle-resolved photodetection capability of the self-folded square pyramid shaped $MoS_2 - Au - SU8$ photodetector as compared to its 2D counterpart. (b,c) SEM images and angular-dependent photovoltage response of the self-folded pyramid, square pyramid, and flower-shaped 3D $MoS_2 - SU8$ photodetectors. (d,e) Self-folding transformation of a flat $MoS_2 - Au - SU8$ photodetector into a compact tower with vastly different spatial arrangement of its functional components. (f) Optical microscope image of a rectangular $MoS_2 - Au - SU8$ photodetector with Miura-ori pattern consisting of rigid panels and bidirectionally folding hinges. (g) Conformal wrapping of the flexible $MoS_2 - Au - SU8$ photodetector on a sphere. (h,i) Reversible Miura folding of the 2D $MoS_2 - Au - SU8$ photodetector from flat to a compact multilayered geometry with vastly different spatial arrangement and significantly reduced detection area in the XY plane. (j) The photovoltage measured from the rectangle $MoS_2 - Au - SU8$ photodetector before (black line) and after (red line) Miura folding, when the laser is scanned along the $Y - $ axis. All scale bars are $1mm$.

119

$MoS_2 - Au - SU8$ at specific wavelengths as compared to its 2D counterpart. The self-folding of complex 3D structures that show stimuli responsive reversible folding and unfolding with vastly different optical detection areas is a significant advance in this work. In order to illustrate this concept, we reversibly reconfigured a 2D flat $MoS_2 - Au - SU8$ photodetector that changes shape into a 3D tower structure with unidirectional folding (Figs. 6-5(d) and (e)). Importantly, inspired by the Miura-ori [203], we were able to create a rectangular-shaped $MoS_2 - Au - SU8$ photodetector sheet with arrays of Au patterns in the horizontal direction (Fig. 6-5(f)). The photodetector is highly flexible and can conform to curved objects such as a sphere in analogy to the properties of contact lenses (Fig. 6-5(g)). The SU8 film is photopatterned such that it contains rigid panels and two types of folding hinges: one group folds upward while the other one folds downward. As a result, the flat rectangular $MoS_2 - Au - SU8$ photodetector can be transformed into a compact multilayer-folded shape with a dramatic reduction in light detection area, as shown in the SEM images (Figs. 6-5(h) and (i)). We measured the photovoltage from the Miura photodetector before and after folding (Fig. 6-5(j)), during which the laser was scanned along the Y-axis of the photodetector. Prior to folding, strong PV is generated when the laser illuminates the $MoS_2 - Au$ regions as expected. After folding, the Miura pattern folds into an ultracompact multilayer. Interestingly, the folding conceals the $MoS_2 - Au$ regions within the compact structure and the PV essentially vanishes. After unfolding in acetone, the PV is essentially recovered. This experiment highlights the dramatic tunability that can be achieved in reconfigurable and reversible $MoS_2 - Au - SU8$ photodetectors which is an important step toward realizing deployable and smart biomimetic opto-electronic devices. We note that as compared to other designs used in the paper, due to the large strain generated during the Miura folding and unfolding, a fraction of the electrodes was damaged or delaminated after multiple cycles of folding/unfolding.

6.4 Conclusions

In summary, we have demonstrated a general approach to reversibly fold high-quality monolayer MoS_2 into well-defined 3D structures and opto-electronic devices. Reversible selffolding is based on solvent-induced swelling and deswelling of a differentially photo-cross-linked polymer SU8. The energy for shape transformation is derived from the flow of the solvent in and out of the polymer and does not require any wires, tethers, or batteries. Differential photo-cross-linking enables bending with both positive, zero, and negative curvatures; consequently, we were able to realize both hingeless and bidirectionally hinged 3D structures. We demonstrated that a 3D photodetector based on the folded $MoS_2 - Au - SU8$ structure offers spatially resolved 3D photodetection capability, which is also tunable depending on the 3D distribution of the $MoS_2 - Au$ patterns. As compared to conventional flat 2D structures, simulations show that 3D MoS_2 structures such as nanometer-sized cubes offer significantly enhanced light-matter interaction, and strong coupling of electric field at the boundaries and corners. Furthermore, a dramatic reduction and recovery of the $MoS_2 - Au - SU8$ photodetection area can be achieved with a Miura-ori, which is an advantageous attribute for wearables, as well as portable, foldable, and smart, sensors and energy harvesting devices. We anticipate that this self-folding approach could also be used with other 2D materials. Also, its reliance on planar lithographically patterned precursors and SU8 photoresist suggests the possibility for facile integration with microelectromechanical systems, microfluidics, and complementary metal-oxide-semiconductor to realize even more complex origami-inspired 3D integrated and multifunctional devices.

Chapter 7

Wide Bandwidth, Nonmagnetic Linear Optical Isolators based on Frequency Conversion

7.1   Introduction

Nonreciprocal light propagation that breaks the time-reversal symmetry plays an important role in optical communication and computing. For example, optical isolators and circulator are used in laser protection, optical signal processing and instrumentation application. To break the reciprocity, optical isolation has been traditionally achieved through magneto-optical Faraday effect. However, for the fast-developing silicon integrated photonics, the traditional optical isolators and circulators are at disadvantage as are not compatible with complementary metal-oxide-semiconductor (CMOS) processing platforms.

To avoid the integration of magneto-optical elements and achieve more compact isolation, a variety of different physical principles have been proposed. Among these new principles, one of the most attractive and studied is based on the electro-optical effect. In electro-optic modulation velocities of RF and Optical waves are matched only in one direction, and this breaks reciprocity. However, modulated isolators usually suffer from a number of limitations, such as incomplete isolation, nonlinearity,

excessive insertion loss and narrow bandwidth, moreover, because the momentum mismatch inhibiting the backward transmission is very small, hence the achieved optical isolator is very long ($\sim$cm), which makes it harder for miniaturization. By considering the above drawbacks of electro-optical effect, we can resort to another widely used and relatively mature principle: nonlinear frequency conversion and four wave mixing (FWM) based on the second and third-order nonlinear susceptibilities, which can help us obtain wide bandwidth, linear optical isolators. In this work, two ideas have been developed to achieve full isolation over wide bandwidth of a few THz in the telecom range.

7.2 Wideband nonmagnetic linear optical isolator based on nonlinear frequency conversion and spectral filtering

Optical isolators and circulators are essential components for signal routing and blocking in applications such as lasers protection and stabilization and optical networks [204, 205]. Their functionality is fundamentally based on breaking time-reversal symmetry or Lorentz reciprocity described by symmetric scattering matrix [206–208]. Key features of an ideal optical isolator include broadband operation, linearity, low insertion loss and high isolation. Another crucial feature for modern integrated photonic applications is small footprint required for integration of isolators with other components. Guided-wave isolators have been realized for decades using the Faraday effect in magneto-optical materials [209–211], where the garnet serves as the optical guiding layer. Introducing thin layers of garnets, e.g., yttrium iron garnet (YIG), to standard semiconductor-based photonic integrated circuits (PICs) has been pursued more recently with reasonable success [212–214]. Still, fabrication challenges, high insertion loss, and polarization dependence present formidable obstacles that prevent integrated magnetic isolators from being widely adapted. Hence, alternative,

123

nonmagnetic optical isolator has been vigorously pursued by many groups.

Lorentz reciprocity holds for any linear, time-invariant and reciprocal systems with symmetric permittivity and permeability tensors or combination thereof. Thus, nonmagnetic optical nonreciprocity can be achieved through breaking either the linearity or time-invariance condition [206, 208], often accompanied by introducing optical loss and gain. This has been sought by a number of research groups through adopting different approaches. For example, nonlinear effects (both second-$\chi^{(2)}$ and third-order $\chi^{(3)}$ nonlinearity) have been in focus of works used [215–218]; however, these schemes have limited potential since their performance depends on input power or have limited operation bandwidth, and, furthermore, some of them are not even true isolators, as explained in [207]. Similarly, Recently, proposed a theoretical modeling of a non-reciprocal system based on a parity-time symmetric schemes has been reported [219]. The proposed scheme that incorporates ring resonators waveguides with alternating gain and loss regions in presence of Kerr nonlinearity are is clearly non-reciprocal, in the sense that they have different transmittance spectra for left-to-right and right-to-left incident signals, i.e $T_L(\lambda) \neq T_R(\lambda)$an incident signal in opposite directions. However However, in either direction, if the incident signal is back-reflected, the scheme is incapable of blocking the reflected signal.for signal propagating from right-to-left in the presence of its counter-propagating signal from left-to-right, both will have the same transmittance and no isolation will be achieved.

At the same time, true optical isolators based on time-varying modulation of material properties (usually refractive index) by traveling wave of RF frequency has been proposed and investigated in recent years. These include electro-optically induced indirect interband transition [220, 221], space-time modulation in photonic crystal waveguides [222], acousto-optic modulation [223, 224] as well as electro-optic (EO) modulation in commercial devices [225, 226], and more elaborate but conceptually similar work that involved synthetic angular momentum [227, 228]. These schemes

are truly isolating and linear, yet reliance on modulation at RF frequency leads to three deleterious effects. First of all, modulation at frequency of say 10 GHz limits the bandwidth of the signal to something less than that. Second, even if clever dispersion engineering can alleviate this problem, presence of strong RF power inevitably causes high noise in the signal band - it may be not important if the isolator just serves to isolate the laser source, but it is problematic if it is used further along the optical path where the weak signal will be difficult to discern in the presence of strong RF pump. Last, but not least, the working principle of all time-modulated schemes relies upon the fact that the processes that are momentum (phase) matched in one direction are mismatched in the other direction. For instance, if the refractive index is modulated by a wave with a frequency Ω and wavevector $K(\Omega)$, the efficient energy transfer between two forward propagating optical waves of frequencies ω_1 and $\omega_2 = \omega_1 - \Omega$ will be achieved when $k(\omega_1) = k(\omega_2) + K(\Omega)$ (i.e., when the group velocity of optical wave matches phase velocity of RF wave). For backward propagation, the momentum mismatch is then $\Delta k = 2K$, and the full isolation is attained if the length is chosen to be $L = \pi/K$. If the coupling wave is RF, the mismatch is relatively small (on the scale of cm^{-1}), hence a long length is required. And any small deviation of length will cause leakage. To avoid this issue, one may consider acousto-optic modulation [223, 224], where K is larger but then the bandwidth gets severely limited. All of these limitations, however, can be lifted once one realizes that in essence any time-dependent modulation scheme is a three-wave nonlinear parametric process, hence if instead of low frequency RF coupling wave one uses the wave of optical frequency, the bandwidth can be significantly expanded, no noise will enter the signal bandwidth, and, most important the momentum mismatch K will becomes so large that no meaningful coupling in the backward direction can occur leading to much higher and more robust isolating ratios.

This is precisely the idea behind this work, as we introduce a wholly new approach

based on nonlinear frequency conversion processes (e.g., difference-frequency generation (DFG)) and spectral filtering, to achieve nonmagnetic wideband and linear (in a sense of input vs. output characteristics) optical isolation. The scheme is compatible with integrated photonics platforms, i.e., it can be potentially monolithically integrated on a single chip with complex PICs. The operation principle of the new optical isolator is
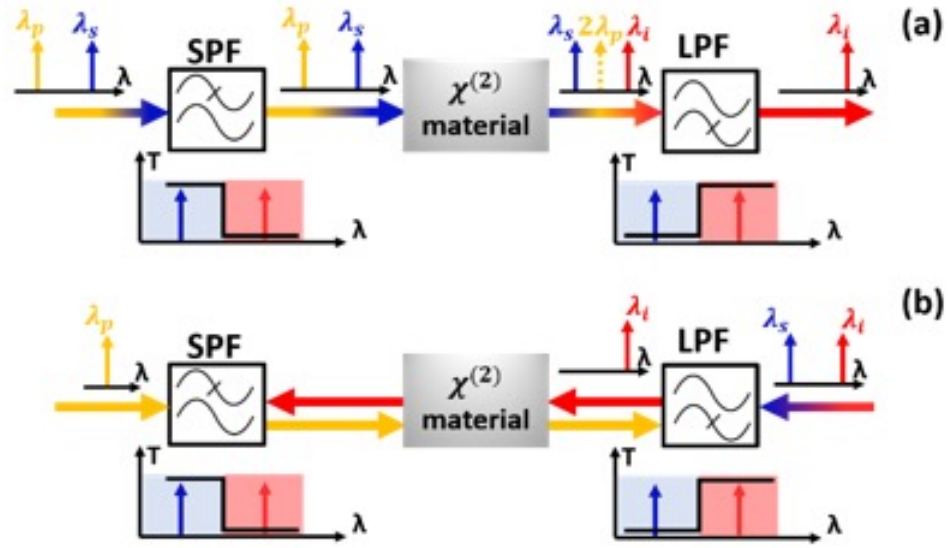
Figure 7-1. Schematic diagram of the proposed optical isolator, showing operation principle in (a) forward and (b) backward directions. SPF: short-pass filter, LPF: long-pass filter.

based on breaking Lorentz reciprocity in nonlinear waveguides. In essence, nonlinearity is one way to achieve asymmetric scattering matrix ($S^T \neq S$) and hence non-reciprocal operation [206]. To explain the proposed concept, first consider the signal, s, and pump, p, co-propagation in forward direction, shown in Fig. 7-1(a), with $\lambda_s < 2\lambda_p$. In this case, an idler wave can be generated at wavelength $\lambda_i = (\lambda_p^{-1} - \lambda_s^{-1})^{-1}$ through DFG, as long as the phase matching condition is satisfied. The shown long-pass filter (LPF) at the output allows only the transmission of the idler, which now contains all the information transferred from the signal and blocks all other involved wavelengths. In Fig. 7-1(b), the signal and/or idler are coupled in the backward direction. The signal is blocked by the LPF and only the idler can be transmitted. Since the pump

and idler are counter-propagating in this case, the phase matching condition is not satisfied, hence, given that the wavevector mismatch is large (coherence length is on the scale of optical wavelength), no signal is generated, and the idler wave is eventually absorbed by the short-pass filter (SPF).

The frequency shift from signal to idler inherent in this scheme should not present a problem in most optical links, but if it does, it can be remedied by converting the idler output back to the input signal wavelength through another DFG process. Alternatively, as we have proposed elsewhere, the frequency shift can be completely avoided as proposed by us in [229] if sum-frequency generation (SFG) instead of DFG is used instead of DFG [229]. However, such a scheme would require a highly efficient SFG process in a long waveguide to achieve sufficient signal depletion and hence good isolation. It should be also noted that combination of SFG and optical absorption can be used instead of filtering [230]. Again, long devices are needed to attain high conversion and efficient absorption. Also, adiabatic rate of the quasi-phase-matching period is another restriction imposed in this scheme, in order to avoid overdamping problem due to strong absorption [230].

It should be mentioned that second-order nonlinearity in PPLN has been exploited in the past to demonstrate optical isolation [215]. However, that scheme would only functions at high input signal powers (1.5 W at 1550 nm), behaving more like a power limiter and lacking linearity. While our isolator is also based on second-order nonlinearity, its input-output relation is linear and not power dependent. In an ideal case, $P_i = \eta P_s P_p L^2$, where η is the nonlinear conversion efficiency and L is the length of PPLN, thus the generated idler power is proportional to the input signal for a fixed pump power. Indeed, in our experiments the isolator works perfectly at low input pump powers of $\sim$ 3mW.

In our proof-of-concept demonstration, we use a periodically-poled thin-film lithium niobate (TFLN) waveguide as the $\chi^{(2)}$ nonlinear element, and combine it with external

spectral filters to achieve high isolation ratio. Details of the thin-film PPLN design and fabrication can be found in our previous work [231]. We have recently developed an actively-monitored iterative poling technique to optimize the periodic poling conditions and report record-high efficiencies of up to $4600\%\text{W}^{-1}\text{cm}^{-2}$ [231]. The TFLN platform has many unique properties and is a fairly recent ultracompact platform, on which a wide variety of integrated photonic components, such as highly efficient periodically-poled LN (PPLN) devices [231–234], high-speed optical modulators [235–237], cascaded nonlinear devices [238, 239], quantum photonics devices [240, 241] and acousto-optic devices [242, 243] have been demonstrated. An implementation of the proposed
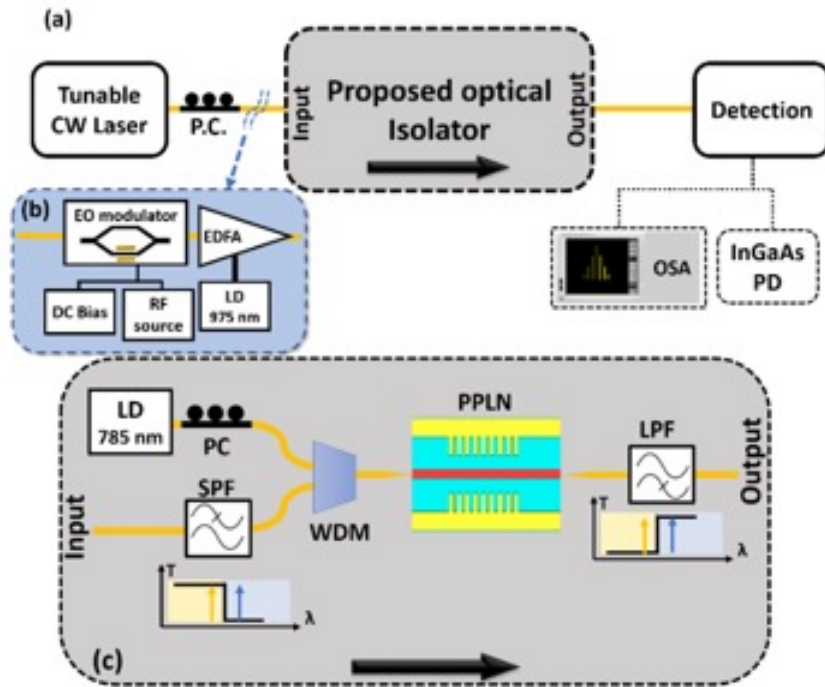
Figure 7-2. Experimental setup for the demonstrated optical isolator with (a) the general scheme for forward measurement, (b) the added components for input modulation and (c) the detailed schematics of optical isolator.

isolator system is depicted in Fig. 7-2. The thin-film PPLN waveguide is pumped using dual pump (pump-signal) to generate a DFG signal at the telecommunication band. The pump source is a diode laser at 785nm wavelength, which is tunable over few nanometers. The signal source is a continuous-wave (CW) laser that can be tuned

128

from 1490nm to 1640nm. Inline polarization controllers (PCs) are used to adjust the pump and signal polarizations for transverse-electric (TE) mode excitation into the waveguide. This guarantees utilizing the highest nonlinear coefficient of X-cut lithium niobate ($d_{33} = 30$pm/V).

The signal is first filtered by a mechanically tunable short-pass filter with a rolling-off slope of 20 dB/nm and a tuning range of 1490 nm to 1610 nm. Then, it gets multiplexed with the pump through a wavelength-division multiplexer (WDM). The WDM output is coupled into the thin-film PPLN waveguide using an anti-reflection (AR) coated lensed fiber. The output from the waveguide is also coupled using a similar lensed fiber and then filtered using a mechanically tunable long-pass filter with similar specifications. The output is characterized using either an InGaAs detector at 1550 nm wavelength range or an optical spectrum analyzer (OSA).

Prior to the isolation experiments, we have characterized the PPLN waveguide by measuring SHG and achieve nonlinear conversion efficiency of 95%W^{-1} in 4-mm-long PPLN regions out of 1-cm-long waveguides. This length can be significantly reduced without affecting the whole system performance through using shorter PPLN devices with better poling uniformity and, hence, higher normalized efficiency. The measured phase matching characteristics is shown in Fig. 7-3 with a phase matching peak around $2\lambda_\mathrm{p} = 1570$nm. The observed deviation from an ideal sinc^2 function is attributed to statistical variation of fabrication parameters and poling nonuniformities over long lengths. This nonideality may be alleviated by adopting techniques described in [244, 245].

The experimental setup for characterizing the isolator is shown in Fig. 7-2(a). We first start with measuring the DFG signal. A wide tuning range of the DFG, extending from 1505 to 1646 nm, is attained, as summarized in Figs. 7-2(a) and (b) and limited by the available tuning range of the CW signal laser. Then, the output signal is measured after the LPF demonstrating the forward propagation case, as shown in

Fig. 7-4(c). Evidently, the signal and pump waves are completely blocked and only the idler is transmitted with power level more than -50 dBm, carrying all the signal wave spectral information, as desired. The signal wavelength is tuned from 1550 nm to 1565 nm resulting in an idler wavelength tuned from 1575 nm to 1590 nm with a consistent power level. The overall insertion loss at the signal and idler wavelengths is ~14 dB. However, only ~1 dB is attributed to the 1-cm TFLN device. The other 13 dB is due to coupling loss into the chip (~3.7 dB per facet) and insertion losses of the WDM component (3 dB) and the two filters (1.3 dB, each), both of which can be reduced or eliminated in a fully-integrated system.
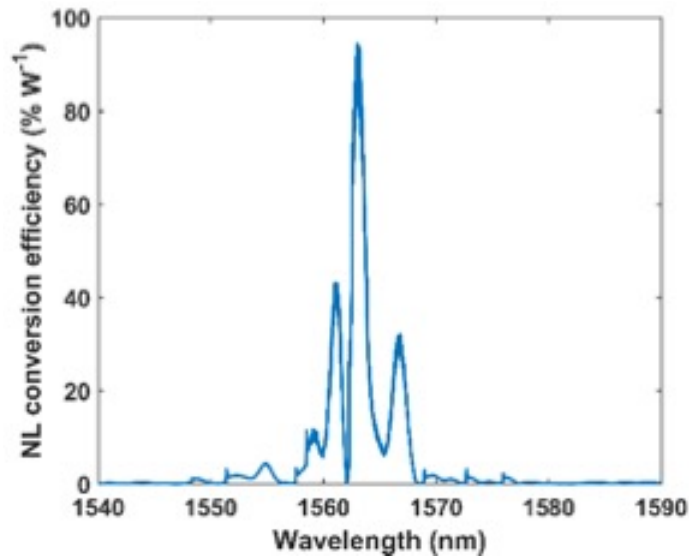
Figure 7-3. Measured SHG efficiency versus pump wavelength shows a peak conversion efficiency of $95\%/W$ around 1570 nm.

Shown in Fig. 7-4(d) is, backward-propagating signals below $2\lambda_p = 1570$nm are completely blocked by the LPF, as far as the noise floor of the employed OSA (-75 dBm) suggests. This implies that an optical isolationa difference of 40 dB is achievedbetween the forward- and backward-propagationng transmittance at λ_s.

The isolation of the present isolator depends mainly on the filters' extinction ratios, nonlinear conversion efficiency, as well as any back-reflections of the involved pump, signal and idler waves. However, iImagine a signal above 1570 nm is coupled
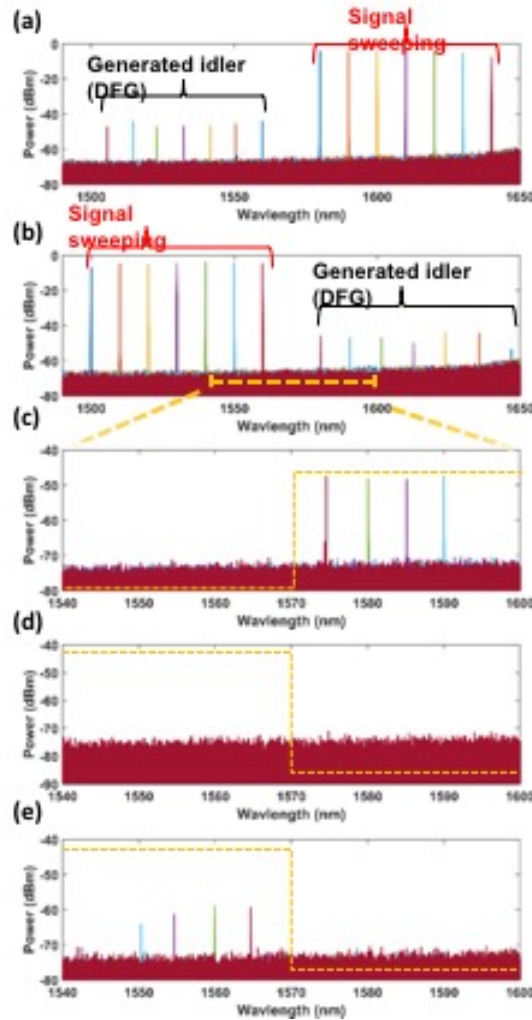
Figure 7-4. Characterization results of the proposed isolator: Generated idler (DFG) measured before LPF with signal tuned from (a) 1570 nm to 1640 nm and (b) 1500 nm to 1560 nm. Measured Isolator output in (c) forward direction, (d) backward direction with tuned signal from 1550 nm to 1565 nm and (e) backward direction with idler coupled back and tuned from 1575 to 1590 nm. Dotted yellow lines represents the LPF and SPF transmission windows.

in the isolator in backward direction. This can be the case if the forward-generated idler is back-reflected into the system. Such a signal is transmitted through the LPF. Although the phase-matching condition is not satisfied between this signal and the forward pump, as explained earlier, an output signal below 1570 nm with 13-18 dB less power than the forward case is evident in Fig. 7-4(e). In other words, the measured isolation is 13 to 18 dB in this case, which is superior to most prior results obtained

with time-varying schemes [221, 222, 224, 226]. Isolations of 30 dB (at 2 GHz) and 14 dB (at 10 GHz), have been reposted on an approach based on RF modulation [225]. However, as mentioned before, that approach suffers from inherently limited bandwidth and requires fine tuning.

The backward-propagating signal in the latter case is most likely generated through the DFG process between the backward propagating idler and back-reflected pump from the PPLN devices' polished facet and any other reflections from other components and fibers. The backward propagating pump power inside the PPLN is estimated to be one order of magnitude less than the forward propagating pump based on the facets reflectivity and insertion loss at pump wavelength. This back-reflected pump and backward-coupled signal waves hence co-propagate in the backward direction and satisfy the phase matching condition, resulting in a relatively efficient DFG process. Then, the generated signal could pass through the SPF at the output, tuned to block waves above 1570 nm, and get detected by the OSA, hence an isolation of 13-18 dB. This backward generated signal can, nonetheless be significantly reduced or eliminated by applying appropriately-designed anti-reflection (AR) coatings to the PPLN facets and other system components to eliminate all back-reflections. The estimated isolation after AR coating is 40 dB, i.e., on par with the first case explained above.

For the sake of demonstrating applicability to optical communication systems, we examined the performance of our isolator when using RF-modulated optical signals. The RF modulation setup is shown in Fig. 7-2(b), in which an external RF commercial EO intensity modulator operating up to 13 GHz is employed. The modulating RF signal is generated by a network analyzer and amplified by an RF amplifier. The modulator is also DC-biased for maximum sensitivity. The output from the modulator is amplified using an Erbium-doped fiber amplifier (EDFA) to compensate for the insertion loss of the modulator. The laser signal, tuned from 1550 nm to 1565 nm, is first modulated with 5 GHz RF signal and coupled into the isolator. Figure 7-5(a)
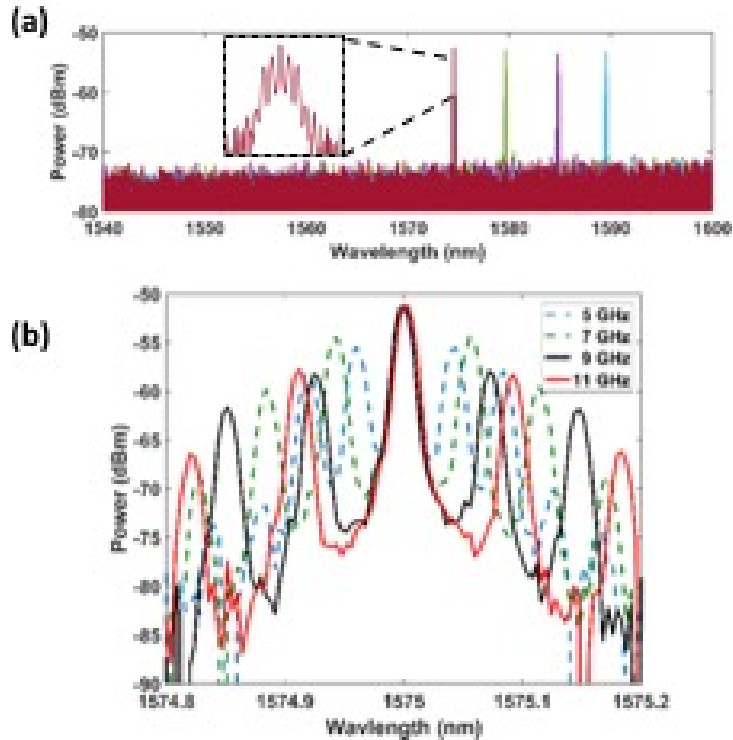
Figure 7-5. Isolator output with RF modulated input signal at (a) fixed RF speed of 5 GHz and tuned optical signal (1550 to 1565 nm) and (b) tuned RF signal (5 to 11 GHz) and fixed input signal at 1565 nm.

shows the isolator output in forward direction. The generated idler clearly carries all the information from the input signal represented by the modulation sidebands, shown in the zoomed output in the inset. The output power is a little bit lower than the unmodulated case due to the added sources of losses in the system, but still consistent over the tuning range. The input signal is then kept fixed at 1565 nm and the RF frequency is tuned from 5 to 11 GHz and the output at 1575 nm is recorded for each frequency, as reported in Fig. 7-5(b). This result demonstrates the isolator compatibility for high-speed communication, limited here only by the employed modulator bandwidth.

Before concluding we briefly outline the means by which the performance of the demonstrated isolator can be improved. The isolation ratio can be greatly improved by incorporating AR coatings and superior filters, The insertion loss can be reduced by

improving coupling and eventually integrating all the component and the conversion efficiency can be enhanced substantially if the pump instead of being lost at the output LPF can be rerouted back to the rear facet of the pump laser so the DFG can take place inside the ring pump laser cavity. It should be noted that this scheme is, in principle, a parametric amplifier. Hence, if the insertion loss is reduced significantly and efficiency is enhanced, the isolator can operate with gain rather than loss. It must be also mentioned that the proposed signal-to-idler isolation scheme is not limited to $\chi^{(2)}$ nonlinearity, as third-order nonlinear ($\chi^{(3)}$) processes, such as four-wave mixing (FWM), can be alternatively considered.

To summarize, we have proposed a novel class of nonmagnetic wideband linear optical isolators based on frequency conversion in nonlinear waveguides. We have demonstrated and characterized the performance of the proposed isolator using DFG in thin-film PPLN devices. The operational range of the isolator has extended from 1490 nm to 1640 nm, limited only by the bandwidth of the used equipment, and the isolation of up to 18 dB is measured for the idler and signal waves. The difference between forward- and backward-propagation transmittances at the signal wavelength is 40 dB. The isolator has demonstrated linearity and has shown no performance degradation with signals of up to 11 GHz in bandwidth making it an attractive candidate for fully integrated photonics circuits.

7.3 Optical Isolators Based on Mode Conversion in Waveguides with Adiabatic Couplers

In the previous section, we successfully achieve a non-magnetic linear optical isolation based on non-linear frequency conversion and spectral filters. However, because the signal and idler wave are always coexisted, spectral filters are necessary at the input and output which makes the whole optical isolator costy and bulky. Hence, if we can separate the signal and idler wave at the output, then we can get rid of the spectral

filters. Based on the waveguide coupler theory, if the signal and idler are orthogonal modes in waveguide coupler, they can be separated by coupling to different waveguide coupler arms. In this section, I design the filter-free optical isolators based on the conventional symmetric waveguide coupler and adiabatic waveguide coupler.

Both the symmetric and adiabatic waveguide coupler are widely used to coupling or splitting light into different waveguides. The coupling length of symmetric waveguide coupler is extremely sensitive to wavelength and fabrication imperfections which make it difficult to achieve the desired coupling ratio and the exact beat length. Asymmetric adiabatic couplers have been developed to overcome these drawbacks. Adiabatic couplers work by adiabatically converting the mode of a single waveguide into either the even or odd mode of two identical waveguides separated by a small gap. Adiabatic couplers do not require precisely defined power-transfer length. In addition, they have small wavelength and fabrication variation dependence but with a trade-off of longer coupling lengths than directional couplers. Figure 7-6 is a brief schematic of the adiabatic waveguide coupler. Usually it consists of two asymmetric waveguides or linear tapers, separated by a gap. Figure 7-7(a) shows the geometric structure of the
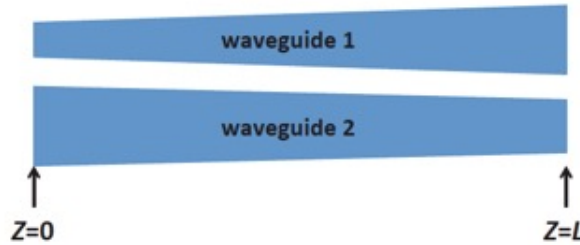
Figure 7-6. Schematic of adiabatic waveguide coupler consists of two asymmetric waveguides.

filter-free optical isolator. The middle symmetric wavegudie coupler, whose two arms have the same cross-section $1.5 \times 1.5 \mu m^2$ and length L_d, is symmetrically sandwiched by two adiabatic waveguide couplers, the length of the adiabatic waveguide couplers is L_a, the cross-section of the narrow core is $2 \times 2 \mu m^2$ at the input and output, and then
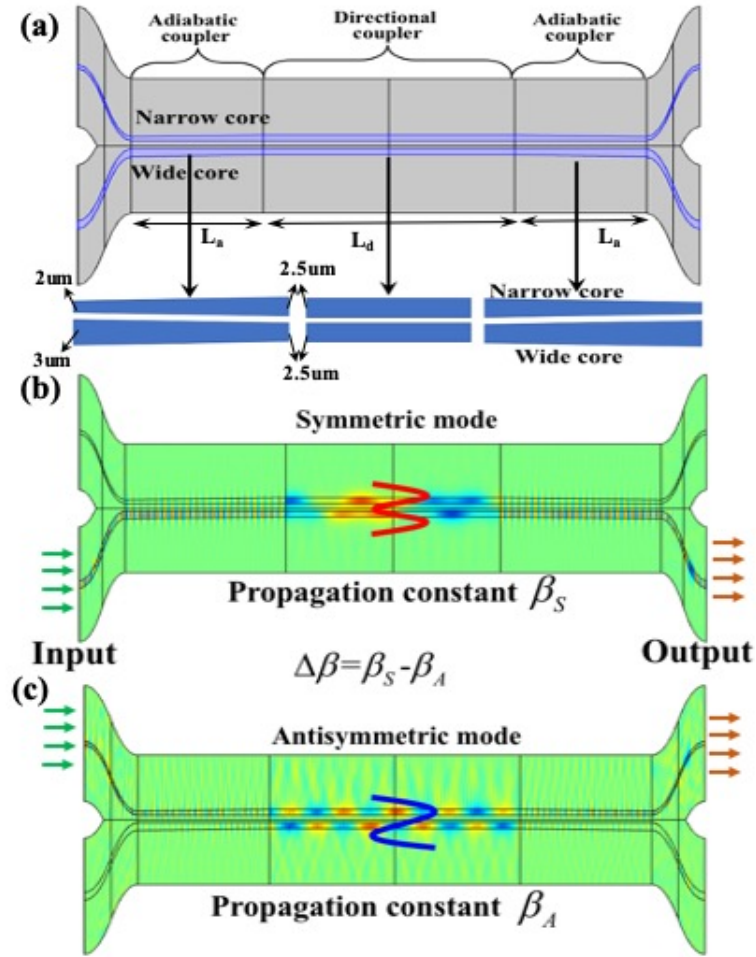
Figure 7-7. (a) is the schematic of filter-free optical isolator; (b) and (c) are the Comsol simulation results when the signal is input form different coupler arms.

linearly increases to $2.5 \times 2.5 \mu m^2$ at the connection to the middle symmetric waveguide coupler, the cross-section of the wide core is $3 \times 3\mu m^2$ at the input and output and then linearly decrease to $2.5 \times 2.5\mu m^2$ at the connection to the middle symmetric waveguide coupler. The radius of the bend waveguides at the input and out have been optimized using parameter sweeping. The gap between the two arms of middle symmetric waveguides is 2.5μm. Figures 7-7(b) and (c) show the different propagation modes inside the waveguide couplers based on different exciting conditions. As shown in Fig. 7-7(b), when the signal is input from the wide arm, a symmetric mode with propagation constant β_s is excited in the middle symmetric directional wavegudie

136

coupler, after the directional waveguide coupler, the symmetric mode couples back to the wide arm and output from the wide arm. Similarly, When a signal is input from the narrow arm, a antisymmetric mode with propagation constant β_{a} is excited in the middle symmetric waveguide coupler, after the directional waveguide coupler, the antisymmetric mode couples back and output from the narrow arm, as shown in Fig. 7-7. In the middle symmetric waveguide coupler, if we take some strategy to achieve the mode conversion, we can probably realise the nonreciprocal propagation. For example, for the symmetric mode excited by inputting the signal from wide arm, if we can make it convert to antisymmetric mode at the end of middle symmetric waveguide coupler, then the antisymmetric mode would couple to the narrow arm instead of wide arm. For the backward operation, when the signal is reflected back to the narrow arm, in the middle symmetric waveguide coupler, the mode conversion condition is not satisfied, and finally it will outcome from narrow arm. Several mechanisms can be employed to achieve the mode conversion, such as electro-optical effect, acoustic-optical effect and nonlinear optics. The following are two optical isolators achieved, and the mode conversion in the first one is realized using electro-optical effect and in the second one using difference frequency generation (DFG).

7.3.1 Optical Isolator Based on Electro-Optical Mode Conversion

To realize the mode conversion inside waveguide coupler, it is necessary to compensate the propagation constants difference. We slightly modulate the refraction index of the symmetric waveguide coupler. One of the most commonly used method is the application of electric field, just as people did to achieve modulators. As shown in Fig. 7-9 electrodes are deposited on the top and bottom of the symmetric waveguide coupler. The waveguide design assures momentum matching, i.e $\delta\beta = \beta_{\mathrm{s}} - \beta_{\mathrm{a}} - \beta_{\mathrm{RF}} = 0$. There are several electro-optical materials such as $LiNbO_3$, GaAs and $LiTaO_3$, in this work

we use LiNbO$_3$, and it electro-optical coefficient is about $\gamma_{13} = 8$pm/V at wavelength 1.55μm [246]. The index of core is $n_c = 2.22$ and the index of cladding is $n_d = 2.2$. Figure 7-8 is the evolution of symmetric and antisymmetric modes propagation constant with input wavelength when there is no applied voltage. We can see from Fig. 7-8, at the wavelength 1.55μm, the propagation constants difference Δk is $9.7753 \times 10^3 \text{m}^{-1}$, then for a modulation frequency $\omega_{\text{RF}} = 20$GHz, to compensate the propagation difference, the modification of index should be $\Delta n = \omega_{\text{RF}}/(\Delta kc) = 6.82 \times 10^{-3}$, where c is the light speed in vacuum, then the electric potential E_p needed can be calculated through $\Delta n = \frac{1}{2} n_c^3 \gamma_{13} E_p$. The total cross-section, of the waveguide is $2.5 \times 2.5 \mu m^2$, hence the amplitude of the voltage needed to apply on the waveguide during the simulation is $V_p = (E_p \times 2.5 \times 10^{-6}) = 400$V, then the modulation voltage is $V = V_p \cos(\omega_{\text{RF}} t)$.

Fig. 7-10 shows the performance of optical isolator based on the electro-optical effect, we can see that the energy from the signal symmetric mode moves to the idler antisymmetric mode inside the middle symmetric waveguide coupler. To achieve full isolation, we need to choose the length of the middle symmetric waveguide coupler, according to Fig. 7-10(a) the length is about 2.65cm with the electric modulation frequency $\omega_{\text{RF}} = 20$GHz.

For the backward operation, due to the uncompensable propagation constant difference $\delta\beta = \beta_s - \beta_a + \beta_{\text{RF}} = 2\beta_{\text{RF}}$, when the idler wave is input or reflected back to the narrow arm of rare adiabatic waveguide coupler, the mode is always antisymmetric inside the middle symmetric waveguide coupler, and finally it outputs from the narrow arm of the front adiabatic waveguide coupler. Hence, by using the electric modulation, we successfully achieved the mode conversion and nonreciprocal transmission. It is linear and power efficient. However, due to the small electric modulation frequency, when it operates backward, the propagation constant difference is much smaller than the first isolator we proposed and demonstrated in section 7.2. Hence, if either length
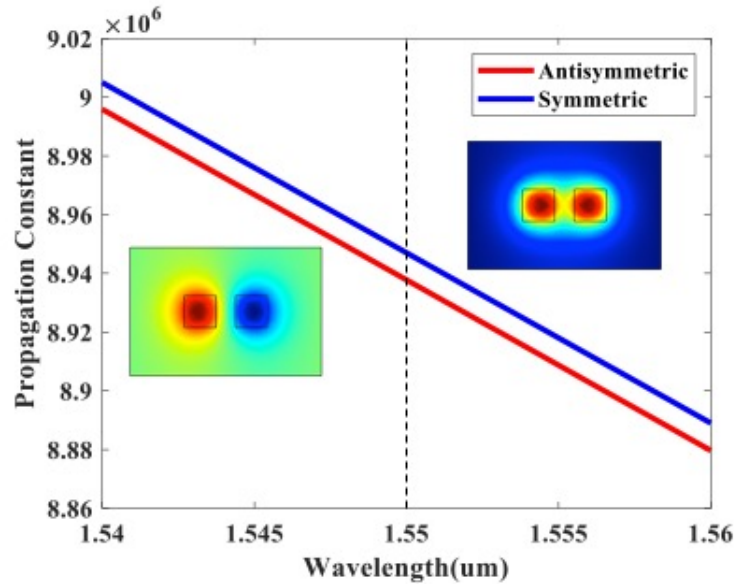
Figure 7-8. Changes of propagation constant of symmetric and antisymmetric mode with wavelength.
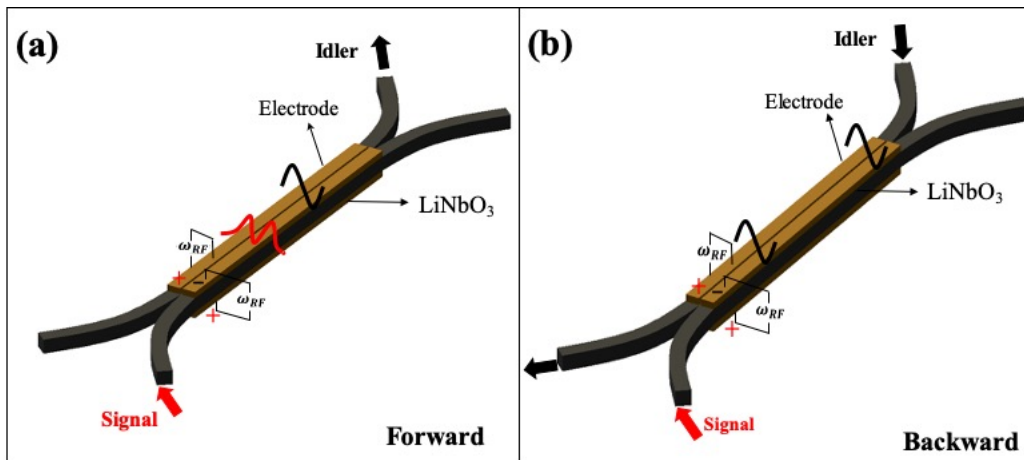
Figure 7-9. The forward and backward operation of the second optical isolator.

or voltage slightly deviates, the isolation is not a full isolation, as shown in Fig . 7-10(b), the energy can still transfer back and forth between the symmetric and antisymmetric modes. Then, to realize full isolation, we much carefully choose the waveguide coupler length and other parameters such as the modulation frequency, in order to let the maximum forward energy transfer and the minimum backward energy transfer overlap, as shown in Fig. 7-11(a). Figure 7-11 shows the effect of modulation power on the performance of isolation. We can see that, suppose we have selected the

139

Figure 7-10. (a) and (b) are the forward and backward performance of the optical isolator when electric modulation is used to match the phase mismatch.

proper waveguide length and modulation power for full isolation, then by changing the modulation power at the original signal input for forward operation, the output power shows up and keeps increasing due to the imperfect isolation. Hence, it desirable to combine adiabatic mode conversion with difference frequency generation to achieve a good isolation without retorting to high finesse filtering.
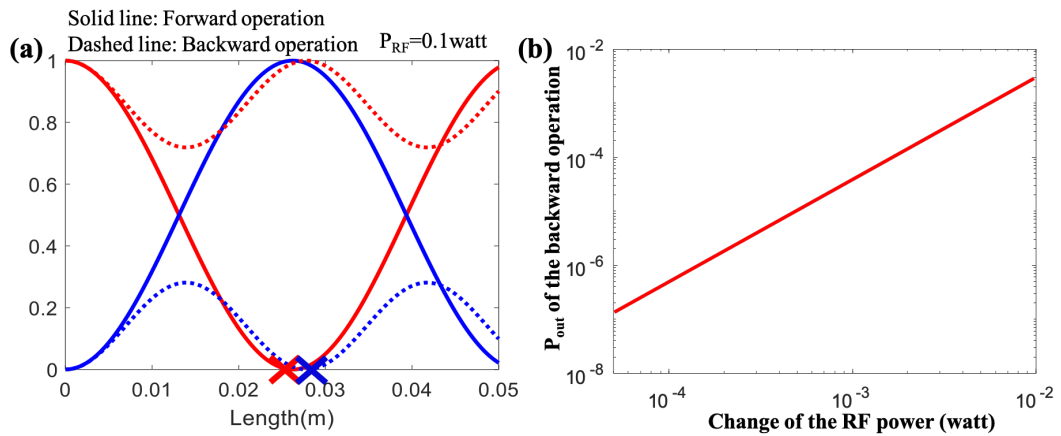
Figure 7-11. (a) To reach full isolation the maximum forward transfer must overlap the minimum backward transfer; (b) Change of the output power with modulation power at forward input when the isolator operates backward.

7.3.2 Optical Isolator based on Non-linear Optical Conversion

By using the waveguide couplers and electro-optical effect, we have successfully achieved the mode conversion and optical isolation without using the filter. However, as we can see, for the backward operation, the energy from the reflected wave can still couple to the original input, it can only be avoided by carefully choosing the precise waveguide length. But by considering the fabrication error, it very difficult to reach it. Hence, to reach a stable optical isolation, we tried another mode conversion strategy-nonlinear optical effect. Here to compensate the propagation constant difference and achieve mode conversion, we utilize the periodically poled $LiNbO_3$ (PPLN), which is widely using in nonlinear optics to eliminate phase mismatch, in arms of the directional waveguide coupler. By doing this the propagation constant difference can be compensated, hence in the directional waveguide coupler the symmetric and antisymmetric modes can convert to each other. For the simulation and calculation, the nonlinear coefficient we use is $d_{33} = 30$pm/V.

The period of the PPLN is decided by the phase mismatch, the pump power used here is 100mw at wavelength $\lambda_p = 780$nm, the wavelength of signal is $\lambda_s = 1550$nm, the idler wavelength is $\lambda_i = 1560$nm, then the phase mismatch is $\Delta k = k_s + k_i - k_p = 3.211 \times 10^5 m^{-1}$, hence the period of PPLN is $2\pi/\Delta k = 19.57\mu m$. The indies for the pump, signal and idler waves are 2.2580, 2.2111 and 2.2108 reslectively [247].

Figure 7-12 shows the forward and backward operation of optical isolator based on nonlinear optical mode conversion. The signal (1550nm) is input from the wide arm, and in the middle directional waveguide couplers, the symmetric propagation will be excited. The pump (780nm) is input from the narrow arm, hence the antisymmetric mode will be excited in the middle directional waveguide coupler. As we all know, the second order nonlinear coefficient can result in three wave mixing. Hence in the middle directional waveguide coupler, due to the three wave mixing, idler wave (1560nm) will

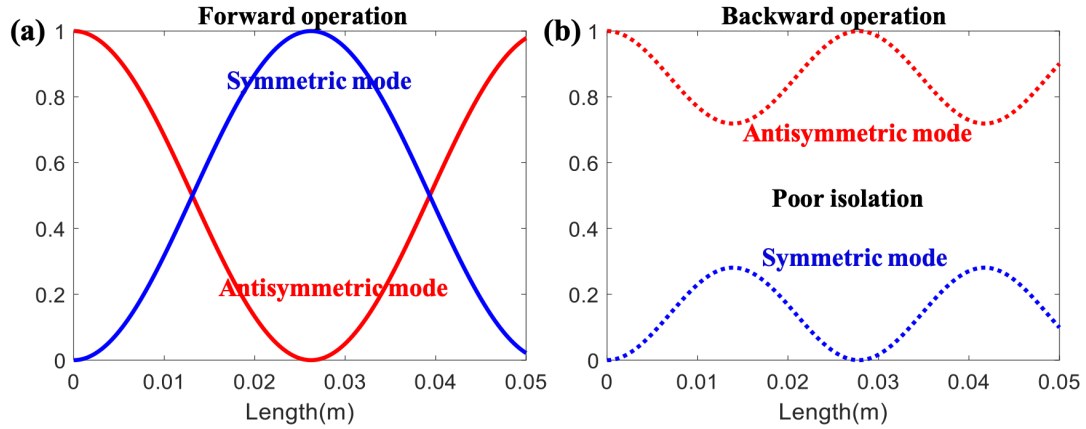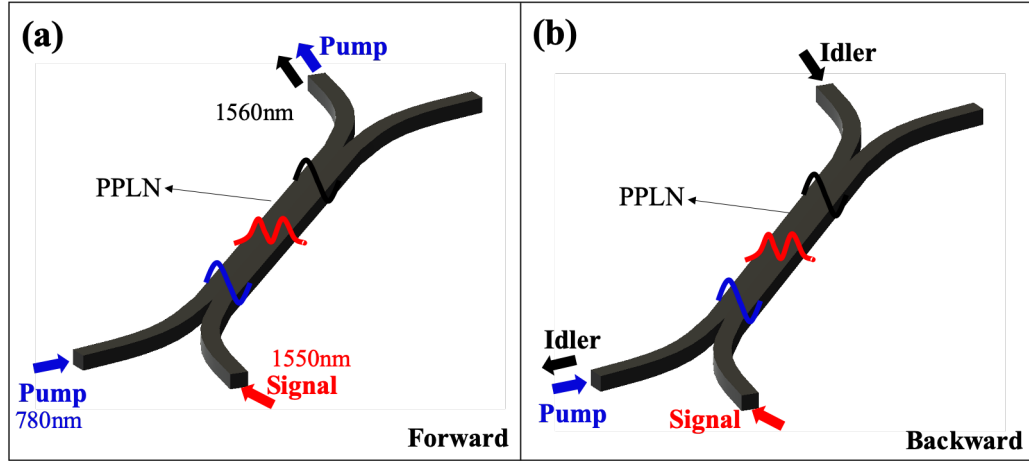**Figure 7-12.** The forward and backward operation of the PPLN optical isolator configuration.
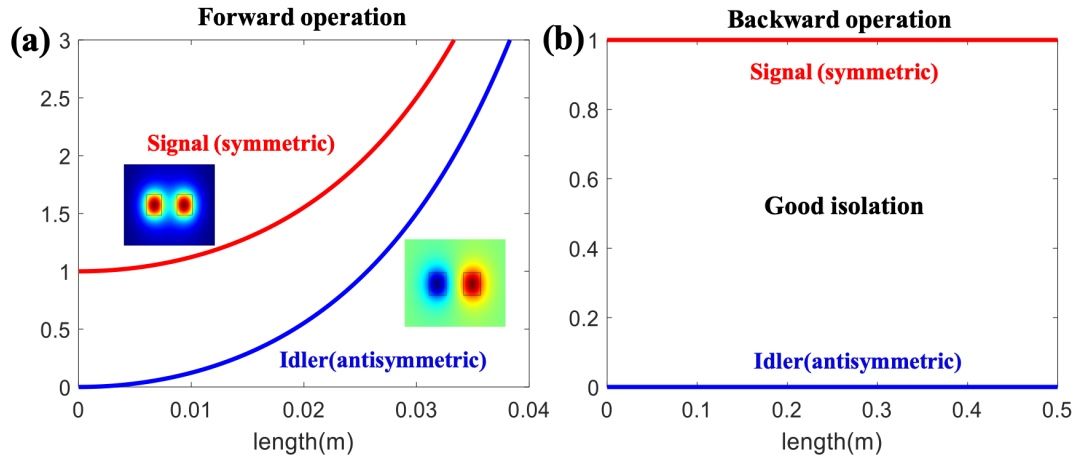
Figure 7-13. (a) and (b) are the forward and backward performance of the designed optical isolator when PPLN is used to match the phase mismatch.

be obtained, because the new generated idler wave is antisymmetric mode, hence, in the rare adiabatic waveguide coupler the idler wave couples to the narrow arm and output through the narrow arm. There are both pump and idler wave at the narrow arm output, so, in order to get the idler wave, a low-pass filter (LPF) is required at the narrow arm output, as shown in Fig. 7-12(a). For the backward operation, as show in the Fig. 7-12(b), when the idler wave is incident from the narrow arm of the rare arm, in the middle directional waveguide coupler, the antisymmetric mode will be excited, but due to the large phase mismatch ($\Delta k = k_s + k_i + k_p = 2k_{pump}$), the three

wave mixing process cannot happen there, therefor, the idler antisymmetric mode propagates from the rare to the front adiabatic waveguide coupler and output from the narrow arm of the front adiabatic waveguide coupler. Now, by using the second order nonlinear coefficient and three wave mixing, we have successfully achieved the asymmetric coupling and nonreciprocal transmission for the forward and backward operation in the waveguide coupler. Figure 7-13 shows the theoretical calculation, we assume that the pump is undepleted, in the middle directional waveguide coupler, the energy transfers from the pump to the idler wave, the three-wave mixing process is similar to the optical parameter amplifier. The power of the pump is 100nw, and our calculation shows that the required directional waveguide coupler length is about 2.8cm. Figure 7-13 shows the signal and idler wave for the backward operation, we can see that due to the large phase mismatch, the propagation of idler wave are totally isolated. Even though we are using the second order nonlinear coefficient, the performance of the optical isolator is linear, and its working bandwidth are very wide with low insertion loss. Moreover, our calculation shows full isolation can be achieved, only the LPF at the output can affect the performance of this optical isolator. The disadvantage here is the frequency shift- the idler wave and signal wave have different frequencies. The optical isolator involves frequency shit due to the difference frequency generate effect.

7.4 Conclusions

In this chapter, We have proposed and analyzed different schemes for non-magnetic optical isolators. We demonstrated the first one experimentally, it's achieved based on frequency conversion process (DFG) in single PPLN waveguide combining with spectral filters. It exhibits a wide bandwidth of more than 150 nm, limited only by the measurement setup, and an optical isolation ratio of up to 18 dB for the involved idler and signal waves. The difference of transmittance at the signal wavelength

between forward and backward propagation is 40 dB. Then to realize spectral filter-free and non-magnetic optical isolators, I have proposed and designed two optical isolators based on adiabatic waveguide coupler and waveguide conversion based on electro-optical effect and DFG. By comparison, I have demonstrated that the filter-free isolator based on electro-optical effect can work entirely in the telecom range with high power efficiency and wide band, but it's challenging to reach satisfying isolation in practice; the optical isolator based on nonlinear optical effect (DFG) on the other hand can offer full optical isolation with linearity and wide working band, but frequency of output wave is different from the original input due to the nonlinear optical three wave mixing process. Our new proposed optical isolators based on different schemes provide new choices for the development of integrated photonics.

Chapter 8

Conclusion

In this thesis I presented the results of my study of various aspects of light interaction with structured all-dielectric and metal-dielectric materials. Using theoretical analysis, numerical modeling, and, in some cases experimental measurements, I have identified and studied number of interesting properties of these materials which make them attractive for many applications. These include novel subwavelength imaging schemes, various sensors operating in visible and mid IR ranges, thermal emitters, photodetectors and non-reciprocal optical devices. At the same time, I have also pointed out to the constrains placed on the performance of structured materials by practical issues of losses, fabrication resolution and generally low efficiency of many optical processes. The results of the research have been published in 6 papers in high impact journals and presented at numerous conferences. These results present a small, but hopefully important step on the path to practical applications of metamaterials.

References

1. Wenshan, C. & Shalaev, V. Optical Metamaterials. Fundamentals and Applications. *Springer. pp. xi* **3,** 9 (2010).

2. Xi, S. *et al.* Experimental verification of reversed Cherenkov radiation in left-handed metamaterial. *Physical review letters* **103,** 194801 (2009).

3. Seddon, N. & Bearpark, T. Observation of the inverse Doppler effect. *Science* **302,** 1537–1540 (2003).

4. Maier, S. A. *Plasmonics: fundamentals and applications* (Springer Science & Business Media, 2007).

5. Schuster, A. *An introduction to the theory of optics* (E. Arnold, 1904).

6. Lamb, H. On Group-Velocity. *Proceedings of the London Mathematical Society* **2,** 473–479 (1904).

7. Mandel'shtam, L. Group velocity in a crystal lattice. *Zh. Eksp. Teor. Fiz* **15,** 18 (1945).

8. Sivukhin, D. The energy of electromagnetic waves in dispersive media. *Opt. Spektrosk* **3,** 308–312 (1957).

9. Veselago, V. G. The Electrodynamics of Substances with Simultaneously Negative Values of ϵ and μ. *Physics-Uspekhi* **10,** 509–514 (1968).

10. Pendry, J. B. Negative refraction makes a perfect lens. *Physical review letters* **85,** 3966 (2000).

11. Pendry, J. B., Schurig, D. & Smith, D. R. Controlling electromagnetic fields. *science* **312,** 1780–1782 (2006).

12. Smith, D. R., Pendry, J. B. & Wiltshire, M. C. Metamaterials and negative refractive index. *Science* **305,** 788–792 (2004).

13. Shalaev, V. M. *et al.* Negative index of refraction in optical metamaterials. *Optics letters* **30,** 3356–3358 (2005).

14. Fang, N., Lee, H., Sun, C. & Zhang, X. Sub–diffraction-limited optical imaging with a silver superlens. *Science* **308,** 534–537 (2005).

15. Alitalo, P. & Tretyakov, S. Electromagnetic cloaking with metamaterials. *Materials today* **12,** 22–29 (2009).

16. Schurig, D. *et al.* Metamaterial electromagnetic cloak at microwave frequencies. *Science* **314,** 977–980 (2006).

17. Yu, N. *et al.* Light propagation with phase discontinuities: generalized laws of reflection and refraction. *science* **334,** 333–337 (2011).

18. Cornbleet, S. Geometrical optics reviewed: a new light on an old subject. *Proceedings of the IEEE* **71,** 471–502 (1983).

19. Cathey, W. Three-dimensional wavefront reconstruction using a phase hologram. *JOSA* **55,** 457–457 (1965).

20. Ni, X., Emani, N. K., Kildishev, A. V., Boltasseva, A. & Shalaev, V. M. Broadband light bending with plasmonic nanoantennas. *Science* **335,** 427–427 (2012).

21. Yu, N. *et al.* A broadband, background-free quarter-wave plate based on plasmonic metasurfaces. *Nano letters* **12,** 6328–6333 (2012).

22. Yu, N. & Capasso, F. Flat optics with designer metasurfaces. *Nature materials* **13,** 139–150 (2014).

23. Aieta, F. *et al.* Aberration-free ultrathin flat lenses and axicons at telecom wavelengths based on plasmonic metasurfaces. *Nano letters* **12,** 4932–4936 (2012).

24. Pors, A., Nielsen, M. G., Eriksen, R. L. & Bozhevolnyi, S. I. Broadband focusing flat mirrors based on plasmonic gradient metasurfaces. *Nano letters* **13,** 829–834 (2013).

25. Aieta, F., Kats, M. A., Genevet, P. & Capasso, F. Multiwavelength achromatic metasurfaces by dispersive phase compensation. *Science* **347,** 1342–1345 (2015).

26. Khorasaninejad, M. *et al.* Metalenses at visible wavelengths: Diffraction-limited focusing and subwavelength resolution imaging. *Science* **352,** 1190–1194 (2016).

27. Smith, D. & Schurig, D. Electromagnetic wave propagation in media with indefinite permittivity and permeability tensors. *Physical Review Letters* **90,** 077405 (2003).

28. Lindell, I. V., Tretyakov, S., Nikoskinen, K. & Ilvonen, S. BW media—Media with negative parameters, capable of supporting backward waves. *Microwave and Optical Technology Letters* **31,** 129–133 (2001).

29. Belov, P. Backward waves and negative refraction in uniaxial dielectrics with negative dielectric permittivity along the anisotropy axis. *Microwave and Optical Technology Letters* **37,** 259–263 (2003).

30. Fisher, R. & Gould, R. Resonance cones in the field pattern of a short antenna in an anisotropic plasma. *Physical Review Letters* **22,** 1093 (1969).

31. Alekseyev, L. V., Podolskiy, V. A. & Narimanov, E. E. Homogeneous hyperbolic systems for terahertz and far-infrared frequencies. *Advances in OptoElectronics* **2012** (2012).

32. Noginov, M., Lapine, M., Podolskiy, V. & Kivshar, Y. Focus issue: hyperbolic metamaterials. *Optics express* **21,** 14895–14897 (2013).

33. Jacob, Z., Smolyaninov, I. I. & Narimanov, E. E. Broadband Purcell effect: Radiative decay engineering with metamaterials. *Applied Physics Letters* **100,** 181105 (2012).

34. Biehs, S.-A., Tschikin, M. & Ben-Abdallah, P. Hyperbolic metamaterials as an analog of a blackbody in the near field. *Physical review letters* **109,** 104301 (2012).

35. Li, J., Fok, L., Yin, X., Bartal, G. & Zhang, X. Experimental demonstration of an acoustic magnifying hyperlens. *Nature materials* **8,** 931–934 (2009).

36. Smolyaninov, I. I. & Narimanov, E. E. Metric signature transitions in optical meta-materials. *Physical Review Letters* **105,** 067402 (2010).

37. Smolyaninov, I. I., Hung, Y.-J. & Hwang, E. Experimental modeling of cosmological inflation with metamaterials. *Physics Letters A* **376,** 2575–2579 (2012).

38. Smolyaninov, I. I. & Kildishev, A. V. Light propagation through random hyperbolic media. *Optics letters* **38,** 971–973 (2013).

39. Liu, Z., Lee, H., Xiong, Y., Sun, C. & Zhang, X. Far-field optical hyperlens magnifying sub-diffraction-limited objects. *science* **315,** 1686–1686 (2007).

40. Rho, J. *et al.* Spherical hyperlens for two-dimensional sub-diffractional imaging at visible frequencies. *Nature communications* **1,** 1–5 (2010).

41. Ishii, S., Kildishev, A. V., Narimanov, E., Shalaev, V. M. & Drachev, V. P. Sub-wavelength interference pattern from volume plasmon polaritons in a hyperbolic medium. *Laser & Photonics Reviews* **7,** 265–271 (2013).

42. Smith, D. R., Schurig, D., Mock, J. J., Kolinko, P. & Rye, P. Partial focusing of radiation by a slab of indefinite media. *Applied physics letters* **84,** 2244–2246 (2004).

43. Noginov, M. *et al.* Controlling spontaneous emission with metamaterials. *Optics letters* **35,** 1863–1865 (2010).

44. Tumkur, T. *et al.* Control of spontaneous emission in a volume of functionalized hyperbolic metamaterial. *Applied Physics Letters* **99,** 151115 (2011).

45. Agranovich, V. & Kravtsov, V. Notes on crystal optics of superlattices. *Solid State Communications* **55,** 85–90 (1985).

46. Shen, L., Yang, T.-J. & Chau, Y.-F. Effect of internal period on the optical dispersion of indefinite-medium materials. *Physical Review B* **77,** 205124 (2008).

47. Orlov, A. A., Voroshilov, P. M., Belov, P. A. & Kivshar, Y. S. Engineered optical nonlocality in nanostructured metamaterials. *Physical Review B* **84,** 045424 (2011).

48. Simovski, C. R., Belov, P. A., Atrashchenko, A. V. & Kivshar, Y. S. Wire metamaterials: physics and applications. *Advanced Materials* **24,** 4229–4248 (2012).

49. Silveirinha, M. G. Nonlocal homogenization model for a periodic array of ϵ-negative rods. *Physical Review E* **73,** 046612 (2006).

50. Evans, P. *et al.* Growth and properties of gold and nickel nanorods in thin film alumina. *Nanotechnology* **17,** 5746 (2006).

51. Noginov, M. *et al.* Bulk photonic metamaterial with hyperbolic dispersion. *Applied Physics Letters* **94,** 151105 (2009).

52. Kabashin, A. *et al.* Plasmonic nanorod metamaterials for biosensing. *Nature materials* **8,** 867–871 (2009).

53. Wurtz, G. A. *et al.* Designed ultrafast optical nonlinearity in a plasmonic nanorod metamaterial enhanced by nonlocality. *Nature nanotechnology* **6,** 107 (2011).

54. Krishnamoorthy, H. N., Jacob, Z., Narimanov, E., Kretzschmar, I. & Menon, V. M. Topological transitions in metamaterials. *Science* **336,** 205–209 (2012).

55. Kidwai, O., Zhukovsky, S. V. & Sipe, J. Effective-medium approach to planar multilayer hyperbolic metamaterials: Strengths and limitations. *Physical Review A* **85,** 053842 (2012).

56. Wood, B., Pendry, J. & Tsai, D. Directed subwavelength imaging using a layered metal-dielectric system. *Physical Review B* **74,** 115116 (2006).

57. Elser, J., Podolskiy, V. A., Salakhutdinov, I. & Avrutsky, I. Nonlocal effects in effective-medium response of nanolayered metamaterials. *Applied physics letters* **90,** 191109 (2007).

58. Cortes, C., Newman, W., Molesky, S. & Jacob, Z. Quantum nanophotonics using hyperbolic metamaterials. *Journal of Optics* **14,** 063001 (2012).

59. Poddubny, A. N., Belov, P. A., Ginzburg, P., Zayats, A. V. & Kivshar, Y. S. Microscopic model of Purcell enhancement in hyperbolic metamaterials. *Physical Review B* **86,** 035148 (2012).

60. Lu, D., Kan, J. J., Fullerton, E. E. & Liu, Z. Enhancing spontaneous emission rates of molecules using nanopatterned multilayer hyperbolic metamaterials. *Nature nanotechnology* **9,** 48–53 (2014).

61. Shalaginov, M. Y. *et al.* Broadband enhancement of spontaneous emission from nitrogen-vacancy centers in nanodiamonds by hyperbolic metamaterials. *Applied Physics Letters* **102,** 173114 (2013).

62. Kim, J. *et al.* Improving the radiative decay rate for dye molecules with hyperbolic metamaterials. *Optics express* **20,** 8100–8116 (2012).

63. Sreekanth, K. V., Krishna, K. H., De Luca, A. & Strangi, G. Large spontaneous emission rate enhancement in grating coupled hyperbolic metamaterials. *Scientific reports* **4,** 06340 (2014).

64. Liu, B. & Shen, S. Broadband near-field radiative thermal emitter/absorber based on hyperbolic metamaterials: Direct numerical simulation by the Wiener chaos expansion method. *Physical Review B* **87,** 115403 (2013).

65. Miller, O. D., Johnson, S. G. & Rodriguez, A. W. Effectiveness of thin films in lieu of hyperbolic metamaterials in the near field. *Physical review letters* **112,** 157402 (2014).

66. Korzeb, K., Gajc, M. & Pawlak, D. A. Compendium of natural hyperbolic materials. *Optics express* **23,** 25406–25424 (2015).

67. Kronig, R. d. L. & Penney, W. *Quantum mechanics of electrons in crystal lattices* in *Proceedings of the Royal Society of London A: Mathematical, Physical and Engineering Sciences* **130** (1931), 499–513.

68. Cho, H.-S. & Prucnal, P. R. New formalism of the Kronig-Penney model with application to superlattices. *Physical Review B* **36,** 3237 (1987).

69. Colvard, C., Merlin, R., Klein, M. & Gossard, A. Observation of folded acoustic phonons in a semiconductor superlattice. *Physical Review Letters* **45,** 298 (1980).

70. Mishra, S. & Satpathy, S. One-dimensional photonic crystal: The Kronig-Penney model. *Physical Review B* **68,** 045121 (2003).

71. Johnson, P. B. & Christy, R.-W. Optical constants of the noble metals. *Physical review B* **6,** 4370 (1972).

72. Engheta, N. Pursuing near-zero response. *Science* **340,** 286–287 (2013).

73. Maas, R., Parsons, J., Engheta, N. & Polman, A. Experimental realization of an epsilon-near-zero metamaterial at visible wavelengths. *Nature Photonics* **7,** 907–912 (2013).

74. Gómez Garcıa, P. & Fernández-Álvarez, J.-P. Floquet-Bloch theory and its application to the dispersion curves of nonperiodic layered systems. *Mathematical Problems in Engineering* **2015** (2015).

75. Naik, G. V., Liu, J., Kildishev, A. V., Shalaev, V. M. & Boltasseva, A. Demonstration of Al: ZnO as a plasmonic component for near-infrared metamaterials. *Proceedings of the National Academy of Sciences* **109,** 8834–8838 (2012).

76. Eyges, L. & Wintersteiner, P. Modes of an array of dielectric waveguides. *JOSA* **71,** 1351–1360 (1981).

77. Douillard, L. *et al.* Short range plasmon resonators probed by photoemission electron microscopy. *Nano letters* **8,** 935–940 (2008).

78. Khurgin, J. B. How to deal with the loss in plasmonics and metamaterials. *Nature nanotechnology* **10,** 2–6 (2015).

79. Sarid, D. Long-range surface-plasma waves on very thin metal films. *Physical Review Letters* **47,** 1927 (1981).

80. Berini, P. Long-range surface plasmon polaritons. *Advances in Optics and Photonics* **1,** 484–588 (2009).

81. Barnes, W. Fluorescence near interfaces: the role of photonic mode density. *journal of modern optics* **45,** 661–699 (1998).

82. Okamoto, K. *et al.* Surface-plasmon-enhanced light emitters based on InGaN quantum wells. *Nature materials* **3,** 601–605 (2004).

83. Caldwell, J. D. *et al.* Sub-diffractional volume-confined polaritons in the natural hyperbolic material hexagonal boron nitride. *Nature communications* **5,** 5221 (2014).

84. Siegner, U., Fluck, R., Zhang, G. & Keller, U. Ultrafast high-intensity nonlinear absorption dynamics in low-temperature grown gallium arsenide. *Applied physics letters* **69,** 2566–2568 (1996).

85. Wang, W. *et al.* Far-field imaging device: planar hyperlens with magnification using multi-layer metamaterial. *Optics express* **16,** 21142–21148 (2008).

86. Smith, E., Liu, Z., Mei, Y. & Schmidt, O. System investigation of a rolled-up meta-material optical hyperlens structure. *Applied physics letters* **95,** 083104 (2009).

87. Byun, M. *et al.* Demonstration of nanoimprinted hyperlens array for high-throughput sub-diffraction imaging. *Scientific reports* **7,** 46314 (2017).

88. Avrutsky, I., Salakhutdinov, I., Elser, J. & Podolskiy, V. Highly confined optical modes in nanoscale metal-dielectric multilayers. *Physical Review B* **75,** 241402 (2007).

89. Zhang, Z. & Satpathy, S. Electromagnetic wave propagation in periodic structures: Bloch wave solution of Maxwell's equations. *Physical review letters* **65,** 2650 (1990).

90. Willets, K. A. & Van Duyne, R. P. Localized surface plasmon resonance spectroscopy and sensing. *Annu. Rev. Phys. Chem.* **58,** 267–297 (2007).

91. Zeng, S., Baillargeat, D., Ho, H.-P. & Yong, K.-T. Nanomaterials enhanced surface plasmon resonance for biological and chemical sensing applications. *Chemical Society Reviews* **43,** 3426–3452 (2014).

92. Atwater, H. A. & Polman, A. Plasmonics for improved photovoltaic devices. *Nature Materials* **9,** 205–213 (2010).

93. Kauranen, M. & Zayats, A. V. Nonlinear plasmonics. *Nature Photonics* **6,** 737–748 (2012).

94. Naik, G. V. *et al.* Titanium nitride as a plasmonic material for visible and near-infrared wavelengths. *Optical Materials Express* **2,** 478–489 (2012).

95. Kanehara, M., Koike, H., Yoshinaga, T. & Teranishi, T. Indium tin oxide nanoparticles with compositionally tunable surface plasmon resonance frequencies in the near-IR region. *Journal of the American Chemical Society* **131,** 17736–17737 (2009).

96. Franzen, S. Surface plasmon polaritons and screened plasma absorption in indium tin oxide compared to silver and gold. *The Journal of Physical Chemistry C* **112,** 6027–6032 (2008).

97. Buonsanti, R., Llordes, A., Aloni, S., Helms, B. A. & Milliron, D. J. Tunable infrared absorption and visible transparency of colloidal aluminum-doped zinc oxide nanocrystals. *Nano Letters* **11,** 4706–4710 (2011).

98. Caldwell, J. D. *et al.* Low-loss, infrared and terahertz nanophotonics using surface phonon polaritons. *Nanophotonics* **4,** 44–68 (2015).

99. Tassin, P., Koschny, T., Kafesaki, M. & Soukoulis, C. M. A comparison of graphene, superconductors and metals as conductors for metamaterials and plasmonics. *Nature Photonics* **6,** 259–264 (2012).

100. Jahani, S. & Jacob, Z. All-dielectric metamaterials. *Nature Nanotechnology* **11,** 23–36 (2016).

101. Khurgin, J. B. Replacing noble metals with alternative materials in plasmonics and metamaterials: how good an idea? *Phil. Trans. R. Soc. A* **375,** 20160068 (2017).

102. Hsieh, W. T. *et al.* Comparative Analysis of Metals and Alternative Infrared Plasmonic Materials. *ACS Photonics* **5,** 2541–2548. eprint: https://doi.org/10.1021/acsphotonics.7b01166 (2018).

103. Khurgin, J. B. Relative merits of phononics vs. plasmonics: the energy balance approach. *Nanophotonics* **7,** 305–316 (2018).

104. Miller, O. D. *et al.* Fundamental limits to optical response in absorptive systems. *Optics Express* **24,** 3329–3364 (2016).

105. Miller, O. D. *et al.* Fundamental limits to extinction by metallic nanoparticles. *Physical Review Letters* **112,** 123903 (2014).

106. Spitzer, W., Kleinman, D. & Walsh, D. Infrared properties of hexagonal silicon carbide. *Physical Review* **113,** 127 (1959).

107. Mutschke, H., Andersen, A., Clément, D., Henning, T. & Peiter, G. Infrared properties of SiC particles. *arXiv preprint astro-ph/9903031* (1999).

108. Jackson, J. D. *Classical electrodynamics* (Wiley, 1999).

109. Baranov, D. G. *et al.* All-dielectric nanophotonics: the quest for better materials and fabrication techniques. *Optica* **4,** 814–825 (2017).

110. Evlyukhin, A. B. *et al.* Demonstration of magnetic dipole resonances of dielectric nanospheres in the visible region. *Nano Letters* **12,** 3749–3755 (2012).

111. Kuznetsov, A. I., Miroshnichenko, A. E., Fu, Y. H., Zhang, J. & Luk'yanchuk, B. Magnetic light. *Scientific Reports* **2,** 492 (2012).

112. Lin, R.-B., Liu, S.-Y., Ye, J.-W., Li, X.-Y. & Zhang, J.-P. Photoluminescent metal–organic frameworks for gas sensing. *Advanced Science* **3** (2016).

113. Lin, J., Zhang, Y., Qian, J. & He, S. A nano-plasmonic chip for simultaneous sensing with dual-resonance surface-enhanced Raman scattering and localized surface plasmon resonance. *Laser & Photonics Reviews* **8,** 610–616 (2014).

114. Osawa, M. in *Near-field optics and surface plasmon polaritons* 163–187 (Springer, 2001).

115. Marinica, D., Kazansky, A., Nordlander, P., Aizpurua, J. & Borisov, A. Quantum plasmonics: nonlinear effects in the field enhancement of a plasmonic nanoparticle dimer. *Nano Letters* **12,** 1333–1339 (2012).

116. Chow, T. T. A review on photovoltaic/thermal hybrid solar technology. *Applied Energy* **87,** 365–379 (2010).

117. Kildishev, A. V., Boltasseva, A. & Shalaev, V. M. Planar photonics with metasurfaces. *Science* **339,** 1232009 (2013).

118. Zhao, Y., Belkin, M. A. & Alù, A. Twisted optical metamaterials for planarized ultrathin broadband circular polarizers. *Nature communications* **3,** 1–7 (2012).

119. Niv, A., Biener, G., Kleiner, V. & Hasman, E. Spiral phase elements obtained by use of discrete space-variant subwavelength gratings. *Optics communications* **251,** 306–314 (2005).

120. Levy, U., Kim, H.-C., Tsai, C.-H. & Fainman, Y. Near-infrared demonstration of computer-generated holograms implemented by using subwavelength gratings with space-variant orientation. *Optics letters* **30,** 2089–2091 (2005).

121. Boltasseva, A. & Atwater, H. A. Low-loss plasmonic metamaterials. *Science* **331,** 290–291 (2011).

122. Fan, P. *et al.* An invisible metal–semiconductor photodetector. *Nature Photonics* **6,** 380 (2012).

123. Businaro, L. *et al.* Mid-infrared nanoantenna arrays on silicon and CaF2 substrates for sensing applications. *Microelectronic engineering* **97,** 197–200 (2012).

124. Miyazaki, H. *et al.* Dual-band infrared metasurface thermal emitter for CO2 sensing. *Applied Physics Letters* **105,** 121107 (2014).

125. Makhsiyan, M., Bouchon, P., Jaeck, J., Pelouard, J.-L. & Haïdar, R. Shaping the spatial and spectral emissivity at the diffraction limit. *Applied Physics Letters* **107,** 251103 (2015).

126. Liu, X. *et al.* Taming the blackbody with infrared metamaterials as selective thermal emitters. *Physical review letters* **107,** 045901 (2011).

127. Sun, K. *et al.* Metasurface optical solar reflectors using AZO transparent conducting oxides for radiative cooling of spacecraft. *ACS Photonics* **5,** 495–501 (2018).

128. Rodrigo, D. *et al.* Resolving molecule-specific information in dynamic lipid membrane processes with multi-resonant infrared metasurfaces. *Nature communications* **9,** 1–9 (2018).

129. Valentine, J. *et al.* Three-dimensional optical metamaterial with a negative refractive index. *nature* **455,** 376–379 (2008).

130. Ni, X., Kildishev, A. & Shalaev, V. Metasurface holograms for visible light Nat. *Commun* **4,** 2807 (2013).

131. Chou, S. Y., Krauss, P. R. & Renstrom, P. J. Imprint lithography with 25-nanometer resolution. *Science* **272,** 85–87 (1996).

132. Lucas, B. D., Kim, J.-S., Chin, C. & Guo, L. J. Nanoimprint Lithography Based Approach for the Fabrication of Large-Area, Uniformly-Oriented Plasmonic Arrays. *Advanced Materials* **20,** 1129–1134 (2008).

133. Boltasseva, A. Plasmonic components fabrication via nanoimprint. *Journal of Optics A: Pure and Applied Optics* **11,** 114001 (2009).

134. Pedersen, R. H. *et al.* Nanoimprinted reflecting gratings for long-range surface plasmon polaritons. *Microelectronic engineering* **84,** 895–898 (2007).

135. Fernandez-Cuesta, I. *et al.* V-groove plasmonic waveguides fabricated by nanoimprint lithography. *Journal of Vacuum Science & Technology B: Microelectronics and Nanometer Structures Processing, Measurement, and Phenomena* **25,** 2649–2653 (2007).

136. Nielsen, R. B. *et al.* Channel plasmon polariton propagation in nanoimprinted V-groove waveguides. *Optics letters* **33,** 2800–2802 (2008).

137. Wu, W. *et al.* Midinfrared metamaterials fabricated by nanoimprint lithography. *Applied physics letters* **90,** 063107 (2007).

138. Wu, W. *et al.* Optical metamaterials at near and mid-IR range fabricated by nanoimprint lithography. *Applied Physics A* **87,** 143–150 (2007).

139. Yao, Y. *et al.* Nanoimprint-defined, large-area meta-surfaces for unidirectional optical transmission with superior extinction in the visible-to-infrared range. *Optics express* **24,** 15362–15372 (2016).

140. Bergmair, I. *et al.* Single and multilayer metamaterials fabricated by nanoimprint lithography. *Nanotechnology* **22,** 325301 (2011).

141. Cattoni, A. *et al.* $\lambda3/1000$ plasmonic nanocavities for biosensing fabricated by soft UV nanoimprint lithography. *Nano letters* **11,** 3557–3563 (2011).

142. Yao, J. *et al.* Functional nanostructured plasmonic materials. *Advanced Materials* **22,** 1102–1110 (2010).

143. Lee, S.-W. *et al.* Highly sensitive biosensing using arrays of plasmonic Au nanodisks realized by nanoimprint lithography. *ACS nano* **5,** 897–904 (2011).

144. Varghese, L. T. *et al.* Resistless nanoimprinting in metal for plasmonic nanostructures. *Small* **9,** 3778–3783 (2013).

145. Liang, C.-C. *et al.* Plasmonic metallic nanostructures by direct nanoimprinting of gold nanoparticles. *Optics express* **19,** 4768–4776 (2011).

146. Chen, W. *et al.* Large-area nanoimprinted colloidal Au nanocrystal-based nanoantennas for ultrathin polarizing plasmonic metasurfaces. *Nano letters* **15,** 5254–5260 (2015).

147. Chen, W. *et al.* Angle-Independent Optical Moisture Sensors Based on Hydrogel-Coated Plasmonic Lattice Arrays. *ACS Applied Nano Materials* **1,** 1430–1437 (2018).

148. Park, S. J. *et al.* Modulation of the effective density and refractive index of carbon nanotube forests via nanoimprint lithography. *Carbon* **129,** 8–14 (2018).

149. Taylor, J. H. & Yates, H. W. Atmospheric transmission in the infrared. *JOSA* **47,** 223–226 (1957).

150. Yates, H. & Taylor, J. *Infrared transmission of the atmosphere* tech. rep. (NAVAL RESEARCH LAB WASHINGTON DC, 1960).

151. Werle, P. *et al.* Near-and mid-infrared laser-optical sensors for gas analysis. *Optics and lasers in engineering* **37,** 101–114 (2002).

152. Richter, D. *et al.* Field measurements of volcanic gases using tunable diode laser based mid-infrared and Fourier transform infrared spectrometers. *Optics and Lasers in Engineering* **37,** 171–186 (2002).

153. Rayleigh, L. LIII. Remarks upon the law of complete radiation (1900).

154. Novotny, L. Effective wavelength scaling for optical antennas. *Physical Review Letters* **98,** 266802 (2007).

155. Dodge, M. J. Refractive properties of magnesium fluoride. *Applied Optics* **23,** 1980–1985 (1984).

156. Lucas, J., Smektala, F. & Adam, J. L. Fluorine in optics. *Journal of fluorine chemistry* **114,** 113–118 (2002).

157. Fiori, G. *et al.* Electronics based on two-dimensional materials. *Nature nanotechnology* **9,** 768 (2014).

158. Lopez-Sanchez, O., Lembke, D., Kayci, M., Radenovic, A. & Kis, A. Ultrasensitive photodetectors based on monolayer MoS 2. *Nature nanotechnology* **8,** 497–501 (2013).

159. Anasori, B., Lukatskaya, M. R. & Gogotsi, Y. 2D metal carbides and nitrides (MXenes) for energy storage. *Nature Reviews Materials* **2,** 1–17 (2017).

160. Anichini, C. *et al.* Chemical sensing with 2D materials. *Chemical Society Reviews* **47,** 4860–4908 (2018).

161. Xie, S. *et al.* Coherent, atomically thin transition-metal dichalcogenide superlattices with engineered strain. *Science* **359,** 1131–1136 (2018).

162. Novoselov, K. S. *et al.* A roadmap for graphene. *nature* **490,** 192–200 (2012).

163. Novoselov, K., Mishchenko, A., Carvalho, A. & Neto, A. C. 2D materials and van der Waals heterostructures. *Science* **353,** aac9439 (2016).

164. Blees, M. K. *et al.* Graphene kirigami. *Nature* **524,** 204–207 (2015).

165. Xu, W. & Gracias, D. H. Soft Three-Dimensional Robots with Hard Two-Dimensional Materials. *ACS nano* **13,** 4883–4892 (2019).

166. Xu, W., Kwok, K. S. & Gracias, D. H. Ultrathin shape change smart materials. *Accounts of chemical research* **51,** 436–444 (2018).

167. Xu, W. *et al.* Ultrathin thermoresponsive self-folding 3D graphene. *Science advances* **3,** e1701084 (2017).

168. Xu, W. *et al.* Self-folding hybrid graphene skin for 3D biosensing. *Nano letters* **19,** 1409–1417 (2018).

169. Shenoy, V. B. & Gracias, D. H. Self-folding thin-film materials: From nanopolyhedra to graphene origami. *Mrs Bulletin* **37,** 847–854 (2012).

170. Wang, H. *et al.* Self-rolling and light-trapping in flexible quantum well–embedded nanomembranes for wide-angle infrared photodetectors. *Science advances* **2,** e1600027 (2016).

171. Rogers, J., Huang, Y., Schmidt, O. G. & Gracias, D. H. Origami mems and nems. *Mrs Bulletin* **41,** 123–129 (2016).

172. Bernardi, M., Ferralis, N., Wan, J. H., Villalon, R. & Grossman, J. C. Solar energy generation in three dimensions. *Energy & Environmental Science* **5,** 6880–6884 (2012).

173. Lamoureux, A., Lee, K., Shlian, M., Forrest, S. R. & Shtein, M. Dynamic kirigami structures for integrated solar tracking. *Nature communications* **6,** 8092 (2015).

174. Song, Y. M. *et al.* Digital cameras with designs inspired by the arthropod eye. *Nature* **497,** 95–99 (2013).

175. Zhang, K. *et al.* Origami silicon optoelectronics for hemispherical electronic eye systems. *Nature communications* **8,** 1–8 (2017).

176. Xia, F., Wang, H., Xiao, D., Dubey, M. & Ramasubramaniam, A. Two-dimensional material nanophotonics. *Nature Photonics* **8,** 899 (2014).

177. Mak, K. F., McGill, K. L., Park, J. & McEuen, P. L. The valley Hall effect in MoS2 transistors. *Science* **344,** 1489–1492 (2014).

178. Koppens, F. *et al.* Photodetectors based on graphene, other two-dimensional materials and hybrid systems. *Nature nanotechnology* **9,** 780 (2014).

179. Mueller, T., Xia, F. & Avouris, P. Graphene photodetectors for high-speed optical communications. *Nature photonics* **4,** 297 (2010).

180. Gabor, N. M. *et al.* Hot carrier–assisted intrinsic photoresponse in graphene. *Science* **334,** 648–652 (2011).

181. Wang, L. *et al.* On-Chip Rolling Design for Controllable Strain Engineering and Enhanced Photon–Phonon Interaction in Graphene. *Small* **15,** 1805477 (2019).

182. Kang, P., Wang, M. C., Knapp, P. M. & Nam, S. Crumpled Graphene Photodetector with Enhanced, Strain-Tunable, and Wavelength-Selective Photoresponsivity. *Advanced Materials* **28,** 4639–4645 (2016).

183. Deng, T. *et al.* Three-dimensional graphene field-effect transistors as high-performance photodetectors. *Nano letters* **19,** 1494–1503 (2019).

184. Lee, W. *et al.* Two-dimensional materials in functional three-dimensional architectures with applications in photodetection and imaging. *Nature communications* **9,** 1–9 (2018).

185. Miskin, M. Z. *et al.* Graphene-based bimorphs for micron-sized, autonomous origami machines. *Proceedings of the National Academy of Sciences* **115,** 466–470 (2018).

186. Reynolds, M. F. *et al.* Capillary Origami with Atomically Thin Membranes. *Nano letters* **19,** 6221–6226 (2019).

187. Baytekin, B., Cezan, S. D., Baytekin, H. T. & Grzybowski, B. A. Artificial heliotropism and nyctinasty based on optomechanical feedback and no electronics. *Soft robotics* **5,** 93–98 (2018).

188. Li, C., Liu, Y., Huang, X. & Jiang, H. Direct sun-driven artificial heliotropism for solar energy harvesting based on a photo-thermomechanical liquid-crystal elastomer nanocomposite. *Advanced Functional Materials* **22,** 5166–5174 (2012).

189. Shang, L., Zhang, W., Xu, K. & Zhao, Y. Bio-inspired intelligent structural color materials. *Materials Horizons* **6,** 945–958 (2019).

190. Deng, T. *et al.* Self-folding graphene-polymer bilayers. *Applied Physics Letters* **106,** 203108 (2015).

191. Kang, K. *et al.* High-mobility three-atom-thick semiconducting films with wafer-scale homogeneity. *Nature* **520,** 656–660 (2015).

192. De Fazio, D. *et al.* High responsivity, large-area graphene/MoS2 flexible photodetectors. *ACS nano* **10,** 8252–8262 (2016).

193. Jamal, M., Zarafshar, A. M. & Gracias, D. H. Differentially photo-crosslinked polymers enable self-assembling microfluidics. *Nature communications* **2,** 1–6 (2011).

194. Yu, H., Balogun, O., Li, B., Murray, T. W. & Zhang, X. Building embedded microchannels using a single layered SU-8, and determining Young's modulus using a laser acoustic technique. *Journal of Micromechanics and Microengineering* **14,** 1576 (2004).

195. Freitag, M., Low, T., Xia, F. & Avouris, P. Photoconductivity of biased graphene. *Nature Photonics* **7,** 53 (2013).

196. Konstantatos, G., Levina, L., Fischer, A. & Sargent, E. H. Engineering the temporal response of photoconductive photodetectors via selective introduction of surface trap states. *Nano letters* **8,** 1446–1450 (2008).

197. Ruffieux, P. *et al.* Electronic structure of atomically precise graphene nanoribbons. *Acs Nano* **6,** 6930–6935 (2012).

198. Jung, G.-H., Yoo, S. & Park, Q.-H. Measuring the optical permittivity of two-dimensional materials without a priori knowledge of electronic transitions. *Nanophotonics* **8,** 263–270 (2019).

199. Mukherjee, B. *et al.* Complex electrical permittivity of the monolayer molybdenum disulfide (MoS 2) in near UV and visible. *Optical Materials Express* **5,** 447–455 (2015).

200. Lloyd, D. *et al.* Band gap engineering with ultralarge biaxial strains in suspended monolayer MoS2. *Nano letters* **16,** 5836–5841 (2016).

201. He, K., Poole, C., Mak, K. F. & Shan, J. Experimental demonstration of continuous electronic structure tuning via strain in atomically thin MoS2. *Nano letters* **13,** 2931–2936 (2013).

202. Lee, H. S. *et al.* MoS2 nanosheet phototransistors with thickness-modulated optical energy gap. *Nano letters* **12,** 3695–3700 (2012).

203. Miura, K. & Lang, R. The science of Miura-ori: A review. *Origami* **4,** 87–99 (2009).

204. Ribbens, W. B. An optical circulator. *Applied Optics* **4,** 1037–1038 (1965).

205. Miller, D. A. Rationale and challenges for optical interconnects to electronic chips. *Proceedings of the IEEE* **88,** 728–749 (2000).

206. Jalas, D. *et al.* What is—and what is not—an optical isolator. *Nature Photonics* **7,** 579–582 (2013).

207. Shi, Y., Yu, Z. & Fan, S. Limitations of nonlinear optical isolators due to dynamic reciprocity. *Nature photonics* **9,** 388 (2015).

208. Sounas, D. L. & Alù, A. Non-reciprocal photonics based on time modulation. *Nature Photonics* **11,** 774–783 (2017).

209. Okamura, Y., Inuzuka, H., Kikuchi, T. & Yamamoto, S. Nonreciprocal propagation in magnetooptic YIG rib waveguides. *Journal of lightwave technology* **4,** 711–714 (1986).

210. Aichele, T., Lorenz, A., Hergt, R. & Görnert, P. Garnet layers prepared by liquid phase epitaxy for microwave and magneto-optical applications–a review. *Crystal Research and Technology: Journal of Experimental and Industrial Crystallography* **38,** 575–587 (2003).

211. Dötsch, H. *et al.* Applications of magneto-optical waveguides in integrated optics. *JOSA B* **22,** 240–253 (2005).

212. Bi, L. *et al.* On-chip optical isolation in monolithically integrated non-reciprocal optical resonators. *Nature Photonics* **5,** 758 (2011).

213. Stadler, B. J. & Mizumoto, T. Integrated magneto-optical materials and isolators: a review. *IEEE Photonics Journal* **6,** 1–15 (2013).

214. Pintus, P. *et al.* Microring-based optical isolator and circulator with integrated electromagnet for silicon photonics. *Journal of Lightwave Technology* **35,** 1429–1437 (2017).

215. Gallo, K., Assanto, G., Parameswaran, K. R. & Fejer, M. M. All-optical diode in a periodically poled lithium niobate waveguide. *Applied Physics Letters* **79,** 314–316 (2001).

216. Fan, L. *et al.* An all-silicon passive optical diode. *Science* **335,** 447–450 (2012).

217. Hua, S. *et al.* Demonstration of a chip-based optical isolator with parametric amplification. *Nature communications* **7,** 1–6 (2016).

218. Aleahmad, P., Khajavikhan, M., Christodoulides, D. & LiKamWa, P. Integrated multiport circulators for unidirectional optical information transport. *Scientific reports* **7,** 1–6 (2017).

219. Nazari, F. *et al.* Optical isolation via PT-symmetric nonlinear Fano resonances. *Optics express* **22,** 9574–9584 (2014).

220. Yu, Z. & Fan, S. Complete optical isolation created by indirect interband photonic transitions. *Nature photonics* **3,** 91 (2009).

221. Lira, H., Yu, Z., Fan, S. & Lipson, M. Electrically driven nonreciprocity induced by interband photonic transition on a silicon chip. *Physical review letters* **109,** 033901 (2012).

222. Chamanara, N., Taravati, S., Deck-Léger, Z.-L. & Caloz, C. Optical isolation based on space-time engineered asymmetric photonic band gaps. *Physical Review B* **96,** 155409 (2017).

223. Wang, Q. *et al.* A bidirectional tunable optical diode based on periodically poled LiNbO 3. *Optics express* **18,** 7340–7346 (2010).

224. Kim, J., Kim, S. & Bahl, G. Complete linear optical isolation at the microscale with ultralow loss. *Scientific reports* **7,** 1–9 (2017).

225. Bhandare, S. *et al.* Novel nonmagnetic 30-dB traveling-wave single-sideband optical isolator integrated in III/V material. *IEEE Journal of selected topics in quantum electronics* **11,** 417–421 (2005).

226. Doerr, C. R., Dupuis, N. & Zhang, L. Optical isolator using two tandem phase modulators. *Optics letters* **36,** 4293–4295 (2011).

227. Sounas, D. L. & Alu, A. Angular-momentum-biased nanorings to realize magnetic-free integrated optical isolation. *ACS photonics* **1,** 198–204 (2014).

228. Estep, N. A., Sounas, D. L., Soric, J. & Alù, A. Magnetic-free non-reciprocity and isolation based on parametrically modulated coupled-resonator loops. *Nature Physics* **10,** 923–927 (2014).

229. Li, T., Abdelsalam, K., Fathpour, S. & Khurgin, J. B. *Wide bandwidth, nonmagnetic linear optical isolators based on frequency conversion* in *CLEO: QELS_Fundamental Science* (2019), FW3B–7.

230. Rangelov, A. & Longhi, S. Nonlinear adiabatic optical isolator. *Applied optics* **56,** 2991–2994 (2017).

231. Rao, A. *et al.* Actively-monitored periodic-poling in thin-film lithium niobate photonic waveguides with ultrahigh nonlinear conversion efficiency of 4600% W- 1 cm- 2. *Optics express* **27,** 25920–25930 (2019).

232. Chang, L. *et al.* Thin film wavelength converters for photonic integrated circuits. *Optica* **3,** 531–535 (2016).

233. Wang, C. *et al.* Ultrahigh-efficiency wavelength conversion in nanophotonic periodically poled lithium niobate waveguides. *Optica* **5,** 1438–1441 (2018).

234. Fathpour, S. Heterogeneous nonlinear integrated photonics. *IEEE Journal of Quantum Electronics* **54,** 1–16 (2018).

235. Rao, A. *et al.* High-performance and linear thin-film lithium niobate Mach–Zehnder modulators on silicon up to 50 GHz. *Optics letters* **41,** 5700–5703 (2016).

236. Weigel, P. O. *et al.* Bonded thin film lithium niobate modulator on a silicon photonics platform exceeding 100 GHz 3-dB electrical modulation bandwidth. *Optics express* **26,** 23728–23739 (2018).

237. Wang, C. *et al.* Integrated lithium niobate electro-optic modulators operating at CMOS-compatible voltages. *Nature* **562,** 101–104 (2018).

238. Honardoost, A. *et al.* Cascaded integration of optical waveguides with third-order nonlinearity with lithium niobate waveguides on silicon substrates. *IEEE Photonics Journal* **10,** 1–9 (2018).

239. Sjaardema, T., Rao, A. & Fathpour, S. *Third-and Fourth-Harmonic Generation in Cascaded Periodically-Poled Lithium Niobate Ultracompact Waveguides on Silicon* in *CLEO: Science and Innovations* (2019), STh1J–1.

240. Zhao, J., Ma, C., Rüsing, M. & Mookherjea, S. Entangled photon-pair generation in periodically-poled thin-film lithium niobate waveguides. *arXiv preprint arXiv:1910.03202* (2019).

241. Elkus, B. S. *et al.* Generation of broadband correlated photon-pairs in short thin-film lithium-niobate waveguides. *Optics Express* **27,** 38521–38531 (2019).

242. Cai, L. *et al.* Acousto-optical modulation of thin film lithium niobate waveguide devices. *Photonics Research* **7,** 1003–1013 (2019).

243. Cai, L., Mahmoud, A. & Piazza, G. Low-loss waveguides on Y-cut thin film lithium niobate: towards acousto-optic applications. *Optics express* **27,** 9794–9802 (2019).

244. Nagy, J. T. & Reano, R. M. *Periodic poling of ion-sliced x-cut magnesium oxide doped lithium niobate thin films* in *2018 Conference on Lasers and Electro-Optics (CLEO)* (2018), 1–2.

245. Zhao, J., Rüsing, M. & Mookherjea, S. Optical diagnostic methods for monitoring the poling of thin-film lithium niobate waveguides. *Optics express* **27,** 12025–12038 (2019).

246. Wong, K.-K. *Properties of lithium niobate* **28** (IET, 2002).

247. Zelmon, D. E., Small, D. L. & Jundt, D. Infrared corrected Sellmeier coefficients for congruently grown lithium niobate and 5 mol.% magnesium oxide–doped lithium niobate. *JOSA B* **14,** 3319–3322 (1997).

3400 N Charles Street
Baltimore, Maryland 21218 USA
tli44@jhu.edu

EDUCATION AND DEGREES

- Ph.D. in Electrical Engineering (09/2014-06/2020)
  Department of Electrical and Computer Engineering, Johns Hopkins University
- M.S. in Optics (09/2011-06/2014)
  Department of Physics, Nankai University, China
- B.S. in Physics (09/2007-06/2011)
  Department of Physics and Electronic Science, Shandong Normal University, China

RESEARCH FIELDS

- Plasmonics
- Nano-photonics
- Integrated Photonics
- Metamaterials and Metasurfaces

SKILLS

- Knowledge of Electromagnetic, Photonics, Plasmonics, Semiconductor, Laser and Waveguide
- Knowledge of Optics and Optical Engineering including physical and geometry optics, optical materials, optical metrology methods and optical instruments
- Proficient simulation with COMSOL, Lumerical FDTD for light-matter interaction
- Experience with Optical Design software (Zemax) and Computer-Aided Design software (Auto-CAD)
- Knowledge of programing and data analysis with Matlab, C, and MySQL on Linux and Windows
- Hand-on Experience in micro- and nanofabrication with coating, etching, deposition and photolithography

EXPERIENCE

Johns Hopkins University, Department of Electrical and Computer Engineering *(09/2014-06/2020)*
Research and Teaching Assistant

- Explored, revealed and analyzed the origin of the novel optical properties of sub-wavelength multilayer optical metamaterials for high-resolution imaging, light radiation modulation.
- Analyzed and compared different field enhancement mechanisms in Nanophotonics through light-mater energy balance theory and FDTD simulation.
- Invented a new optical isolator for integrated photonics circuit based on waveguide coupler.
- Designed and fabricated 3D nano optical antenna metamaterials and metasurfaces for electromagnetic wave radiation modulation via Comsol, FDTD simulation and Lab fabrication.
- Participated in the development of 3D optical sensor based on graphene and self-assembly.

Nankai University, Department of Physics *(09/2011-06/2014)*
Research and Teaching Assistant

- Studied magneto-optical effect induced optical nonreciprocal transmission in waveguide.

MAJOR HONOR

- National scholarship awarded by Ministry of Education of the People's Republic of China

PRESENTATIONS

- **Tengfei Li**, and J. B. Khurgin. "What are the merits of hyperbolic metamaterials?" In CLEO: QEL-Fundamental Science,(2016).
- **Tengfei Li**, Vivek Nagal, David Gracias, and Jacob Khurgin. "Imaging with multilayer hyperbolic metamaterials-what are the limits?." In CLEO: QELS-Fundamental Science, pp. FTh4H-6, (2017).
- **Tengfei Li**, Vivek Nagal, David Gracias, and Jacob Khurgin. "Sub-wavelength field enhancement in mid-IR: Photonics vs Plasmonics vs Phononics," In CLEO: QELS-Fundamental Science,(2018).
- **Tengfei Li**, K Abdelsalam, S Fathpour, JB Khurgin. "Wide bandwidth, nonmagnetic linear optical isolators based on frequency conversion" In CLEO: QELS-Fundamental Science,(2019).
- Kamal Abdelsalam, **Tengfei Li**, Jacob Khurgin and Sasan Fathpour. " Wideband Nonmagnetic Linear Optical Isolator in Thin-Film Lithium Niobate " In CLEO: QELS-Fundamental Science,(2020).

PUBLICATIONS

- **Tengfei Li**, and Jacob B. Khurgin. "Hyperbolic metamaterials: beyond the effective medium theory." *Optica* 3,12 1388-1396 (2016)
- **Tengfei Li**, Vivek Nagal, David H. Gracias, and Jacob B. Khurgin. "Limits of imaging with multilayer hyperbolic metamaterials." *Optics Express* 25,12 13588-13601 (2017)
- **Tengfei Li**, Vivek Nagal, David H. Gracias, and Jacob B. Khurgin. "Sub-wavelength field enhancement in mid-IR: Photonics vs Plamsonics vs Photoinics. " *Optics Letter* 43, 18 4465-4468 (2018)
- Kamal Abdelsalam, **Tengfei Li**, Jacob B Khurgin, and Sasan Fathpour. "Linear isolators using wavelength conversion." *Optica*, 7(3):209–213, 2020
- Weinan Xu, **Tengfei Li**, Zhao Qin, Qi Huang, Hui Gao, Kibum Kang, Jiwoong Park, Markus J Buehler, Jacob B Khurgin, and David H Gracias. "Reversible mos2 origami with spatially resolved and reconfigurable photosensitivity." *Nano letters*, 19(11):7941–7949, (2019)
- Vivek Nagal, **Tengfei Li**, Jacob B. Khurgin, and David H. Gracias. "Nanomanufacturing of 3D polarization selective mid-IR metasurfaces." submitted to *ACS Applied Nano Materials* (2020)